Locating Ice Sheet Grounding Lines Using Satellite Radar Interferometry and Altimetry

Anna Elizabeth Hogg

Submitted in accordance with the requirements for the degree of
Doctor of Philosophy

The University of Leeds
School of Earth and Environment

Centre For Polar Observation and Modelling (CPOM)

August, 2015

Acknowledgements

This work was funded by a UK Natural Environment Research Council's (NERC) National Centre for Earth Observation (NCEO) PhD studentship, hosted jointly by the Centre for Polar Observation and Modelling (CPOM) at the University of Leeds and at the Directorate of Earth Observation Programmes, ESA-ESRIN.

Firstly, I thank my supervisor Andy Shepherd for his support, advice and encouragement over the last few years. The work contained in this thesis has been greatly improved by his contribution and I look forward to continuing to work together in the future. I am also extremely grateful to have received support from Martyn Chipperfield, Marcus Engdahl and Mark Doherty during the course my PhD.

Thanks also go to the many colleagues and friends who have kept me entertained, and excited about science throughout my PhD. In particular Kate, Debbie, Mal, Steve, David, Hannah and Aud have endured more than most. Finally thanks to my family and to Ali for always supporting me.

Abstract

In this thesis, I use synthetic aperture radar (SAR) and radar altimeter data to make new observations of Antarctic and Greenland ice sheet grounding lines.

I use ERS SAR data acquired between 1992 and 2011 to map the Petermann Glacier grounding line on 17 occasions using quadruple difference interferometric SAR (QDInSAR). Over the 19-year period, the grounding line position varied by 0.5 km, on average, with no significant trend over time. Although tidal forcing explains a fraction (34 %) of the movement, localised variations in the glacier thickness could explain it all were they to alter the glaciers hydrostatic balance as they advect downstream – a hitherto unconsidered possibility that would reduce the accuracy with which changes in grounding line position can be detected.

Next, I developed a new technique for detecting grounding lines using differential range direction offset tracking (DRDOT) in incoherent SAR data. I then applied this technique to a sequence of 11 TerraSAR-X images acquired in 2009 over Petermann Glacier. The DRDOT technique is able to reproduce the shape and location of the grounding line with an estimated lateral precision of 0.8 km and, although this is 30 times poorer than QDInSAR, provides a complementary method given the paucity of coherent SAR data.

Finally, I developed another new method for detecting the grounding line as the break in ice sheet surface slope computed from CryoSat-2 elevation measurements. I then applied this technique to map grounding lines in the sectors of Antarctica buttressed by the Filchner-Ronne, Ekström, Larsen-C, and Amundsen Sea ice shelves. The technique is able to map the grounding line to within 4.5 km, on average, and, although this is far poorer than either QDInSAR or DRDOT, it is computationally efficient and can succeed where SAR-based methods fail, offering an additional complementary approach.

Contents

Acronyms

Acronym	Definition
AODTM-5	Arctic Ocean Tidal Forward Model
ASTER	Advanced Spaceborne Thermal Emission and Reflection Radiometer
ATM	Airborne Topographic Mapper
CPOM	Centre for Earth Observation and Modelling
DEOS	Department of Earth Observation and Space Systems
DEM	Digital Elevation Model
DMT	Differential Modelled Tide
DRDOT	Differential Range Direction Offset Tracking
ERS	European Remote Sensing satellite
ESA	European Space Agency
GLAS	Geoscience Laser Altimeter System
GPS	Global Positioning System
GL	Grounding Line
HH	Horizontal Horizontal polarisation
HL	Hinge Line
ICESat	Ice, Cloud, and land Elevation Satellite
Ib	Break in surface Slope
IOM	Input Output Method
InSAR	Interferometric Synthetic Aperture Radar
IW	Interferometric Wide swath mode
L2i	Intermediate Level 2
LGM	Last Glacial Maximum
LRM	Low Rate Mode
MCoRDS	Multichannel Coherent Radar Depth Sounder
MLCC	Multi-Look Cross Correlation
NCEO	National Center for Earth Observation
NERC	Natural Environment Research Council
POCA	Point Of Closest Approach
QDInSAR	Quadruple Difference Synthetic Aperture Radar
SAR	Synthetic Aperture Radar
SARIn	Synthetic Aperture Radar Interferometry
SIRAL	SAR Interferometric Radar Altimeter
SLC	Single Look Complex
SSC	Single look Slant range Complex
TOPS	Terrain Observation with Progressive Scans mode

Chapter 1

Introduction and Background

1.1 Importance of Grounding Lines

Global mean sea level has risen at a rate of 1.7 mm per year during the 20th century; however, within the last 20 years this rate has increased to 3.2 mm per year (Church et al., 2013). The primary contributing factors include thermal expansion of the oceans, mass loss from ice situated on land (glaciers, ice caps, and ice sheets), and reduction in land water storage. Small differences between observed sea level rise and the sum of all contributing factors can be attributed to either omission of individual components, or measurement uncertainties. Ice losses from Greenland and Antarctica have increased rapidly over the recent decades – by 278 % and 148 % respectively since 1992 - and the most pronounced changes have occurred in places where the ice sheets are grounded well below sea level (Shepherd et al., 2012). Such marine-based and marine-terminating ice sheet sectors are particularly vulnerable to environmental change, because they are in contact with atmospheric and oceanic masses that are relatively warm, where modest changes in temperature can melt and destabilise the ice. In the most rapidly changing regions, such as the Amundsen Sea sector of West Antarctica and Jakobshavn Isbrae in Western Greenland, warm ocean currents have triggered glacier retreat (Park et al., 2013), leading to increased rates of ice flow (Joughin et al., 2014a) and ice thinning (McMillan et al., 2014) far inland. Elsewhere, at the Antarctic Peninsula, for example, changes in air temperature are believed to be a driver (Scambos et al., 2000) of ice shelf collapse (Rott et al., 1996) which, in turn, has also triggered drawdown of inland ice (Rignot et al., 2004). Ice sheet grounding lines are therefore a sensitive indicator of dynamic instability, and modelling the rate and spatial pattern of future change remains one of the most significant challenges limiting the accuracy of sea level rise projections (Church et al., 2013).

The junction between the floating ice shelf and the grounded ice sheet is of critical importance because it delineates the lateral extent of the ice sheet margin and determines the optimum location of flux gates used for calculating ice discharge and hence ice mass balance. In reality the grounding line is a transitory feature with a location that can fluctuate on short, sub-daily timescales due to the effects of ocean tides and localised ice thickness change (Thomas, 1984), or longer annual to decadal timescales when sustained ice thickness change caused by dynamic instability is present (Rignot et al., 1998b; Park et al., 2013). The grounding line is defined as the boundary between floating ice in hydrostatic equilibrium with the ocean, and grounded glacial ice (Cogley et al., 2011). It lies at the base of the ice sheet (Figure 1-1) and the hinge line is the manifestation of this flexure feature at the ice surface. Although there may be a small lateral variation in the locations of the hinge line and grounding line, their migration rates are similar, and so tracking either is an accurate measure of grounding line motion or stasis (Rignot et al., 1996). The grounding line lies within a region called the grounding zone which encompasses the full range of tidal motion, and can be up to a few kilometres wide in the in the flow-line direction, depending on factors such as bed topography and ocean tide heights. Ice within the grounding zone is supported by hydrostatic pressure from the sea below and internal stresses present within the glacial ice (Vaughan, 1995).

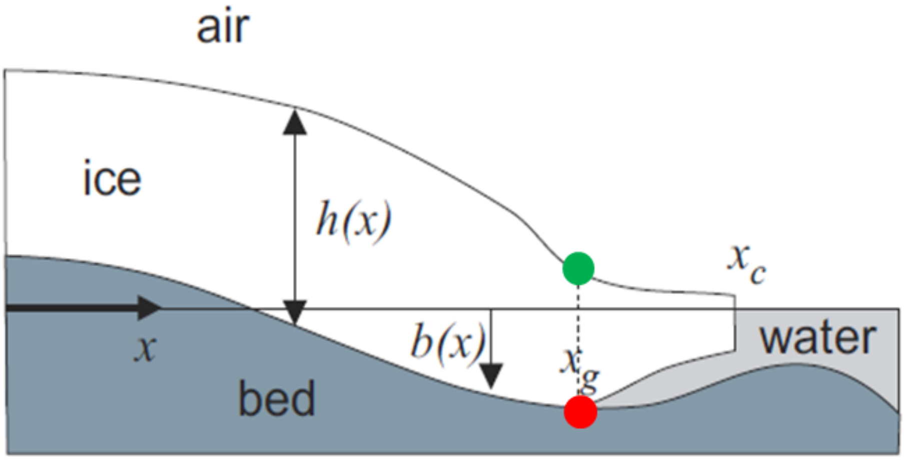

Figure 1-1. *Cross-section of an ice sheet grounding zone (reproduced from Schoof, 2007), showing the relative position of the grounding line (red dot) and the hinge line (green dot), where h(x) is ice thickness, b(x) is depth of ice below sea level,* x_g *is the grounding line and* x_c *is the calving front.*

Ice flow transitions at the grounding line from shear-dominated, basal-drag flow in the grounded ice sheet, to drag-free, side-shear-controlled, gravity spreading of flow in the floating ice shelf (Cuffey and Patterson, 2010). Combined, the lateral shearing and longitudinal stretching forces control the rate of ice outflow across the grounding line (Schoof, 2007). Grounding line retreat leads to a reduction in the resistive force which restrains grounded ice and controls the rate of ice discharge (Rignot et al., 2004). Ice sheet models and observations have shown that reduction or removal of this buttressing force can lead to rapid inland propagation of ice drawdown of marine based ice sheet sectors (Rignot et al., 2004; Joughin et al., 2010). This illustrates how relatively modest changes at the termini of outlet glaciers can have a marked impact on the wider ice sheet mass imbalance. In addition to influencing ice speed, grounding line retreat is also an indicator of decreasing ice thickness. When glacial thinning occurs faster than the rate of ablation, without downstream thickening or advance of the terminus, dynamic thinning can be said to occur. Measuring change in grounding line positions allows us to better understand the present day ice sheet contribution to sea level rise, and when ice sheet models accurately replicate the observed past change it provides improved confidence in their ability to predict the rate and magnitude of future dynamical imbalance (Favier et al., 2014).

Ice displacement across the grounding zone can be simulated by an elastic beam model which is dependent on a number of parameters including Poisson's Ratio, tide amplitude and ice shelf thickness and the Young's (elastic) modulus which determines the ice rigidity (Holdsworth, 1969). The model has been used to guide manual delineation of the grounding line and was successfully applied to displacement profiles measured in the field (Vaughan 1995) and in satellite datasets (Rignot, 1996; Rabus and Lang, 2002); however, routine application of the model for picking the grounding line has been limited. Parameters such as ice thickness at the grounding line and Young's modulus are spatially and temporally variable however these differences are not well characterised. It is challenging to accurately measure ice thickness at the grounding line from satellite altimetry datasets because the ice shelf is not yet in hydrostatic equilibrium with the ocean, and airborne radar measurements of the ice bedrock interface are sparse due to logistical constraints. The Young's modulus is also largely uncharacterised at the ice sheet margins; however, lab and field measurements suggest a large range of values between 1.1 and 10.0 GPa (Vaughan 1995). Detailed analysis of temporal variations in tidal flexure have shown that at a single location the value of Young’s modulus needs to vary with tide to match the observations, violating the elastic theory (Schmeltz et al, 2002). While some of the model misfit may be attributed to real change in the ice thickness and rigidity parameters, other studies have indicated that the elastic beam model is an oversimplification of ice flexure across the grounding zone (Tasi and Gudmundsson, 2015) and therefore may not be well suited to guiding manual delineation of the grounding line. Theoretical and numerical models provide important insights into dynamic processes of the grounding zone and in the future observational data will continue to provide essential information for establishing relations between surface elevation and ice thickness in grounding zones and grounding line migration.

1.2 Grounding Line Migration

In order to assess whether present day change in grounding line position is occurring at a faster rate now than it has done in the past, we must have an understanding of the historical retreat rates which occurred in the known past climate setting. Historical grounding line positions can be estimated by dating shells and diatoms in marine sediment cores and incorporated in raised beaches, radiocarbon dates of algae from ice dammed lakes and using paleoclimate model simulations (Conway et al., 1999; Pollard and DeConto, 2009). Grounding lines on the West Antarctic ice sheet are thought to have retreated nearly 1300 km since the Last Glacial Maximum (LGM) 20,000 years ago (Conway et al., 1999), and arrived at their approximate present day location nearly 3000 years ago (Pollard and DeConto, 2009). However, although the overall distance is large, the rate of retreat is slower than is observed today. Grounding line retreat in McMurdo Sound on the Ross Ice Shelf is estimated to have remained relatively constant over the last 7500 years with a retreat rate of approximately 0.12 km per year (Conway et al., 1999). Retreat rates measured on Ice Stream C on the Ross ice shelf between 1974 and 1984 are estimated to be much slower at 0.03 km per year; however, on neighbouring ice Stream B the retreat over the same time period was larger, at 0.45 km per year (Conway et al., 1999). These rates are comparable to Eurasian ice sheet retreat after the LGM which are estimated to be up to 0.15 km per year on ice streams, and 0.009 km per year on the inter-stream margins (Clark et al, 2012). Although these grounding line retreat rates are lower than the present day observations, some ice sheet model simulations have shown that during the disintegration of the West

Antarctic ice Sheet during the Holocene, even if the environmental forcing stabilises, once initiated the grounding line retreat continues for thousands of years (Huybrechts, 2002). This suggests that the inherently unstable bedrock setting of the West Antarctic ice sheet has had a role to play in both its historical and future stability (Thomas, 1979).

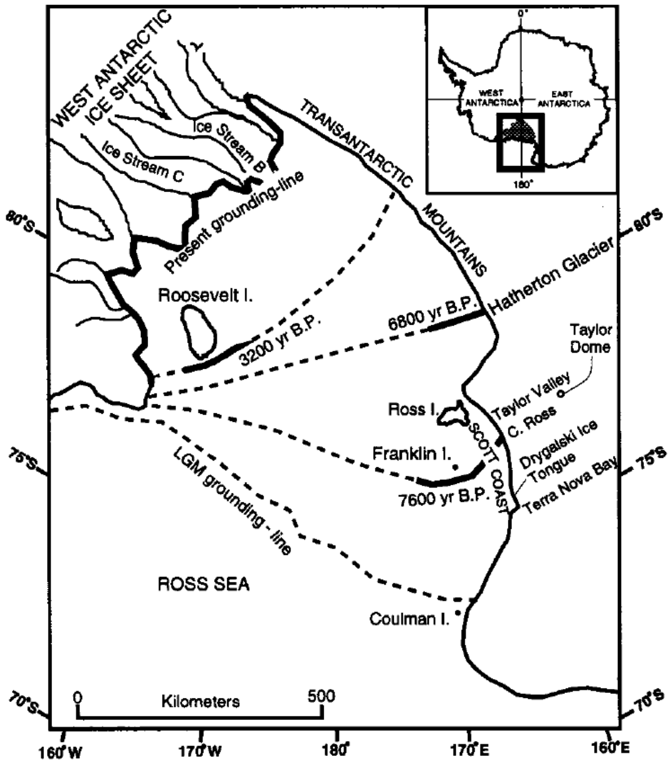

Figure 1-2. *Estimate of dated grounding line retreat on the Ross ice shelf during the Holocene (reproduced from Conway et al., 1999).*

The only present day observations of grounding line retreat have been made in the Amundsen Sea Sector of West Antarctica using satellite radar interferometry (Figure 1-3) (Park et al., 2013; Rignot et al., 2014). Over the last 25 years satellite observations have measured large spatial variability in the magnitude and onset of mass imbalance in neighbouring ice streams (McMillan et al., 2014) which supports model projections showing that future change will not be spatially and temporally homogeneous (Joughin et al., 2010, Joughin et al., 2014). The present day grounding line retreat rates recorded in this rapidly changing sector of Antarctica are 1.8 km per year at the centre of Smith/Kohler Glacier, 1.4 km per year on the main trunk of Pine Island Glacier with a lower rate of retreat on the ice stream margins, 0.8 km per year on Haynes Glacier, and 1 km per year on Cosgrove ice shelf (Rignot et al., 2014). The mean rate of retreat (1.25 km, Rignot et al., 2014) recorded on the main fast flowing ice trunks in the Amundsen Sea Sector is 12 times greater than the historical long term retreat (0.12 km per year, Conway et al., 1999) suggesting that the present day instability is occurring more rapidly than in the past.

Ice sheet mass balance has been measured using three Earth observation techniques including the Input Output Method (IOM) (Rignot et al., 2008), detection of gravitational mass anomalies (Horwath and Dietrich, 2009) and change in surface elevation (Shepherd and Wingham, 2007). Accurate knowledge of the grounding line position is an important parameter for all three techniques as the mass budget method requires ice velocity measurements inland of the grounding line (Rignot and Thomas, 2002), and gravimetry studies use weighted kernels to minimise signal leakage from change in ocean mass (Horwath and Dietrich, 2009). A strong positive correlation between decreasing ice thickness and grounding line retreat has also been observed (Park et al., 2013) which demonstrates that long term change in grounding line position acts as a sensitive indicator of dynamic imbalance.

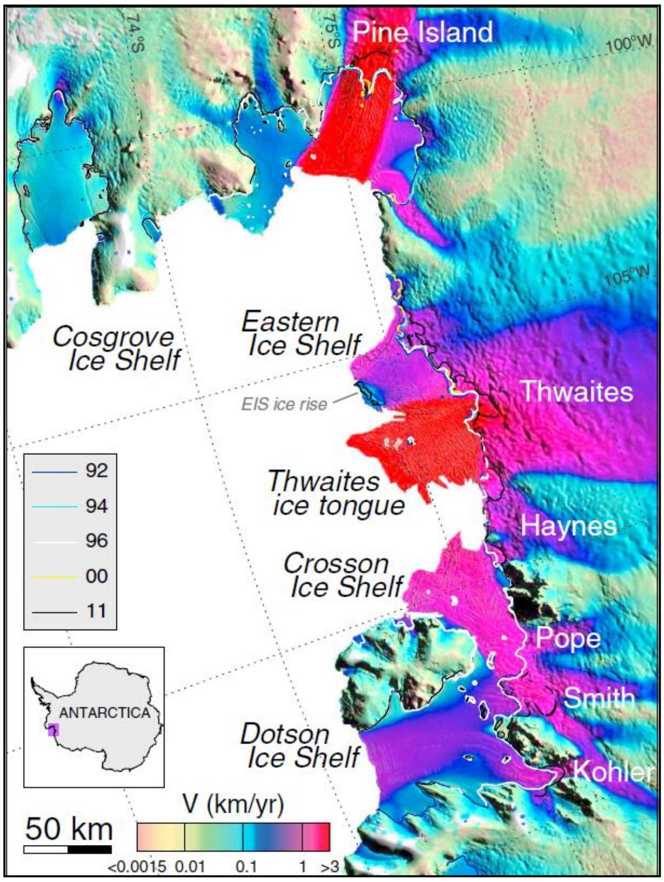

Figure 1-3. *Grounding line retreat measured using QDInSAR in the Amundsen Sea Sector, West Antarctica (reproduced from Rignot et al., 2014)*

Over the last 25 years, satellite observations have allowed us to accurately measure ice sheet mass balance and therefore quantify the present day ice sheet contribution to sea level rise (Shepherd et al., 2012). However, projections of future global sea level rise are more uncertain and estimates range from 20 cm to 2 m by 2100 (Willis and Church, 2012). When ice sheet models replicate past change, it provides greater confidence in their ability to accurately predict the future sea level contribution. Regional ice sheet models can now more accurately reproduce the spatial pattern of observed grounding line retreat in the Amundsen Sea Sector (Favier et al., 2014) (Figure 1-4). Under the same warming scenario, three different ice sheet models all predict a decrease in the grounded ice sheet area and an increasing contribution to sea level rise; however, there are still large unknowns, For example the rate and spatial pattern of these changes is not the same in all models (Figure 1-4). It is not possible to validate modelled grounding line migration outside of West Antarctica because the rate of retreat has not been observed around the majority of the grounded ice boundary. Grounding line retreat in the Amundsen Sea Sector has occurred in parallel with ocean warming caused by the influx of circumpolar deep water onto the continental shelf (Dutrieux et al., 2014). Knowledge of the spatial and temporal pattern of ocean temperature change with depth is limited by the availability of in situ measurements (Holland et al., 2008), therefore observations of grounding line retreat around the Antarctic ice sheet may indicate the presence of ocean forcing processes in other regions. In Antarctica the processed based link between ocean warming and dynamical imbalance is relatively well established; however, fully coupled ice-ocean-atmosphere model studies have yet to be performed (Joughin et al., 2012). New techniques must be developed to fully exploit the Earth observation data archive in order to increase the spatial and temporal density of contemporary grounding line measurements and to validate model projections of future change.

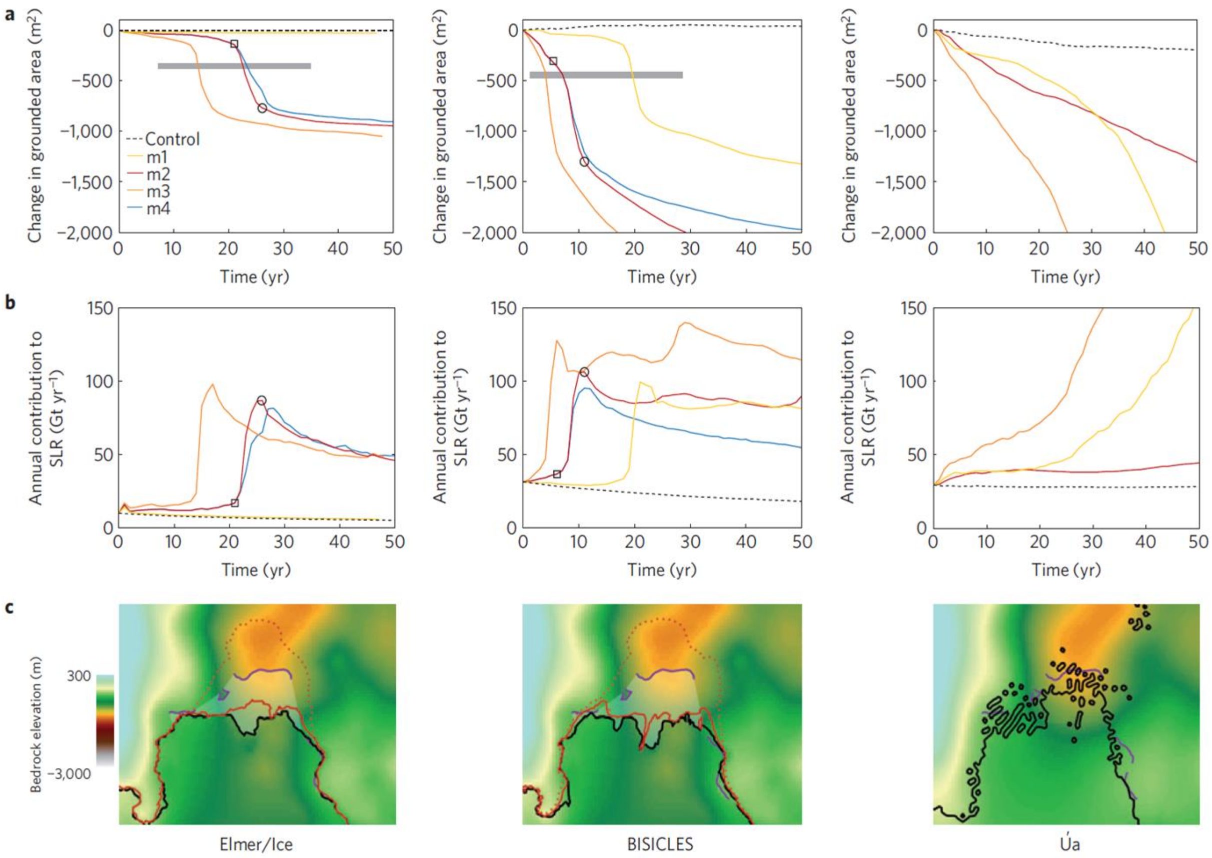

Figure 1-4. *a) Change in grounded area, b) contribution to sea level rise and c) spatial pattern of grounding line retreat in response to the same climate forcing, simulated by three of the most sophisticated, independent ice sheet models (reproduced from Favier et al., 2014).*

1.3 Review of Existing Methods for Detecting Grounding Lines

The grounding line can be detected using field techniques; however, sparse coverage, logistical difficulties and the high cost of repeatedly collecting measurements limit the practicality of in situ data collection on a large scale. Earth observation data and processing techniques provide a solution to these problems and enable data to be repeatedly acquired over the full ice sheet area. Here I present a brief summary of the in situ and Earth observation techniques that have previously been used to map the boundary between the grounded ice sheet and the floating ice shelf, and examples of the locations where these have been applied. Although these techniques provide valuable measurements, limitations in the availability of suitable Earth observation datasets and the absence of geographical features have limited the temporal resolution and spatial accuracy of grounding line datasets that have been produced to date.

1.3.1. Detecting Grounding Lines Using In Situ Methods

As the ice sheet grounding line is located at the base of the ice sheet it would be theoretically possible to send an automatic submersible vehicle under the ice shelf to directly measure this location. However, in practice all existing in situ and remote observation techniques use ice surface features, such as the inland limit of tidal flexure (the hinge line) or the break in surface slope, as a proxy for grounding line position. Three in situ methods have been used to measure ice sheet grounding line positions. The vertical displacement caused by ocean tides was measured across the grounding zone of the Rutford ice stream, Bach ice shelf and Jackobshavn Isbrae using kinematic GPS (Vaughan, 1995). Tilt-meters have also been used to measure the time varying component of the surface slope, which in the vicinity of the grounding zone is caused by ocean tides, on the Doake Ice Rumples (Smith, 1991), and Ekström ice shelf (Kobarg 1988). Finally, the historical ice sheet grounding line position has been estimated using marine bathymetry combined with radiocarbon chronologies of sea floor sediments in front of Crane Glacier on the Antarctic Peninsula (Rebesco et al., 2014).

Ground based observations of the grounding line position are extremely limited in both space and time due to the high cost and logistical difficulty of acquiring data over large areas. For all examples, a measurement has only been made at one epoch, and the spatial variability within the localised region is not well constrained. This presents a problem when there is a disagreement between two independent measurements. For example in the case of Crane Glacier there is a discrepancy between the in situ grounded extent and the grounding line positon measured using quadruple difference interferometry at an earlier date (Rack and Rott, 2004). The authors attribute the cause of this difference to a ‘misplacement’ of the earlier grounding line position (Rebesco et al., 2014); however, given that only one in situ sediment core is available it is not possible to constrain the spatial variability of sediment cores within the localised area making it difficult to conclusively ascertain whether an anomalous sediment core data might have been collected. Without further investigation it is difficult to determine with confidence which dataset is correct; however, either way the wider implications of the disagreement are large. Dating the retreat of the Crane glacier grounding line to pre or post 2002, which both of these examples seek to do, changes our understanding of whether the collapse of the Larsen-B ice shelf should be attributed to either a marine based or atmospheric forcing mechanism.

1.3.2. Detecting Grounding Lines Using Quadruple Difference Interferometry

Quadruple difference interferometry (QDInSAR) provides a direct measurement of the relative displacement of the floating ice shelf surface, with unprecedented centimetre scale vertical accuracy and at a high (30 m) spatial resolution (Rignot, 1998a). The technique was first demonstrated using ERS-1 SAR data acquired over Petermann Glacier in North West Greenland (Rignot, 1996). A minimum of 3 SAR images acquired with a short (~3 day) temporal baseline are required in order to maintain sufficient interferometric coherence for a QDInSAR hinge line measurement to be made. The nominal 35-day repeat period of SAR missions such as ERS-1/2 and ENVISAT are too long to maintain phase coherence over fast flowing ice stream regions. Suitable data has largely only been acquired during the two European Remote Sensing (ERS) satellite 3-day repeat Ice Phases and 1-day repeat Tandem campaigns in 1991 – 1992, 1993 – 1994, 2011 and 1995 – 1996 respectively. Other useful datasets have been acquired by ALOS PALSAR and RADARSAT. Consequently, over the last 25 years it has not been possible to make widespread measurements of change in grounding line position using QDInSAR, and for the majority of the Antarctic ice sheet margin only a single measurement at one epoch has been made (Figure 1-5). The high precision of the QDInSAR technique means that when suitable data is acquired, this is the only method that has been successfully used to measure recent grounding line retreat (Rignot et al., 1998b; Park et al., 2013; Rignot et al., 2014).

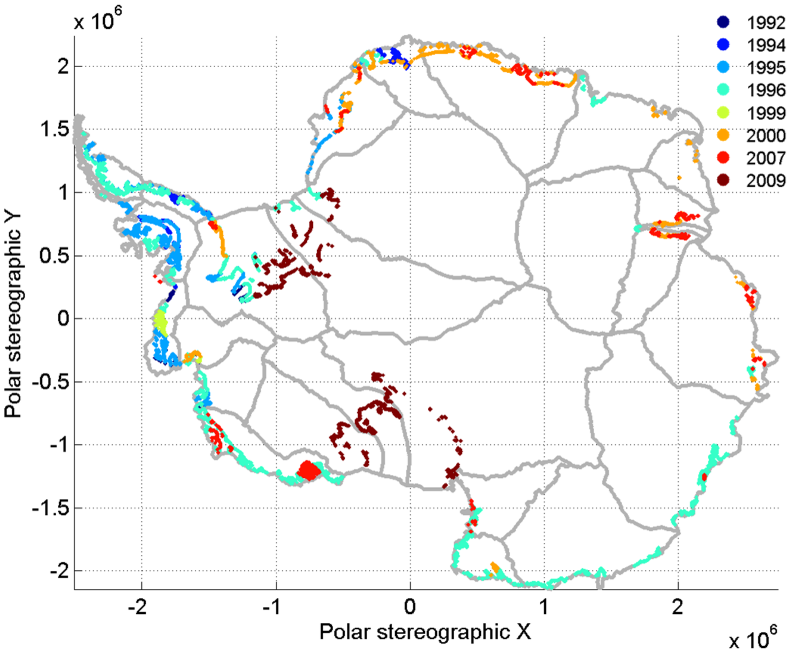

Figure 1-5. *Measurements of the grounding line position made by QDInSAR between 1992 and 2009 (Rignot et al., 2011), Antarctic drainage basins are also annotated (grey line) (Zwally, 2012).*

The following high level steps summarise the QDInSAR method for measuring grounding lines:

- Apply orbital corrections, instrument calibrations and image co-registration to SAR images
- Estimate the Interferometric baseline and perform common band filtering in order to generate a coherent interferogram
- The phase component of the complex interferogram is influenced by the curved Earth contribution, topographic signal, surface displacements, atmospheric delays and phase noise. The interferogram is flattened to remove the curved Earth contribution and filtered in order to reduce phase noise
- Topographic phase signal is simulated from a Digital Elevation Model (DEM) and the SAR imaging geometry, and then is subtracted from the interferogram forming a differential interferogram (DInSAR).
- A second DInSAR image is generated using a different master and slave SAR pair and this is then differenced against the first DInSAR image to remove the phase signal associated with constant ice flow, forming a quadruple difference interferogram

(QDInSAR). The QDInSAR image now contains the differential phase signal which on floating ice streams is largely caused by tidal motion, enabling the grounding line to be determined.

- The QDInSAR image can be unwrapped to retrieve the absolute phase difference

1.3.3. Detecting Grounding Lines Using Repeat Track Laser Altimetry

Repeat track laser altimetry has been used to measure the displacement of the floating ice shelf surface caused by ocean tides, relative to the mean surface elevation along a satellite ground track (Fricker and Padman, 2006). The technique uses laser altimetry data acquired by the Geoscience Laser Altimeter System (GLAS) instrument on board the Ice, Cloud and land Elevation Satellite (ICESat), to determine information about the structure of the grounding zone and location of the grounding line. ICESat has a footprint size of 70 m on the Earth's surface which measures the target surface elevation every 172 m along track (Zwally et al., 2002). In regions with large ocean tide amplitudes and where the satellite ground track is perpendicular to the grounding zone, relative surface displacement can be accurately measured by the laser altimetry footprint, enabling the landward and seaward flexure limits, and break in ice surface slope of the grounding zone to be observed (Fricker and Padman, 2006), along with 'ice plains, where they exist, (Brunt et al., 2010). Figure 1-6 provides an example of a profile of the absolute elevation and elevation anomaly across the grounding zone in the Filchner-Ronne ice shelf produced using this technique. Following calibration of the basic altimeter dataset, the Fricker and Padman (2006) method for measuring the grounding line from ICESat data can be implemented according to the steps outlined below

- Obtain geolocated footprint locations and ocean and load tide corrections from ICESat laser altimetry L2 Antarctic dataset (GLA12 product)
- Filter out cloud affected data, and radiometrically calibrate the return energy and receiver gain using the GLA01 product
- 'Re-tide' dataset using GOT99.2 tidal model correction originally applied to the ICESat data
- Apply saturation correction to elevation data where return energy is greater than receiver gain

- Interpolate each transect of elevation onto a common set of evenly spaced latitude values for each repeated track
- Calculate the mean elevation profile for all repeats
- Calculate the elevation anomaly for each repeat track by differencing the absolute elevation of each track from the mean profile

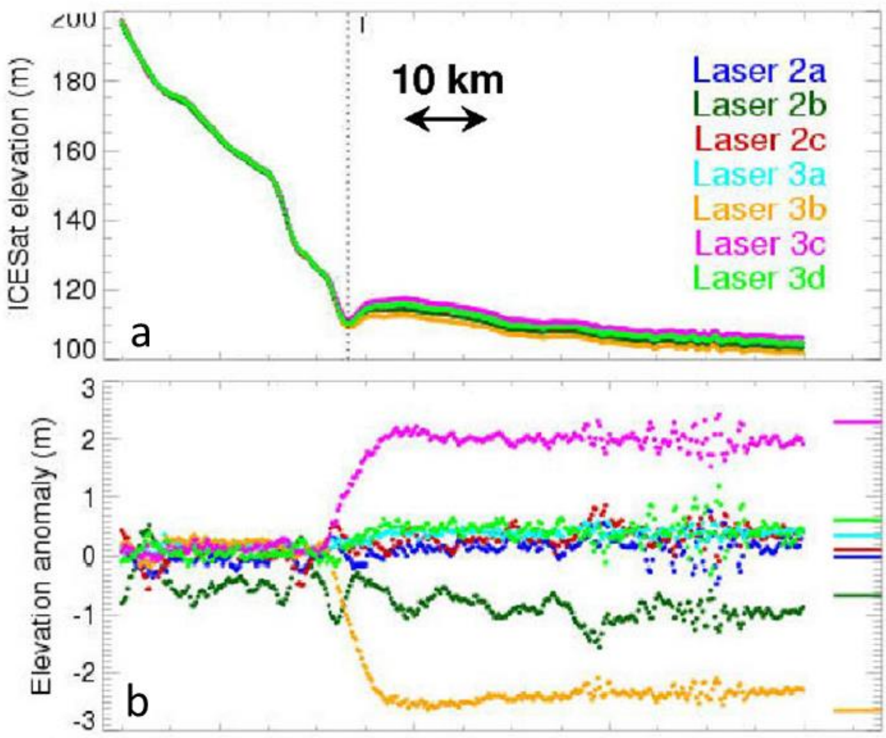

Figure 1-6. *a) Absolute ice surface elevation measured along an ICESat track across the grounding zone, b) elevation anomaly measured along the same track (reproduced from Fricker and Padman, 2006).*

The technique has been successfully used to map the grounding zone of the Filchner-Ronne ice shelf (Fricker and Padman, 2006), the Amery ice shelf, (Fricker et al., 2009) and the Ross ice shelf (Horgan and Anandakrishnan, 2006 and Brunt et al., 2010) (Figure 1-7). To date, only laser altimetry data acquired by GLAS has been used for grounding line determination because the small ground footprint of the sensor is well-suited to the task of detecting grounding line as it allows meter scale changes in surface elevation caused by the tide to be detected. As a consequence, it is only possible to establish the grounding line using this technique during the six years of ICESat mission operation (2003-2009), limiting the time period over which change in grounding line can be observed and preventing widespread inter-comparison of the QDInSAR and altimetry techniques.

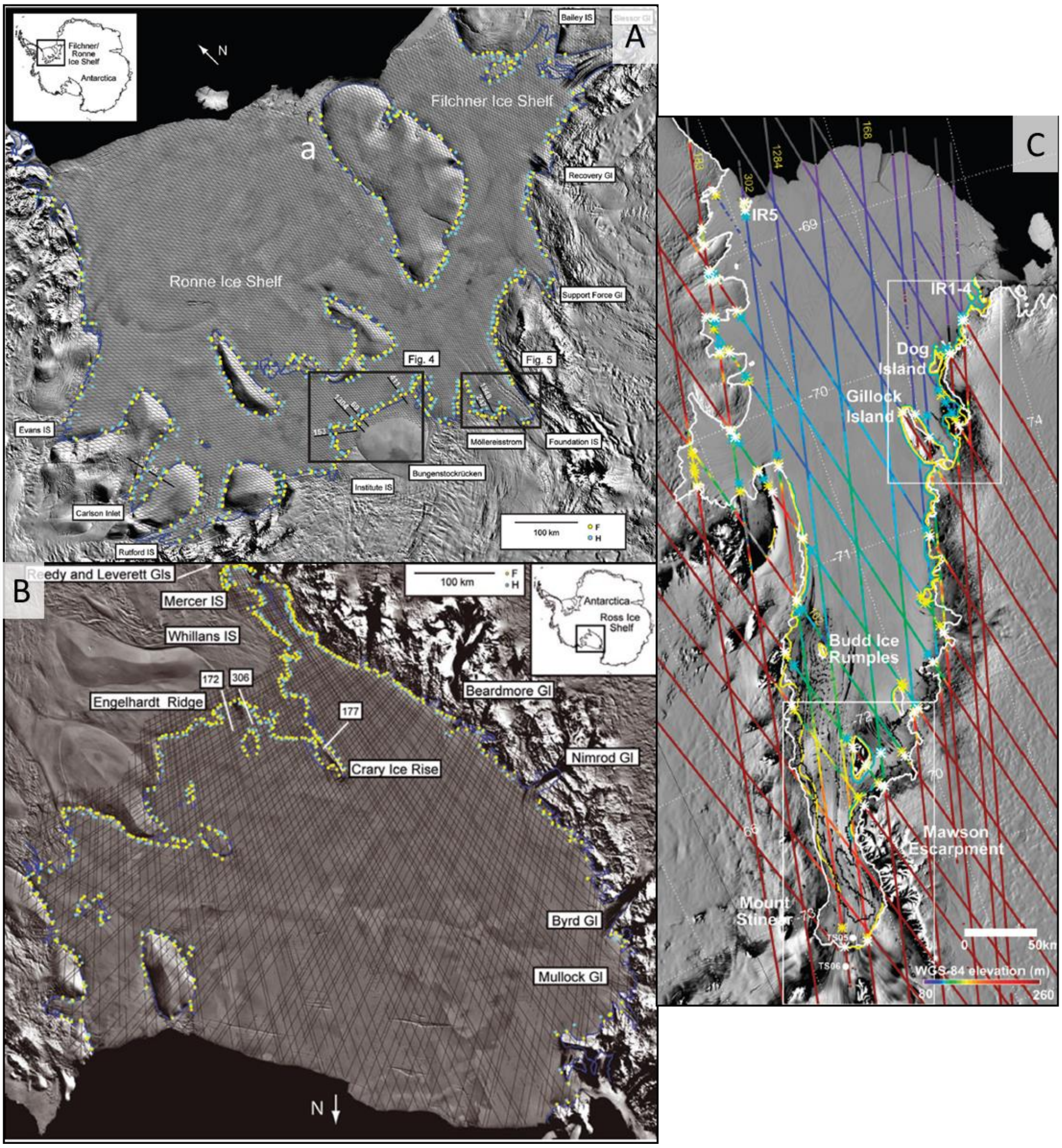

Figure 1-7. The grounding line position (blue dot) and point of floatation (yellow dot) measured in the Filchner-Ronne ice shelf (reproduced from Brunt et al., 2011) (a), the Ross ice shelf (reproduced from Brunt et al., 2010) (b) and the Amery ice shelf (reproduced from Fricker et al., 2009) (c) using repeat track laser altimetry.

In regions such as the Amundsen Sea Sector in West Antarctica, where rapid grounding line retreat has been observed (Park et al., 2013), the ocean tidal range is smaller and consequently vertical displacement of the floating ice shelf and the corresponding grounding line position has not been measured using the repeat-track laser altimetry technique. While the ice sheet hinge line has been mapped once using repeat track laser altimetry, change in hinge line position over time has not been observed which prevents the onset or evolution of dynamical imbalance around the ice sheet coastline from being detected using this technique. Pulse limited radar altimetry data has a larger (~3 km) diameter footprint, which encompasses a larger more topographically variable area on the ice surface, therefore it has yet to be demonstrated if this technique can be adapted to detect tidal displacement.

1.3.4. Detecting Grounding Lines Using Optical Shadow

The grounded ice sheet boundary has also be identified using topographic shadow visible in radiometrically calibrated optical Earth observation data, caused by the break in surface slope at the ice sheet – ice shelf boundary (Bindscahdler et al., 2011). This method is the only technique that has been used to map a continuous grounded ice boundary around the full Antarctic ice sheet (Figure 1-8 a); however, as the technique is reliant on manual delineation it is time consuming to produce and cannot be easily repeated to obtain a present day measurement of the grounded ice boundary or to accurately measure change. An intercomparison of the grounded ice boundary location produced from optical shadow, QDInSAR and repeat track laser altimetry showed discrepancies of up to 150 km in shallow slope regions such as ice planes or areas of fast flow (Rignot et al., 2011; Brunt et al., 2010), indicating that in some regions optical shadow may not be a reliable proxy for grounding line position.

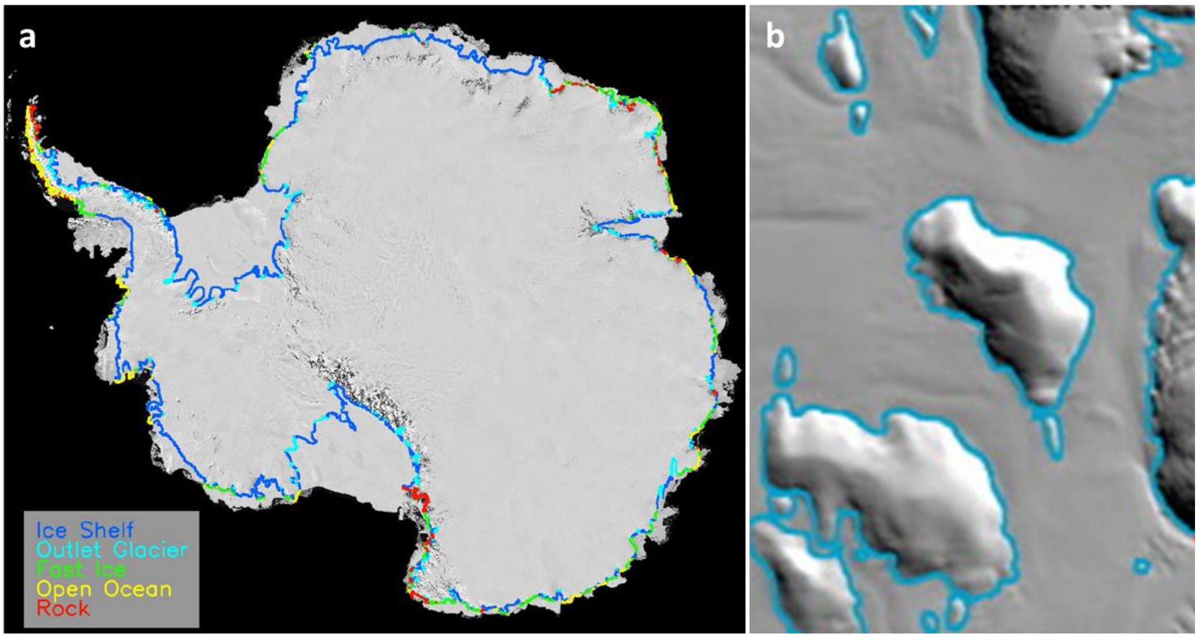

Figure 1-8. *a) Grounding line measured from manual delineation of the shadow boundary at the grounded ice boundary (reproduced from Bindschadler et al., 2011), b) an example of the shadow boundary.*

1.4 Aim

The aim of this thesis is to map change in the location of ice sheet grounding lines because they are an important glaciological parameter, using satellite Earth observation techniques and data acquired over the last 24 years. This aim is of significant importance because grounding lines determine the lateral extent of the ice sheet, the optimum location for mass balance flux gates, and provide evidence of dynamic instability; however, around the majority of the Antarctic coastline the grounding line has only been measured at one epoch during the last 25 years, and contemporary observations of grounding line retreat currently only exist in one sector of Antarctica. I will meet this aim by measuring grounding lines in Greenland and Antarctica using existing techniques such as Quadruple Difference Interferometry (QDInSAR), and by developing new techniques such as Differential Range Direction Offset Tracking (DRDOT) and break in surface slope from CryoSat-2. The results presented in this thesis are used to assess long term grounding line migration over the full 24 year period for which satellite Earth observation data is available, and short term grounding line migration which enables the likely controlling processes to be comprehensively assessed.

1.5 Objectives

The following list of objectives was devised to successfully address the aim of this thesis:

1. Apply the QDInSAR technique to measure the grounding line at a high spatial but coarse temporal resolution using ERS-1 and ERS-2 SAR data acquired between 1992 and 2011, and estimate the lateral precision of the technique.
2. Quantify motion of the hinge line on an ice stream using QDInSAR and perform a comprehensive assessment of the likely controlling process.
3. Develop and apply a new technique for detecting grounding lines in regions of low interferometric coherence, and estimate the lateral precision of the technique.
4. Develop a new technique for detecting the break in ice surface slope as a proxy for ice sheet grounding lines using CryoSat-2 Synthetic Aperture Radar Interferometric (SARIn) mode data.
5. Apply and validate the new CryoSat-2 break in slope technique to measure the grounding line location in topographically diverse sectors of Antarctica.

1.6 Thesis Structure

The remainder of this thesis seeks to fulfil the objectives. In Chapter 2 I present an overview of the Earth observation techniques I used to measure grounding lines, with a focus on interferometry as this was the only technique not newly developed during the course of the thesis. In Chapter 3 I present a 19 year time series of grounding line measurements made using QDInSAR from ERS-1 and 2 data. In Chapter 4 I present a new technique to map ice sheet grounding lines in incoherent SAR data using differential range direction offset tracking of SAR intensity features. In Chapter 5 I present a new method to detect the ice sheet grounding line as the break in surface slope, measured using synthetic aperture radar interferometric (SARIn) mode CryoSat-2 radar altimetry data. Finally in Chapter 6 I summarise the key science results presented in this thesis, and I discuss the opportunities for future work, including an example which shows that I have made the first steps towards measuring the grounding line position with Sentinel-1 for the first time.

Chapter 2

Methods

2.1 Methods Overview

This chapter provides an overview of the processing techniques used to produce the grounding line results presented in this thesis, which include; Quadruple Difference Interferometric Synthetic Aperture Radar (QDInSAR) in Chapter 3, Differential Range Direction Offset Tracking (DRDOT) in Chapter 4 and Synthetic Aperture Radar Interferometry (SARIn) mode CryoSat-2 data in Chapter 5. It is important to note that all three results chapters are structured in the format of scientific papers and therefore contain information on both methods and the results. As the DRDOT and CryoSat-2 processing techniques used in Chapters 4 and 5 were developed during this thesis, the methods are comprehensively described within the respective the results paper. Consequently, to avoid unnecessary repetition of text in this thesis, I present a high level summary of these processing chains in this chapter (Chapter 2), with references to the detailed methods descriptions in the results chapters. Conversely, QDInSAR, used in Chapter 3, is an established technique and the underlying algorithms used to produce an interferogram were not developed during this thesis. Further details on the theoretical basis for Interferometric Synthetic Aperture Radar (InSAR) can be found in Goldstein et al., (1993) and Hansen (2001). In this chapter I provide a more detailed description of the specific InSAR processing chain used in this thesis, because the QDInSAR method is not described in as much detail in the respective results paper (Chapter 3). All Synthetic Aperture Radar (SAR) datasets were processed using the GAMMA Remote sensing software (Werner et al., 2000).

2.2 Overview of the QDInSAR Method

The QDInSAR processing chain (Figure 2-1) is broken down into seven core sub-modules including Single Look Complex (SLC) image formation, coregistration of the SLC pair, formation of the interferogram, flat Earth and topographic phase signal removal, combination of two DInSAR images to form a QDInSAR image and finally phase unwrapping. After the QDInSAR processing is complete the final step of picking the ice sheet hinge line location at the inland limit of tidal flexure is performed. The QDInSAR method described in this section is stated more concisely, without examples at each stage of the processing chain, in Section 3.4 of results Chapter 3.

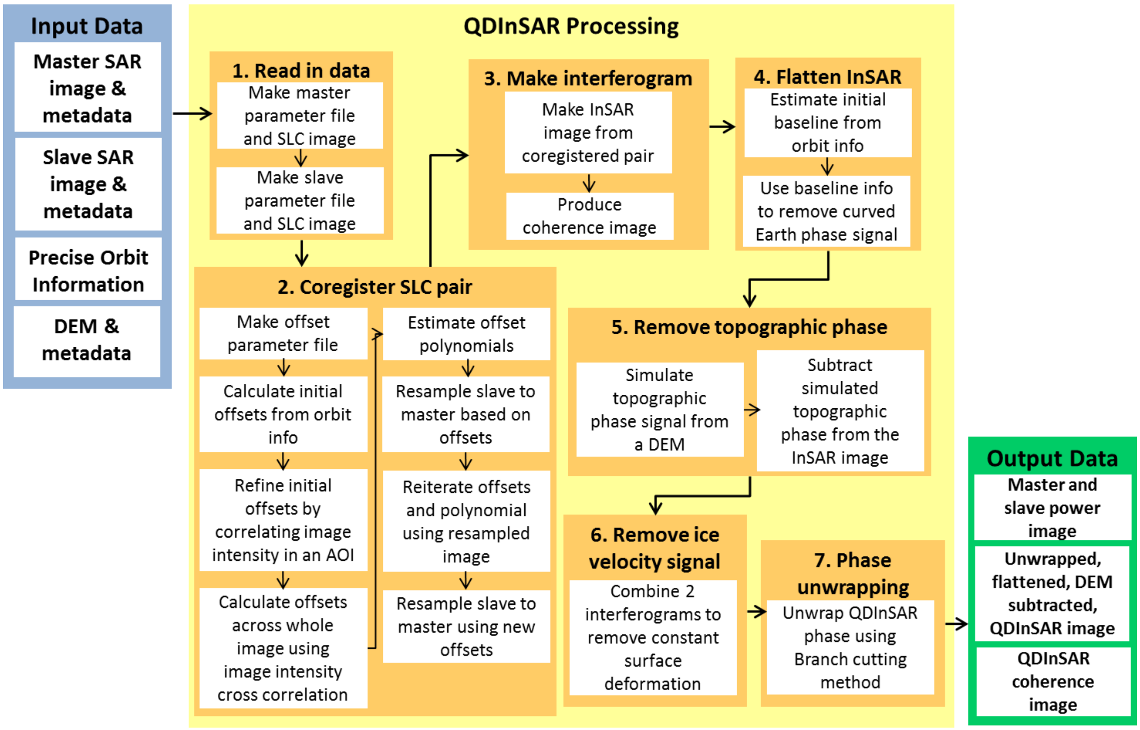

Figure 2-1. *An overview of the Quadruple Difference Interferometric Synthetic Aperture Radar (QDInSAR) processing chain.*

2.2.1. ERS-1/2 Synthetic Aperture Radar (SAR) Data

SAR data acquired by the European Space Agency's (ESA) European Remote Sensing (ERS) 1 and 2 satellites are used as the primary input dataset for the QDInSAR processing chain. Both satellites were maintained at a mean altitude of approximately 780 km above the Earth surface, in a ~91 minute sun-synchronous Polar orbit with a 98.5° inclination angle. The satellite inclination angle constrains the maximum latitude that observations can be made which for ERS-1/2 equals 82°. This is particularly important for ice sheet studies as there is a data gap, where no observations are made, at latitudes higher than 82° North and South. The ERS-1/2 SAR sensor is configured into a right looking viewing geometry with a 23° incidence angle at the centre of each swath. The ERS-1/2 SAR sensor is a C-band radar with a 5.3 GHz central frequency and a 5.6 cm wavelength. ERS-1 was operational for a 9 year period between 17.07.1991 and 10.03.2000, and ERS-2 was operational for a 16 year period between 21.04.1995 and 05.09.2011. Complex SAR data is comprised of an amplitude signal which is primarily controlled by the satellite imaging geometry, surface roughness and dielectric properties of the Earth surface; and a phase difference signal which is controlled by the satellite orbit configuration, curved Earth, surface displacement, surface topography, atmospheric delay and noise.

2.2.2. Formation of a Single Look Complex (SLC) Image

ERS-1 and ERS-2 data are processed from raw to Single Look Complex (SLC) images to retrieve the phase and amplitude measurement for every pixel in each 100km wide SAR image frame. Firstly, the accuracy of the orbit state vectors provided in the metadata of each image is improved by replacing them with precise orbit ephemeris provided by Department of Earth Observation and Space Systems (DEOS) (Scharroo and Visser, 1998) when available. The Doppler ambiguity is calculated to estimate the shift in central frequency caused by any offset in satellite pointing from 90° perpendicular to the direction of satellite travel. The raw data is autofocussed in the range and azimuth direction to form a complex SLC image which contains both the phase information and backscatter power of the return signal. The amplitude of the return SAR power is not homogeneous across the SAR frame as it is affected by relative factors such as the antenna pattern signal and the difference in travel path length of a wave in near and far range. A spatially-variable power correction is applied to each frame to remove non uniform power variations and then a constant offset is applied to produce an absolute radiometric calibrated power image.

2.2.3. SLC image pair Selection and Coregistration

Interferometric pairs were identified by combining temporally sequential SLC master and slave images formed from ERS-1 and 2 data acquired prior to 1997. However, in 2001 the remaining ERS-2 gyroscope failed leading to a degradation of the attitude stability of the satellite platform (Rosich et al., 2001). Non-zero yaw and pitch squint angles induce an offset in the Doppler centroid at which a SAR image is acquired. As the squint angle is not controlled it is not stable through time and therefore repeat SAR acquisitions are acquired at different Doppler centroid frequencies. When the Doppler centroid difference between a SAR image pair is greater than 800 Hz this leads to a reduced frequency spectrum overlap, which causes lower levels of interferometric coherence. Consequently, during the 2011 3-day campaign it is not always possible to pair images chronologically because low Doppler centroid differences are required to achieve high interferometric coherence. Instead, SLC image pairs were formed from data acquired in 2011 when the Doppler centroid difference was less than 800 Hz and for the image pair with the shortest temporal baseline up to a maximum of 9 days (Table 2-1).

Table 2-1. *2011 acquisition date, Doppler centroid per SAR frame and Doppler centroid difference per SAR pair, for ERS-2 data acquired over Petermann Glacier during the 2011 3-day repeat period. '*' denotes image pairs that were deemed viable for interferometry.*

SAR Date (MM_DD)		**05_16**	**05_19**	**05_22**	**05_25**	**05_28**	**05_31**	**06_03**	**06_06**	**06_09**
	Doppler Centroid (Hz)	***-498***	***-2067***	***292***	***-2444***	***-2910***	***-1868***	***-1952***	***-2254***	***-1597***
05_16	***-498***	0	1569	-790*	1946	-2412	1370	1454	1756	1099
05_19	***-2067***	-1569	0	-2359	377*	-843	-199	-115	187	-470
05_22	***292***	790	2359	0	2736	-3202	2160	2244	2546	1889
05_25	***-2444***	-1946	-377	-2736	0	-465*	-576*	-492	-190	-847
05_28	***-2910***	-2412	-843	-3202	-465	0	-1042	-958	-655	-1313
05_31	***-1868***	-1370	199	-2160	576	-1042	0	84*	386	-271
06_03	***-1952***	-1454	115	-2244	492	-958	-84	0	302*	-355
06_06	***-2254***	-1756	-187	-2546	190	-655	-386	-302	0	-657*
06_09	***-1597***	-1099	470	-1889	847	-1313	271	355	657	0

Out of the 9 SAR images acquired over Petermann Glacier during the ERS-2 2011 3-day repeat period, 7 viable image pairs existed (Table 2-1). Only 4 of these pairs have the optimum 3-day temporal baseline with the remaining 3 pairs having a 6-day temporal baseline. Once image pairs were selected the SLC images were formed by first detecting and removing missing lines of data in the input raw datasets, estimating the Doppler ambiguity using the Multi-Look Cross Correlation (MLCC) algorithm, determining the fractional Doppler centroid from the overlapping spectra of the image pair; estimating, pre-filtering and compressing the range power spectrum for each raw image, and finally autofocussing and azimuth compressing each image pair. Image pair co-registration offsets were first estimated from the orbital state vectors, and then coarse and fine image co-registration was performed by calculating the offset between using common features in the intensity backscatter image. Once the offsets have been calculated and refined the slave SLC is resampled to the reference geometry of the master SLC image.

2.2.4. Coherence Estimation and Interferogram Formation

Maintaining interferometric phase coherence in repeat pass SAR acquisitions is challenging over ice covered terrain because the surface rapidly deforms due to the ice flow and in response to changing meteorological events such as snow deposition, redistribution and melting (Figure 2-2). The nominal 35-day orbit repeat period of ERS-1 and 2 is typically too long to acquire viable (i.e. coherent) repeat-pass interferometric data over ice, and so both platforms have been moved into shorter repeat orbits during campaigns dedicated to this purpose. Between 28.12.1991 to 30.03.1992 ERS-1 was placed in a 3-day orbit repeat cycle (termed the first ice phase) and, after the success of this campaign, this was repeated in 1993/4 and in 2011 in order to acquire repeat measurements over Greenland and Antarctica. SAR data acquired by ERS-1 and 2 between 21.03.1995 to 05.06.1996, when both satellites orbited in tandem 35-day repeats, separated by 1-day, is also suitable for interferometry over ice covered regions as the short temporal baseline allows phase coherence to be maintained between SAR images acquired from both sensors. The QDInSAR results presented in this thesis were produced from ERS-1 and 2 data acquired during all 3-day ice campaigns and the 1-day tandem campaign, between 1992 and 2011.

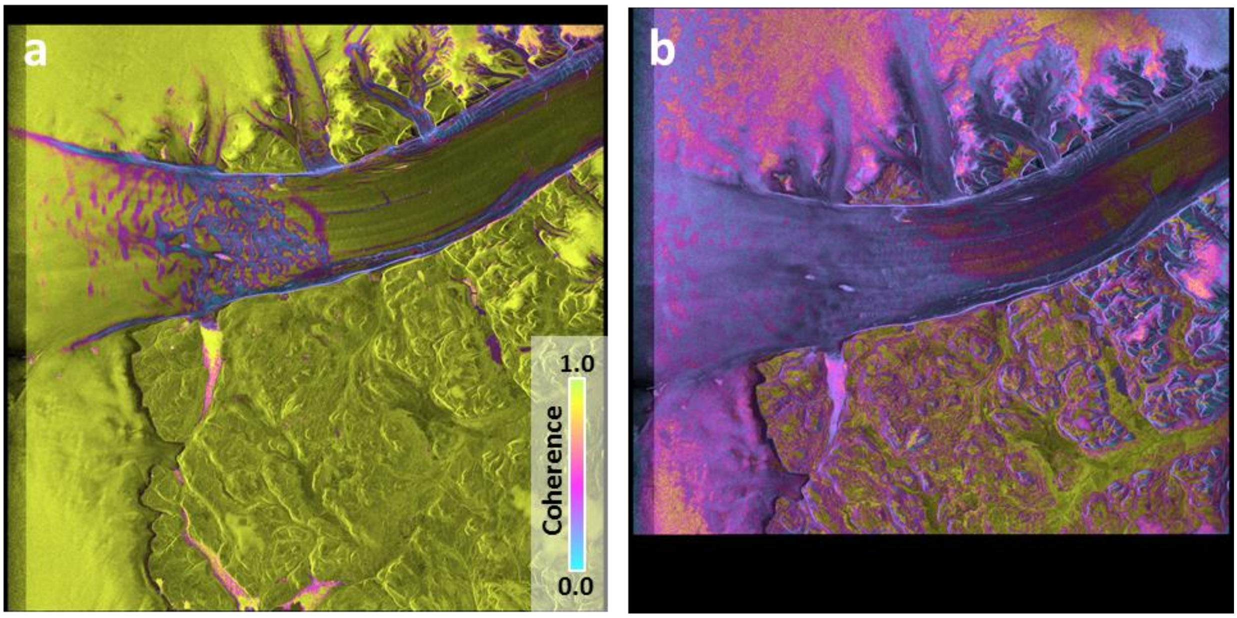

Figure 2-2. *a) Coherence image produced from an ERS-1 image pair with a short 3-day temporal baseline shows high coherence across the frame. b) Coherence image produced from an ERS-1 image pair with a longer 12-day temporal baseline shows a low level of coherence across the frame.*

To further investigate the effect of coherence degradation over time I examined a time series of 38 ERS-1 SAR pairs acquired over Petermann Glacier between 07.02.1992 and 20.03.1992, with 3, 6 and 12-day temporal baselines. The level of coherence was measured on three different glacial land cover types in the Petermann Glacier study area, which were identified using a band ratio classification of a Landsat-7 image acquired on 09.07.1999 (Figure 2-3a). The land types identified in the study area include the fast flowing 'ice stream', slow flowing 'ice sheet', and relatively stable 'exposed rock' (Figure 2-3b). The 'exposed rock' land cover type is primarily composed of rocky outcrops and soil with sparse vegetation in the summer and snow cover in the winter. Excluding the possibility of small landslides or subsidence events this land cover type is assumed to be stable and not subject to any large surface displacement processes. The 'ice sheet' land cover type consists of slow flowing land ice with speeds approximately 5% of the average ice velocity of Petermann Glacier (< 60 m/yr). The 'ice stream' land cover type is the fast flowing (~ 1 km/yr) main trunk of the Petermann Glacier and due to the band ratio classification used, it is largely in the summer ablation zone. Surface displacement on the 'ice stream' land cover type is large relative to the 'ice sheet' land cover type, and is caused by fast ice flow and vertical displacement by ocean tides on the floating ice shelf. The level of coherence on all three land cover types is affected by change in surface morphology caused by meteorological events such as snow melt, snowfall and blowing snow; however, this effect is particularly pronounced on the 'ice stream' and 'ice sheet' areas. However, air temperatures recorded at a nearby weather station during the winter 1992 study period when coherence is assessed, remained below -10 °C suggesting that surface melt is unlikely to have occurred.

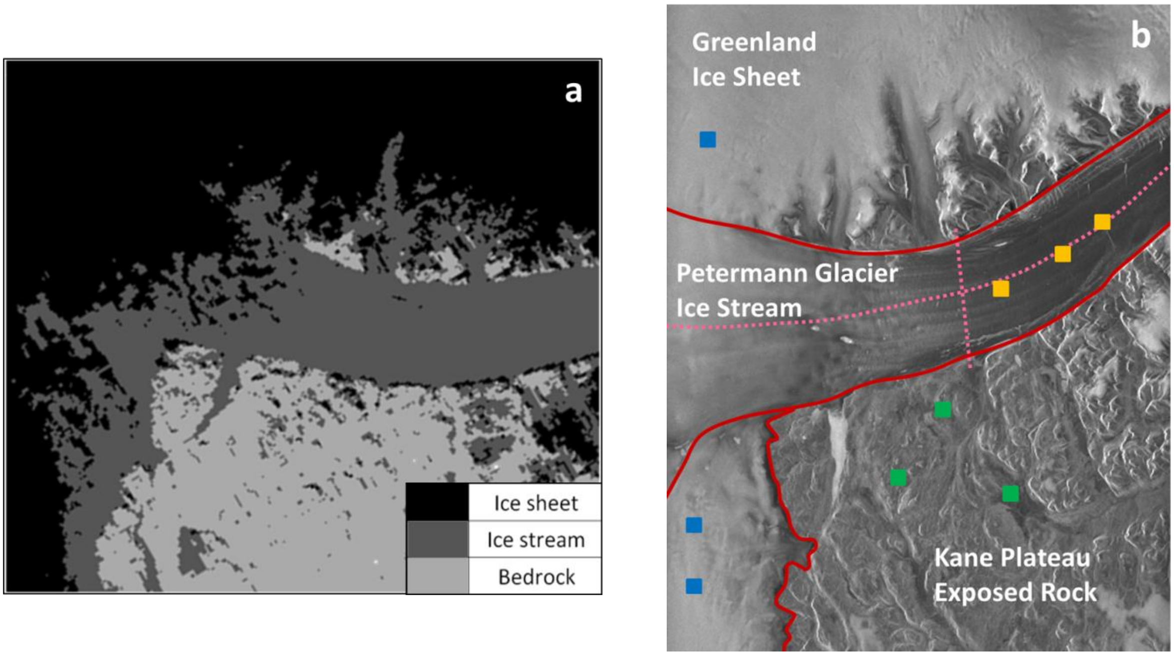

Figure 2-3. *a) Land surface classification performed using a ratio of the spectral bands in a Landsat image acquired on 09.07.1999 over the Petermann Glacier study area. b) Location of land surface types annotated on an ERS backscatter intensity image including the location of polygons where the coherence was extracted from (ice sheet is blue squares, green squares are exposed 'rock', ice stream is orange squares).*

Coherence was computed from the cross correlation coefficient of each of the 38 image pairs, and then the level of coherence was retrieved from polygons located on all three land surface types (Figure 2-3a). On all 3 land cover types a decrease in mean coherence was measured as the temporal baseline of the image pair increased (Figure 2-4). On the rock, ice sheet and ice stream land cover types the area greater than 0.7 coherence was 95 %, 88 % and 87 % for a 3-day baseline, 88 %, 70 % and 67 % for a 6-day baseline and 76 %, 43 % and 19 % for a 12-day baseline respectively.

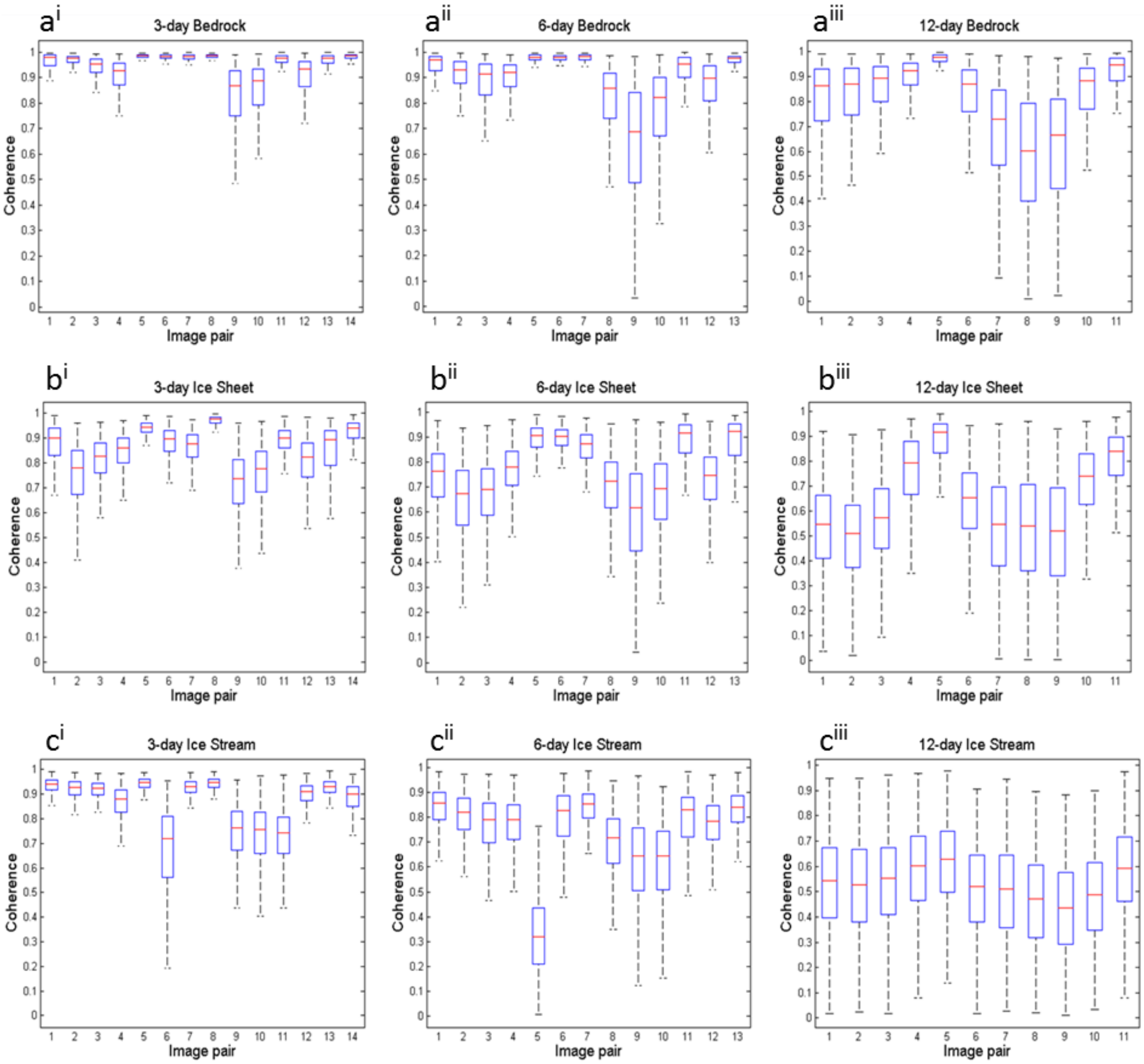

Figure 2-4. *Level of coherence extracted from the 'exposed rock' (a), 'ice sheet' (b), and 'ice stream' (c) land cover types in image pairs with 3 (i), 6 (ii) and 12(iii) day temporal baselines. The x axis shows the number of the image pairs in the time series and the y axis shows the level of coherence. The red bar shows mean coherence and the upper and lower bounds of the box represent the 75th and 25th percentile, while the dashed black vertical bars show the total spread of the coherence values.*

The perpendicular baselines of the 38 image pairs used in this study range between -200 m to +300 m for all but two image pairs. The temporal variability in the ERS-2 3-day perpendicular baselines (Figure 2-5), shows that image pairs with larger perpendicular baselines (> 100 m) do have lower coherence on all 3 land surface types, (e.g. InSAR pairs 9, 10 and 11 in Figure 2-4). However, in line with previous studies (Rott and Siegel, 1996), this is not as significant a factor in comparison with the universal decrease in coherence observed on all land surface types as the temporal baseline increases (Figure 2-4). These results confirm that coherence decreases as the temporal baseline of the SAR image pair increases, and furthermore decorrelation occurs more rapidly on land cover types with large rates of surface displacement (Figure 2-4). This illustrates the importance of selecting SAR data with a short temporal baseline when using coherence based techniques on ice covered terrain.

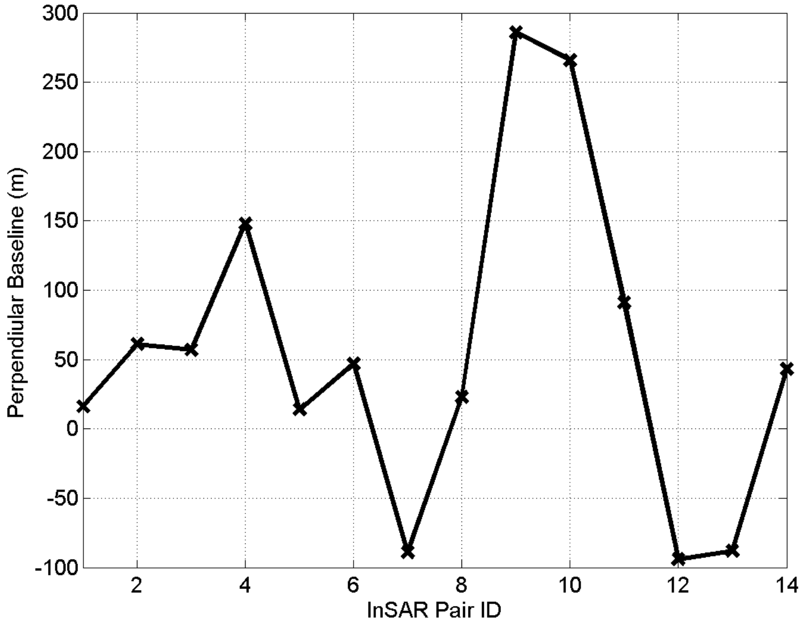

Figure 2-5. *Perpendicular baselines of all ERS-2 3-day InSAR pairs used in the coherence study.*

Interferograms are formed by multiplying the master SLC image with the complex conjugate of the slave SLC image on a pixel by pixel basis. The interferometric phase signal, the phase difference of the two images, contains a signal contribution from the Earth's curvature, topography, surface displacement, atmospheric delay and noise. For the purposes of this study we make an assumption that the influence of atmospheric delay on the phase signal is negligible because it is small relative to the phase difference caused by other factors such as ice flow.

2.2.5. Flat Earth and Topographic Phase Signal Removal

The perpendicular baseline is calculated from the orbital geometry of the image pair in order to estimate and remove the curved Earth phase signal from the interferogram (Figure 2-6). The topographic phase signal is also simulated from the orbital geometry, along with the surface elevation retrieved from an auxiliary Digital Elevation Model (DEM) (ASTER, 2009) (Figure 2-7) which has a mean elevation error of +8.3 m (Tachikawa et al, 2011). The magnitude of the topographic phase signal is dependent on the baseline of the image pair, with small baseline pairs having a low sensitivity and large baseline pairs having a high sensitivity to the topography. The phase sensitivity of an interferometric pair to topography is calculated from the altitude of ambiguity (h_a), which is a function of the wavelength (λ) and look angle of the sensor (Θ), the altitude of the satellite platform (R), and the perpendicular baseline ($B_\perp$) (Equation 1).

$$h_a = \frac{\lambda\, R \sin(\theta)}{2\, B_\perp} \tag{1}$$

The ERS-1 and 2 satellites both operated at a C-band wavelength of 5.6 cm with a look angle of 23°, and were maintained at a mean altitude of 850 km above the Earth's surface. For an InSAR pair with a 100 m perpendicular baseline, each fringe would therefore correspond to 93 m of topographic phase signal, whereas if the perpendicular baseline was doubled to 200 m each fringe would represent 47 m of topographic phase signal. This demonstrates that small baseline pairs have a low sensitivity and large baseline pairs having a high sensitivity to the topography. The consequence of this for measuring the grounding line is that error in removing the topographic phase signal from the QDInSAR image is likely to be larger for image pairs with a larger perpendicular baseline; however, as error in the DEM is less than 10 m, it is unlikely that this uncertainty would lead to a residual error greater than one InSAR fringe.

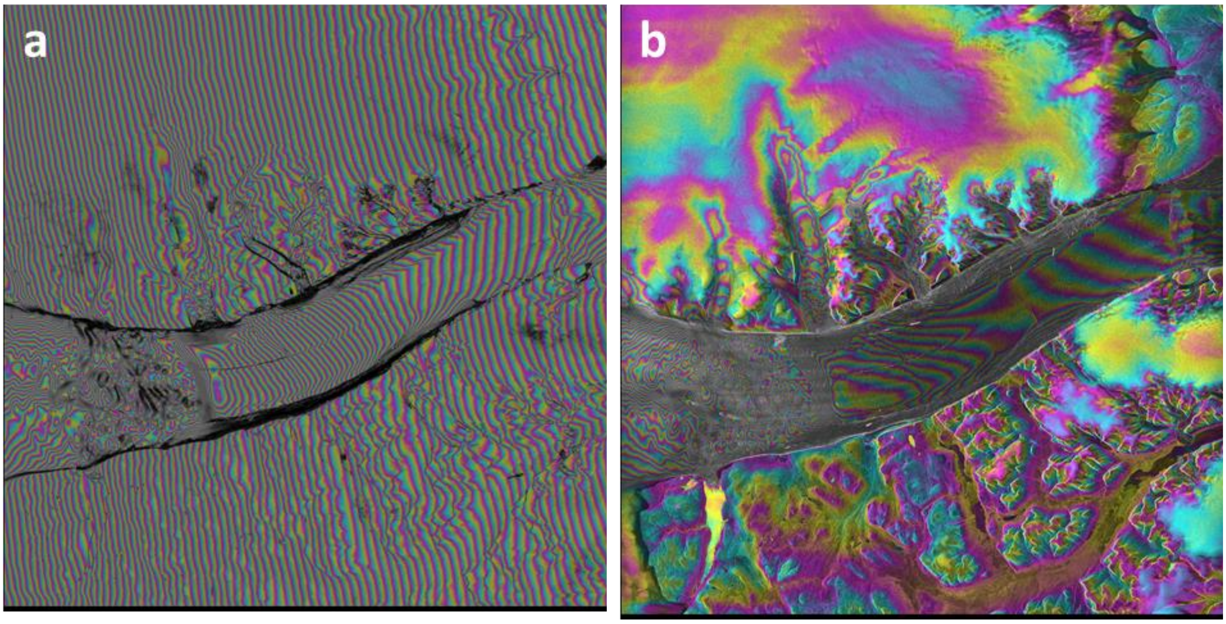

Figure 2-6. *a) Interferogram of Petermann Glacier with phase signal containing flat Earth, topographic, surface displacement and residual noise components. b) Interferogram once flat Earth phase signal has been removed.*

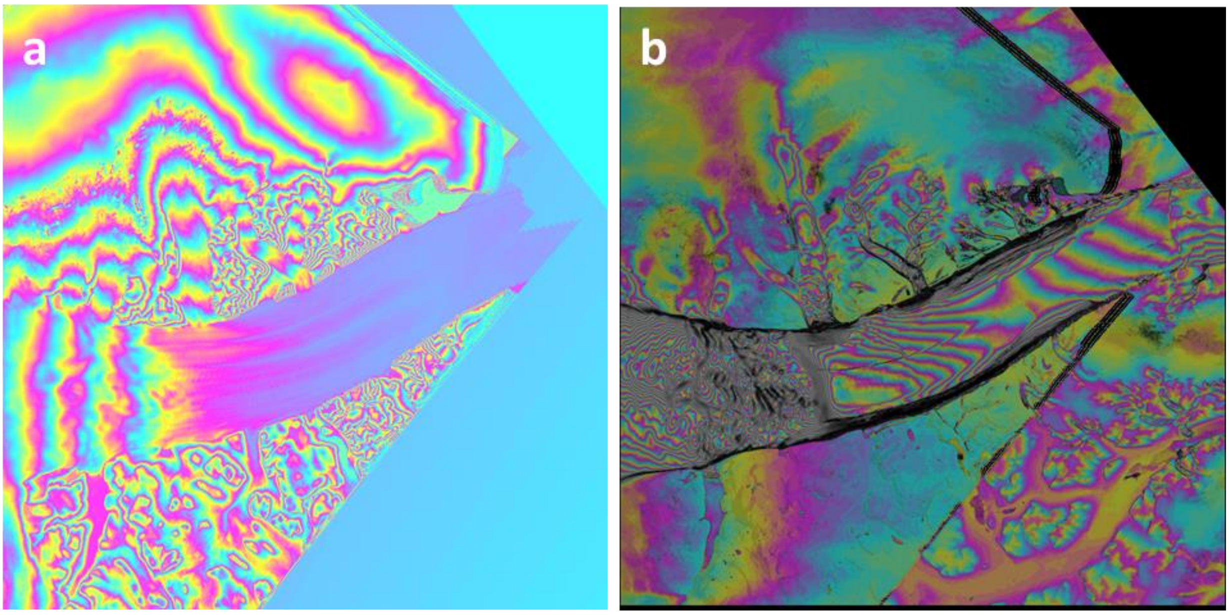

Figure 2-7. *a) Simulated topographic phase signal from the ASTER DEM (ASTER, 2009), b) interferogram of Petermann Glacier with phase signal containing only the surface displacement and residual noise components. Note, in regions outside of the DEM area the topographic phase signal is retained in the interferogram.*

2.2.6. QDInSAR Formation

At the Petermann Glacier surface displacement is caused by ice flow and, in floating sections, by ocean tides. We combine interferogram pairs to remove the common phase signal caused by constant ice flow, forming a quadruple difference interferogram (QDInSAR) (Rignot et al., 1998a). This method assumes that there is no difference in the horizontal motion contained in each InSAR pair, for example, that there is no real speed up or slowdown in the velocity of the ice stream observed in either interferogram. I minimised the likelihood of introducing error caused by residual horizontal velocity differences by combining InSAR images that were produced from data acquired with a temporal separation of a few weeks. Seasonal ice velocity change can occur on some tidewater glaciers within a few weeks; however, the ERS Ice Phase acquisitions took place during winter when rapid increases in speed are unlikely to occur. Furthermore, no previous studies have observed any long term annual change in the ice velocity of Petermann Glacier, reducing the likelihood that a real change in ice velocity may have been observed and introduced as an error in the QDInSAR images. If the ice speed signal is not fully removed from the QDInSAR image then it is also likely to be more gradually distributed across the interferogram, rather than concentrated at the grounding zone giving the appearance of additional fringes which may lead to errors in measuring the location of the grounding line. The remaining phase signal which I assume to be purely vertical, is manifest as a dense band of interference fringes at the boundary between grounded and floating ice and is caused by vertical displacement of the floating ice shelf by ocean tides.

2.2.7. Phase Unwrapping

I unwrapped the quadruple difference interferograms across the grounding zone to calculate the absolute displacement in the satellite line of sight. The phase unwrapping procedure was performed using the branch cut method (Goldstein et al 1988) which was initiated from a seed location on the grounded portion of the ice stream in each differential interferogram to ensure that there is no offset between the real and measured absolute displacement signal. It was not possible to initiate phase unwrapping in the same location in all instances due to temporal decorrelation of the SAR imagery inland of the glacier grounding zone which is lost over even short 3 and 1-day temporal baselines. Areas of low coherence also limit the areal extent of interferometric data in other locations, necessitating the use of manually selected bridges to link areas of disconnected phase in some places. The unwrapped surface displacement was converted from Line of Sight (LOS) to vertical displacement using the satellite geometry and 23° look angle. The absolute vertical displacement signal measured the QDInSAR directly corresponds to the surface elevation change between the two input interferograms.

2.2.8. Picking the Grounding Line from a QDInSAR Image

In quadruple difference interferograms the grounding zone is seen as a dense band of InSAR fringes across the ice stream approximately perpendicular to the direction of ice flow. The grounding line is picked by manually delineating the inland limit of tidal flexure as described by (Rignot et al., 2014) (Figure 2-8). In order to improve the repeatability of the result and ensure a consistent approach was applied to all datasets a set of protocols were followed when manually delineating the grounding line.

1. The interferogram is converted to a geotiff and loaded into a geographic information system software package.
2. The grounding zone is visually identified in the interferogram by locating the dense band of InSAR fringes.
3. Zoom in to the interferogram so the individual pixels are resolved, but so that the first 3 fringes in the vicinity of the grounding line can still be resolved.
4. Manually pick a line along the most inland full InSAR fringe, selecting individual points as frequently as possible.
5. Extract the latitude and longitude coordinates at each of the points and export as a text file.

When a displacement profile is extracted across the grounding zone (Figure 2-8), the inland grounded ice shows no significant vertical displacement, with a mean absolute variability of 3.7 cm, whereas the floating ice shelf seaward of the grounding line (green vertical line) shows over 1 meter of vertical displacement.

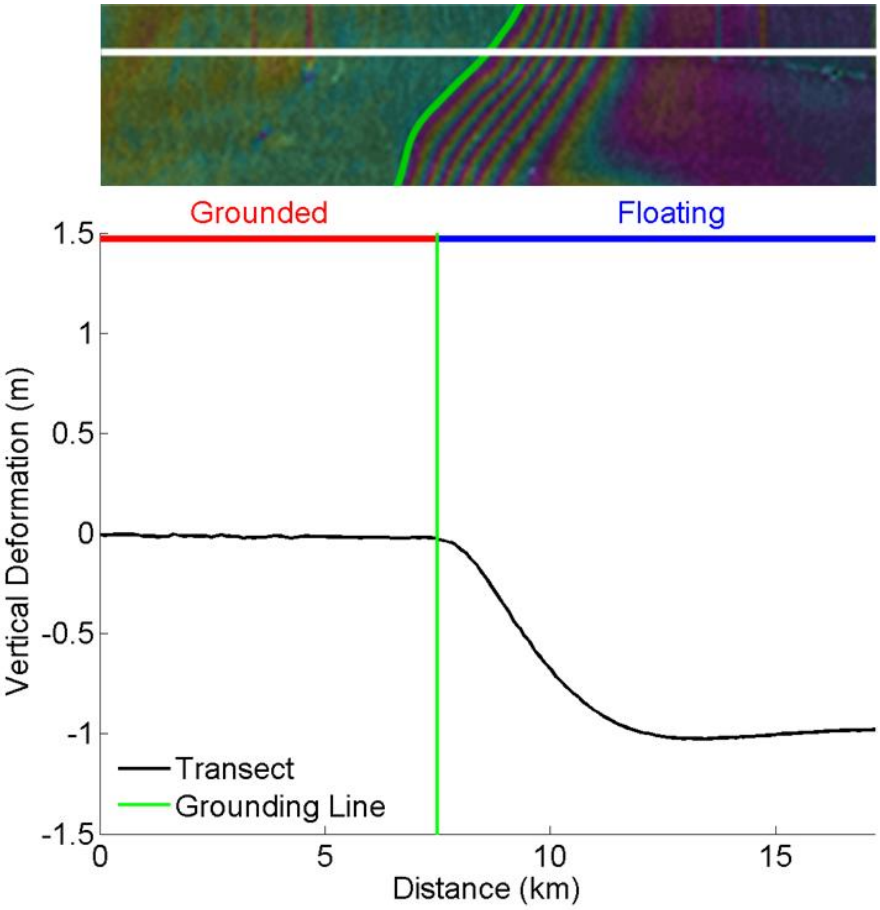

Figure 2-8. *Quadruple difference interferometric fringe pattern across the grounding zone of*

Petermann Glacier. The grounding line location (green) is identified as the inland limit of tidal flexure as seen in a profile of differential vertical displacement (black) extracted along a transect (white).

The inland limit of tidal flexure is more difficult to identify in differential interferograms with a lower fringe density because the magnitude of the vertical displacement signal is smaller; however, the fringes that are present are spread over approximately the same grounding zone width (Figure 2-9). The grounding zone width is defined as the distance between the grounding line, the inland limit of flexure, and the seaward limit of tidal flexure where the floating ice shelf reaches hydrostatic equilibrium with the ocean. This feature is clearly visible in an interferogram as the inland and seaward limit of the dense band of InSAR fringes (Figure 2-8). The seaward limit of tidal flexure is manually delineated using the same procedures used for picking the grounding line; however, there is greater uncertainty in the location of the seaward flexure limit with respect to the inland limit because gradient of the change in displacement is more gradual and occurs over a ~50 % longer distance (Figure 2-8). This shows that for all differential tide amplitudes greater than ±0.3 m the mean width of the grounding zone is 4.7 km with a 0.98 km range of variability. For differential tide amplitudes less than ±0.3 m the mean width decreases to 3.8 km with a much greater 2.8 km range of variability.

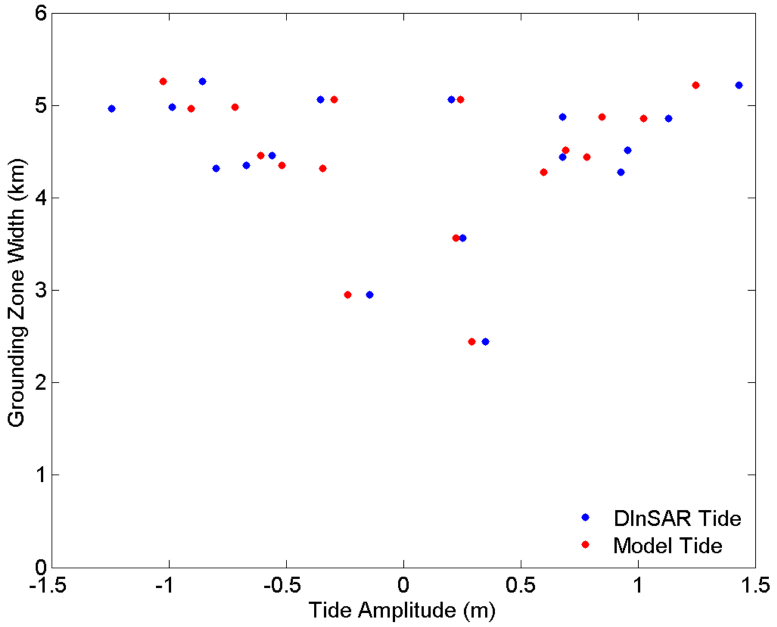

Figure 2-9. *The width of the Petermann Glacier grounding zone measured from the QDInSAR images, shown relative to the modelled differential tide and the relative displacement of the floating ice shelf*

measured in an unwrapped QDInSAR image.

The presence of fewer fringes results in a less abrupt boundary at the inland limit of flexure between the vertically deformed ice shelf and stable grounded ice. To investigate the impact that fringe density might have on the accuracy of the grounding line location picked, I scaled the wrapped phase signal in each differential interferograms by 2 to 4 times π to increase the number of InSAR fringes (Figure 2-10). The grounding zone is clearly visible as a dense band of fringes across the ice stream in the original interferogram (Figure 2-10a); however, as noise within the QDInSAR image is scaled at the same rate as the displacement signal, this eventually saturates the QDInSAR image rendering the grounding zone undetectable (Figure 2-10d). I phase scaled a number of the QDInSAR images until the fringe density in the grounding zone was as high as possible before becoming obscured by noise and then I re-picked the inland limit of tidal flexure. When I compared the grounding line locations delineated from the original and phase scaled DInSAR images I found that there was no visible change in the grounding line location measured (Figure 2-10) therefore I used the original hinge line location throughout the rest of this thesis.

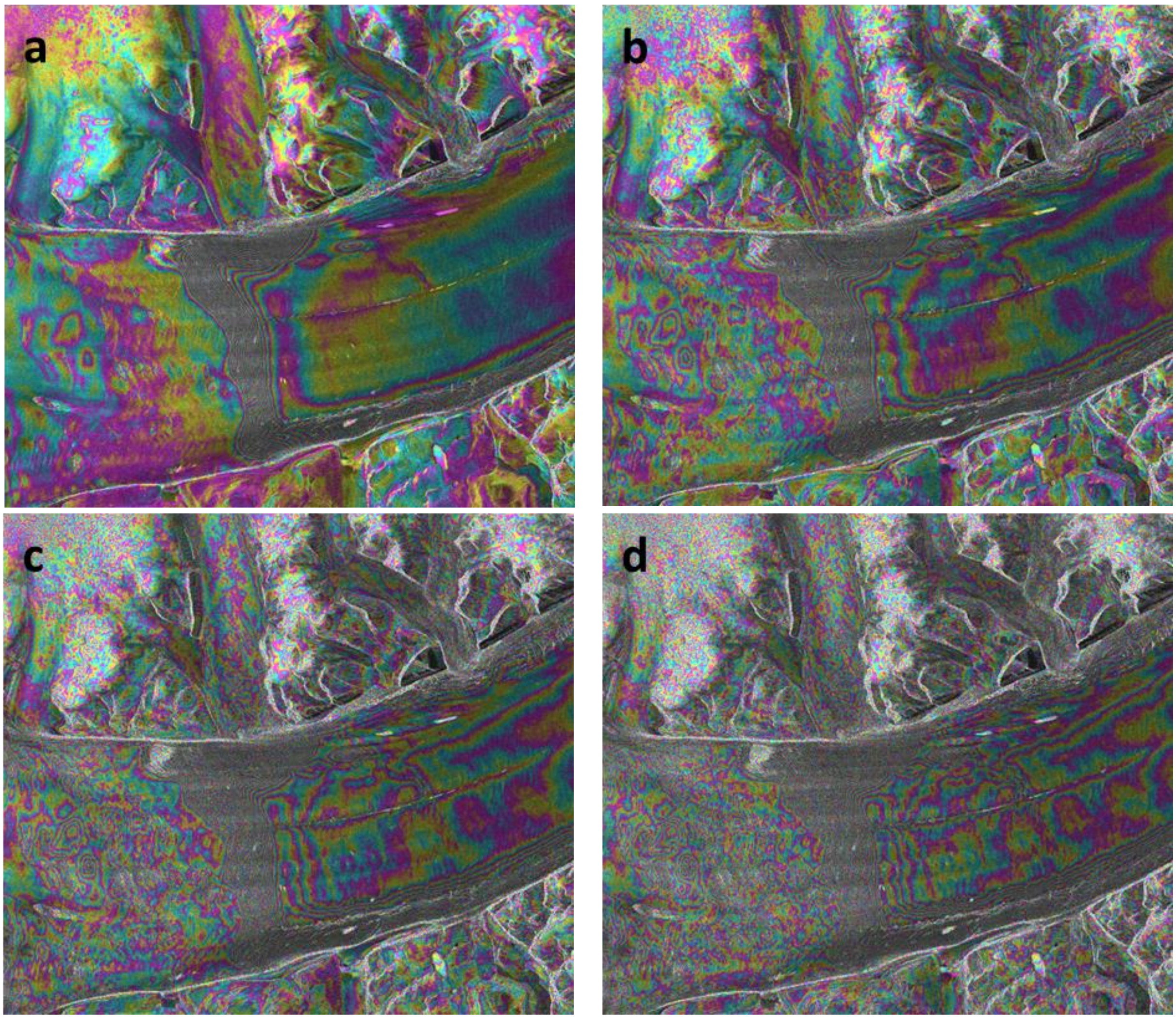

Figure 2-10. *a) The original QDInSAR image, and the QDInSAR image with the phase signal multiplied by 2 (b), 3 (c) and 4 (c) times the original value.*

2.3 Overview of the DRDOT Method

The DRDOT processing chain (Figure 2-11) is broken down into five core sub-modules including reading in the TerraSAR-X SLC data, masking and then coregistering the SLC pairs, intensity feature tracking and calculation of differential range direction offsets and finally picking the ice sheet grounding line.

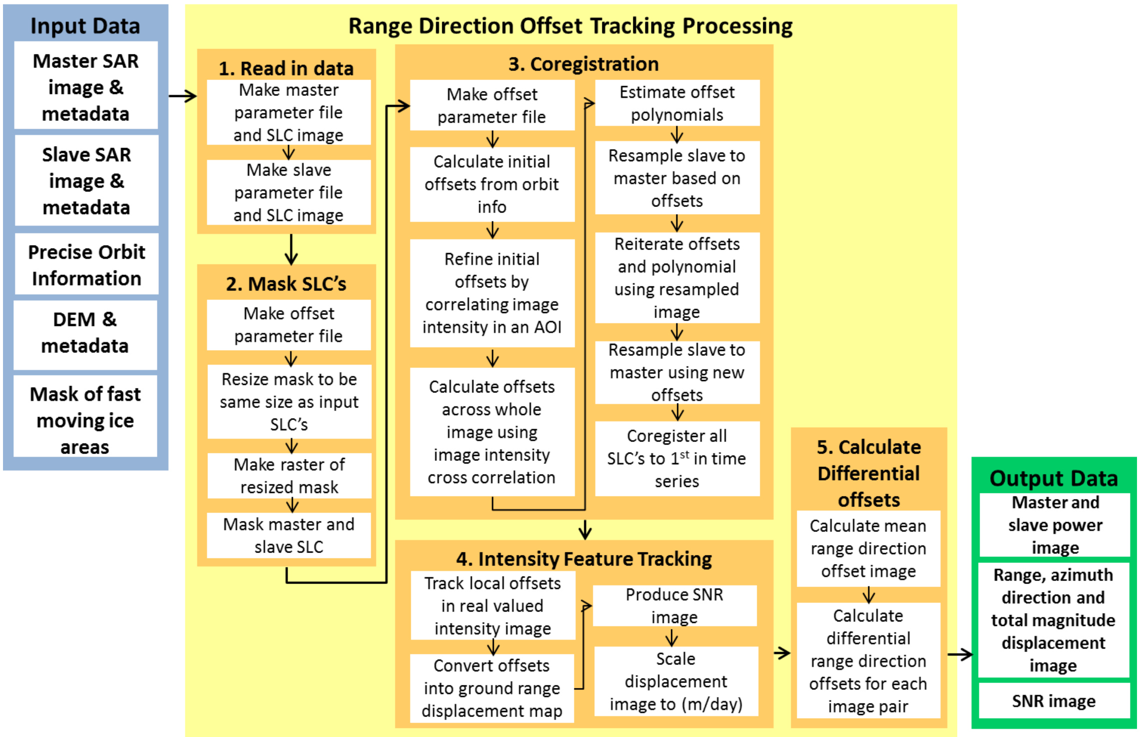

Figure 2-11. *An overview of the Differential Range Direction Offset Tracking (DRDOT) processing chain.*

The DRDOT method is comprehensively documented in the results Chapter 4 as described in Table 2-2.

Table 2-2. *Section references where a comprehensive description of the DRDOT methods are found.*

DRDOT Processing Modules	Chapter	Section
Read in data	4	4.4.1. Synthetic aperture radar data
Mask SLC's	4	4.5.1. Tracking ice motion
Coregistration	4	4.5.1. Tracking ice motion
Intensity feature tracking	4	4.5.1. Tracking ice motion
Differential range direction offset tracking	4	4.6.1.1. Differential range direction offset tracking
Picking the grounding line	4	4.6.1.2. Delineating the grounding line

2.4 Overview of the CryoSat-2 Method

The CryoSat-2 processing chain (Figure 2-12) is broken down into three core sub-modules which include pre-processing correction and gridding, iterative plane fit and grounded ice boundary delineation sub-modules.

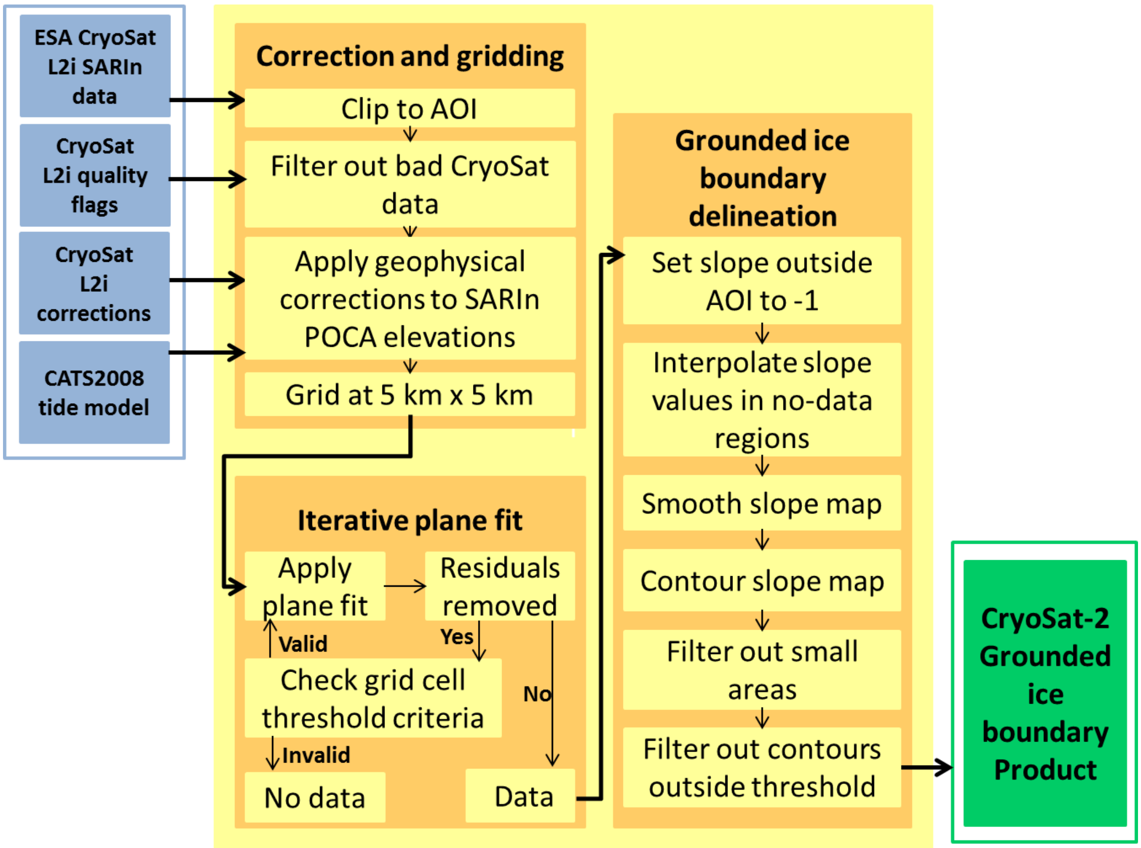

Figure 2-12. *An overview of the CryoSat-2 processing chain.*

The CryoSat-2 method is comprehensively documented in the results Chapter 5 as described in Table 2-3.

Table 2-3. *Section references where a comprehensive description of the CryoSat-2 methods are found.*

CryoSat-2 Processing Modules	Chapter	Section
Correction and gridding	5	5.3. CryoSat-2 data
Iterative plane fit	5	5.5.1. Computing ice sheet surface slope
Grounded ice boundary delineation	5	5.5.2. Identification of the break in surface slope

Chapter 3

Grounding line migration from 1992 to 2011 on Petermann Glacier, North West Greenland

3.1. Abstract

We use satellite radar interferometry to investigate change in location of the Petermann Glacier grounding line between 1992 and 2011. The location was identified in 17 quadruple-difference interferograms produced from ERS-1/2 data - the most extensive time-series assembled at any ice stream to date. There is close agreement (20.6 cm) between interferometric vertical displacement and relative tide amplitudes simulated by the AODTM-5 Arctic tide model. Despite reported ice shelf thinning and episodes of large iceberg calving, the location of the 4.4 km wide groundling zone has remained stable over the 19-year survey period, with no obvious trend over time. Of the 0.5 ± 0.03 km grounding line migration observed we estimate that 34 % can be attributed to change in tide amplitude; however, all of the observed horizontal displacement can be accounted for by 2 ± 3 m of ice thickness change which is modest (29 %) in comparison with observed local terrain variability. We estimate that the Petermann Glacier grounding line position can only be determined with an accuracy of 810 m, reinforcing the importance of repeatedly measuring grounding line locations when attempting to measure advance or retreat over time.

Over the 19-year period, the grounding line position varied by 0.5 km, on average, with no significant trend over time. Although tidal forcing explains a fraction (34 %) of the movement, localised variations in the glacier thickness could explain it all were they to alter the glacier’s hydrostatic balance as they advect downstream – a hitherto unconsidered possibility that would reduce the precision with which changes in grounding line position can be detected.

3.2. Introduction

Ice losses from Greenland and Antarctica have increased rapidly over the recent decades – by 278 % and 148 % respectively since 1992 - and the most pronounced changes have occurred in places where the ice sheets are grounded well below sea level (Shepherd et al., 2012). Such marine-based and marine-terminating ice sheet sectors are particularly vulnerable to environmental change, because they are in contact with atmospheric and oceanic masses that are relatively warm, where modest changes in temperature can melt and destabilise the ice. In the most rapidly changing regions, such as the Amundsen Sea sector of West Antarctica and Jakobshavn Isbrae in Western Greenland, warm ocean currents have triggered glacier retreat (Park et al., 2013), leading to increased rates of ice flow (Joughin et al., 2014a) and ice thinning (McMillan et al., 2014) far inland. Elsewhere, at the Antarctic Peninsula, for example, changes in air temperature are believed to be a driver (Scambos et al., 2000) of ice shelf collapse (Rott et al., 1996) which, in turn, has also triggered drawdown of inland ice (Rignot et al., 2004). Ice sheet grounding lines are therefore a sensitive indicator of dynamic instability, and modelling the rate and spatial pattern of future change remains one of the most significant challenges limiting the accuracy of sea level rise projections (Church et al., 2013).

An ice sheet grounding line is the junction between an ice shelf which floats on the ocean surface, and the ice sheet which is grounded on bedrock. In reality the grounding line is a transitory feature with a location that can fluctuate on short (sub-daily) timescales, for example due to the effects of ocean tides which alter the proportion of ice that floats. The grounding line is located at the base of the ice sheet whereas the hinge line location is the manifestation of this feature at the ice surface. Although there may be a small lateral variation in the position of the hinge and grounding line locations we can infer from elastic beam theory that their migration rates are directly correlated therefore tracking either is an accurate measure of grounding line motion or stasis (Rignot, 1996). Both junctions lie within a region called the grounding zone, which can be up to a few kilometres wide in the direction of ice flow depending on factors such as bedrock topography and tidal amplitude. The grounding zone is of critical importance for ice sheet stability, because it determines the rate at which ice is discharged into the oceans from inland (Schoof, 2007). In the absence of pinning points, grounding line retreat leads to a reduction in the resistive force acting to restrain the grounded ice, and consequently an increase in the rate of ice discharge. These effects have been observed and simulated (Joughin et al., 2010) to rapidly propagate ice drawdown from further inland. Relatively modest changes at the termini of outlet glaciers can therefore have a marked impact on the wider ice sheet mass imbalance.

Although ice sheet grounding lines can be detected using ground based techniques, such as kinematic Global Positioning System measurements of tidal flexure (Vaughan, 1995), they can be logistically difficult or impossible to access, and the high cost of repeated surveys limits the practicality of this approach on large scales. Because of this, techniques based upon satellite observations have emerged as an alternative solution, enabling relatively large quantities of data to be regularly acquired. Three independent Earth observation techniques have been employed to date; the detection of shadow caused by the break in ice sheet surface slope in optical imagery (Bindschadler et al., 2011), and the detection of tidal motion in quadruple difference interferometric synthetic aperture radar (QDInSAR) observations (Goldstein et al., 1993) and repeat satellite altimeter measurements (Fricker and Padman, 2006). It has been shown (Rignot, 1998a) that the technique of QDInSAR is capable of detecting grounding line locations with fine (30 m) spatial resolution and with high precision. However, the temporal sampling frequency of the technique is limited, because of the relative infrequency with which suitable SAR image triplets are acquired; typically, at least three SAR images acquired within a few days are needed. The most useful QDInSAR data were acquired during periods when the two European Remote Sensing (ERS) satellites were orbiting in 3-day and tandem repeat cycles, between 1991 and 1992, 1993 to 1994, in 2011, and between 1995 and 1996, respectively.

3.3. Petermann Glacier Study Area

Petermann Glacier is a large marine terminating ice stream located on the North West coast of the Greenland Ice Sheet at 81°N and 62°W (Figure 3-1). It drains around 4% of the total ice sheet area (Munchow et al., 2014) and is one of only seven ice streams in Greenland with a permanently floating section (Moon et al., 2012). Inland, Petermann Glacier is grounded on bedrock more than 300 m below present day sea level and its 1280 km^2 floating ice tongue flows through a steep sided, 20 km wide fjord into the Hall Basin in the Nares Strait. Satellite observations of surface elevation change inland of the Petermann

Glacier grounding line show a moderate rate of thinning (0.3 m/yr) for the period 2003 to 2007, of which 50 % is directly attributed to a negative surface mass balance anomaly (Pritchard et al., 2009). Episodic calving events in 1992, 2010 and 2012 (Nick et al., 2012; Munchow et al., 2014), have decreased the length of the floating ice shelf by ~40 %. However, there is no evidence to suggest that these calving events are occurring with greater frequency, or that they have affected the glacier speed, which has remained steady at ~1 km/yr in the fastest regions (Nick et al., 2012). This is in part because, at Petermann Glacier, high rates of channelized basal melting remove the vast majority (80 %) of floating ice before calving can occur, making ice-ocean interactions the dominant control on ice mass imbalance (Rignot and Steffen, 2008). Although ship-based studies confirm that there is sufficient heat available within the fjord waters to drive the rapid rates of basal melting inferred from satellite observations (Johnson et al., 2011) it is not certain whether potential changes in ocean temperature, mixing, or sea ice cover might lead to additional melting potential, fuelling speculation that a warming ocean could trigger future grounding line retreat on Petermann Glacier (Johnson et al., 2011; Nick et al., 2013).

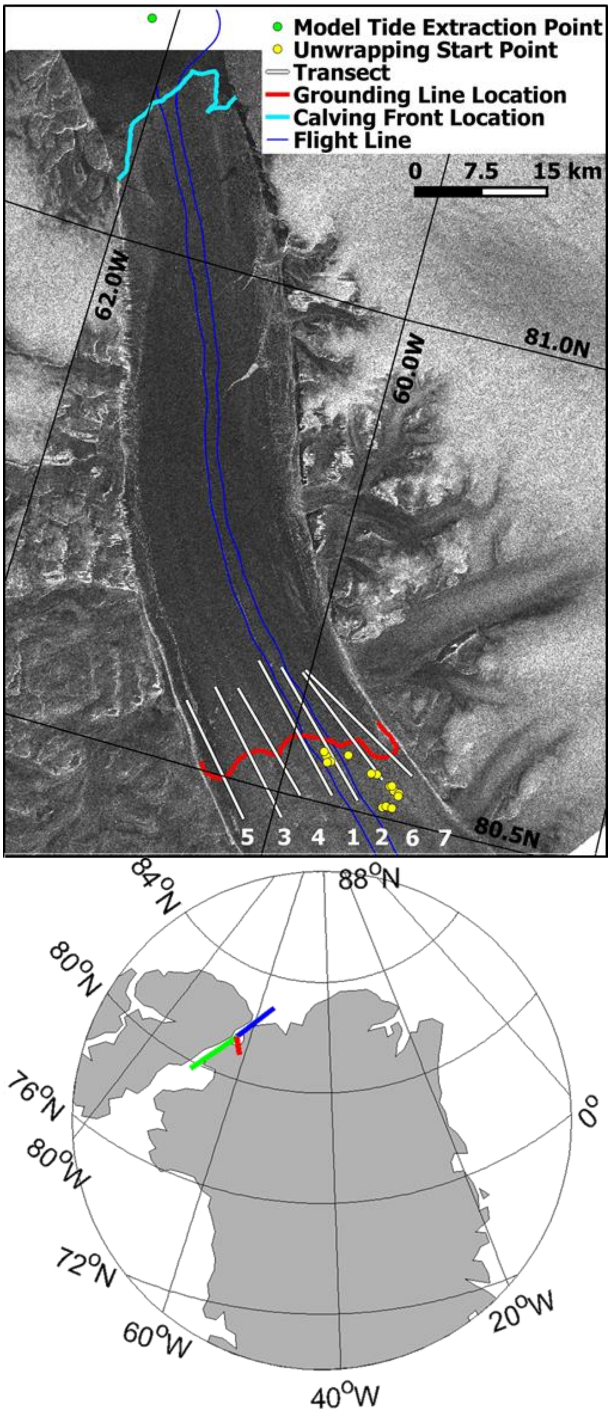

Figure 3-1 *Map of Petermann Glacier, a marine terminating ice stream in North West Greenland. The ice stream is shown by an ERS-1 synthetic aperture radar image, and flows from the bottom to top of the image. The approximate grounding line is shown in red, along-flow transects are marked in white, the calving front is shown in cyan, and ICEBridge flight-line 1 (West) and 2 (East) separated by 2.9 km is shown in blue. Also shown are the seed locations chosen for interferometric phase unwrapping (yellow), and for tide model heights (green). The inset shows the location of Petermann Glacier in Greenland and the location of the start and end points of the fjord (red) and Nares Strait (blue (North) and green (South)) tide model transects.*

3.4. Data and Methods

3.4.1. Synthetic aperture Radar Data

Maintaining interferometric phase coherence in repeat pass SAR acquisitions is challenging over ice covered terrain, because the surface rapidly deforms due to the ice flow and in response to changing meteorological events such as snow deposition and redistribution and melting. The nominal 35-day orbit repeat period of the European Space Agency's (ESA) European Remote Sensing (ERS) 1 and 2 satellites is typically too long to acquire viable (i.e. coherent) repeat-pass interferometric data over ice, and so both platforms have been moved into shorter repeat orbits during campaigns dedicated to this purpose. Between 28.12.1991 to 30.03.1992, ERS-1 was placed in a 3-day orbit repeat cycle (termed the first ice phase) and, after the success of this campaign, it was repeated in 1993/4 and in 2011 in order to acquire repeat measurements over Greenland and Antarctica. SAR data acquired by ERS-1 and 2 between 21.03.1995 and 05.06.1996, when both satellites orbited in tandem 35-day repeats, separated by 1-day, is also suitable for interferometry over ice covered regions as the short temporal baseline allows phase coherence to be maintained between SAR images acquired from both sensors. Here, we used ERS-1 and 2 data acquired on track 12, frame 1953 over Petermann Glacier during all 3-day ice campaigns and the 1-day tandem campaign, between 1992 and 2011 (Table 3-1), to produce measurements of the grounding line location.

Table 3-1. *Details of all SAR data used in this study, including sensor, track number, acquisition dates and temporal baseline. The data are listed in rows identifying each SAR frame element of the 17 quadruple difference interferograms used to detect grounding line locations (identifiable as GLL_01 through GLL_17).*

GL ID	Sensor	Track No.	Master 1 Date	Slave 1 Date	Master 2 Date	Slave 2 Date	Temporal Baselines
GLL_01	ERS-1	12	19920207	19920210	19920210	19920213	3, 3
GLL_02	ERS-1	12	19920210	19920213	19920213	19920216	3, 3
GLL_03	ERS-1	12	19920213	19920216	19920216	19920219	3, 3
GLL_04	ERS-1	12	19920216	19920219	19920219	19920222	3, 3
GLL_05	ERS-1	12	19920219	19920222	19920222	19920225	3, 3
GLL_06	ERS-1	12	19920222	19920225	19920225	19920228	3, 3
GLL_07	ERS-1	12	19920225	19920228	19920228	19920302	3, 3
GLL_08	ERS-1	12	19920228	19920302	19920302	19920305	3, 3
GLL_09	ERS-1	12	19920302	19920305	19920305	19920308	3, 3
GLL_10	ERS-1	12	19920308	19920311	19920311	19920314	3, 3
GLL_11	ERS-1	12	19920311	19920314	19920314	19920317	3, 3
GLL_12	ERS-1	12	19920314	19920317	19920317	19920320	3, 3
GLL_13	ERS-1/2	12	19951028	19951029	19960229	19960301	1, 1
GLL_14	ERS-2	12	20110603	20110606	20110606	20110609	3, 3
GLL_15	ERS-2	12	20110531	20110603	20110606	20110609	3, 3
GLL_16	ERS-2	12	20110516	20110522	20110519	20110525	6, 6
GLL_17	ERS-2	12	20110531	20110603	20110603	20110606	3, 3

3.4.2. Quadruple Difference Interferometry

We processed ERS-1 and ERS-2 data from raw to Single Look Complex (SLC) images using precise Department of Earth Observation and Space Systems (DEOS) orbit ephemerides (Scharroo and Visser, 1998) when available. Temporally sequential SLC master and slave image pairs were formed from ERS-1 and 2 data acquired prior to 1997 (Table 3-1). However, failure of the ERS-2 gyroscope in 2001 (Rosich et al., 2001) resulted in larger and less stable Doppler centroid frequencies, and so it is not always possible to pair temporally sequential images in data acquired during the latter period. To achieve high interferometric coherence low Doppler centroid differences are required to ensure sufficient spectral overlap, therefore in 2011 SLC image pairs were formed when the Doppler centroid difference was less than 800 Hz and when temporal baseline were less than 9 days. Each SAR image pair was co-registered using common features in the backscatter intensity images, with the aid of initial co-registration offsets determined from the orbital state vectors. Assuming that the influence of atmospheric delay on the phase signal is negligible, the interferograms computed from each SAR image pair contain signal contributions from the Earth's curvature, topography, and surface displacement, as well as noise. We simulated the Earth curvature and topographic phase signals using the orbital geometry of each SAR image pair and using a digital elevation model (DEM) generated from ASTER data. These signals were then subtracted from the smoothed interferograms to reduce noise and then isolate the surface displacement phase signal. At the Petermann Glacier, displacement is caused by ice flow and, in floating sections, by ocean tides. We then combine interferogram pairs to form quadruple difference interferograms (Rignot et al., 1998a) which removes the common signal due to constant ice flow which is relatively stable over short periods in comparison to tidal motion. The remaining phase signal, which is manifest as a dense band of interference fringes at the boundary between grounded and floating ice (Figure 3-2), can be attributed to vertical surface displacement caused by ocean tides. We unwrapped the quadruple difference interferogram phase signal across the glacier grounding zone using the branch cut method (Goldstein et al., 1988) to calculate the absolute differential displacement in the satellite line of sight. It was not possible to initiate phase unwrapping in the same location in all instances (Figure 3-1) due to temporal decorrelation of the SAR imagery inland of the glacier grounding zone, which also limited the extent of interferometric data in other locations, necessitating the use of manual bridges to link areas of disconnected phase in some places. Finally we computed differential vertical displacement from the unwrapped phase using the satellite geometry (Figure 3-2).

3.4.3. Picking the Inland Limit of Tidal Flexure

We identified the Petermann Glacier grounding line location (Figure 3-2) by manually delineating the inland limit of tidal flexure, as described by Rignot et al., (2014). In longitudinal profiles (Figure 3-2) grounded ice shows no significant vertical displacement, in contrast to the floating ice shelf, which shows a relative displacement of up to 149 cm at times of extreme tidal difference. Across the 17 quadruple difference interferograms, the grounding zone is marked as a ramp of between 7 and 47 interference fringe cycles, and there is a strong ($R^2 = 0.94$) positive correlation between the fringe density and magnitude of the vertical displacement measured.

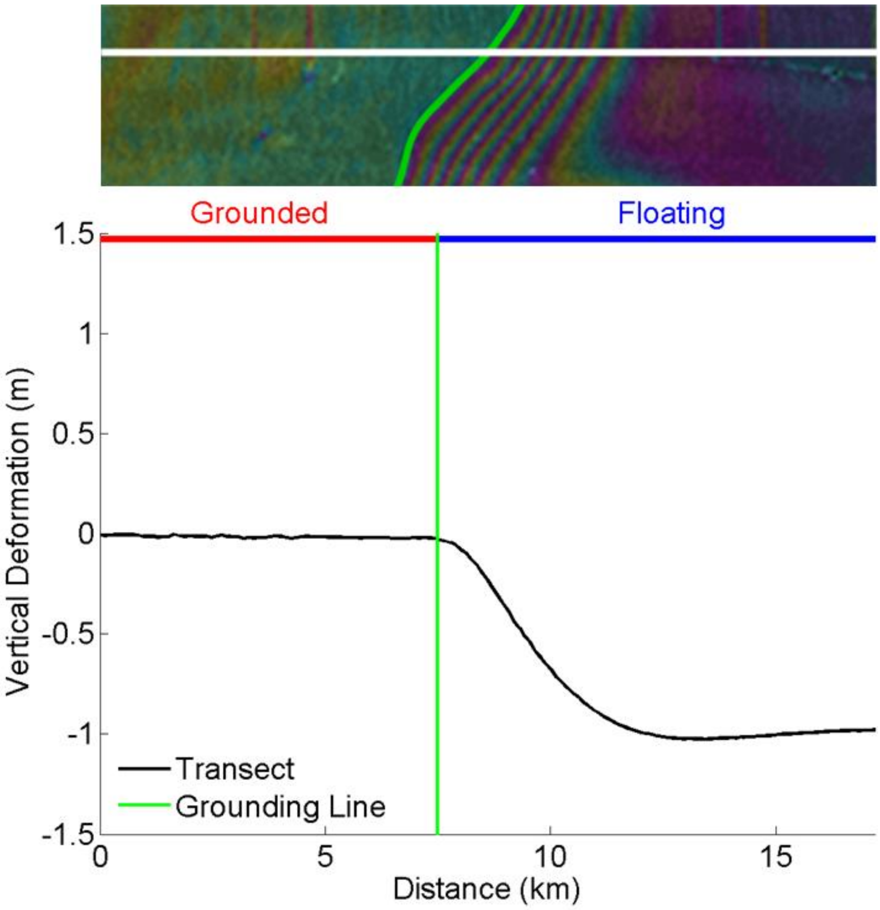

Figure 3-2 *Quadruple difference interferometric fringe pattern across the grounding zone of Petermann Glacier. The grounding line location (green) is identified as the inland limit of tidal flexure as seen in a profile of differential vertical displacement (black) extracted along a transect (white).*

3.4.4. Tide Model Intercomparison

To assess the accuracy of the vertical displacement measured in the differential interferograms, we compared the magnitude of the signal with differential tides calculated from the AODTM-5 Arctic tide model (Padman and Erofeeva, 2004). For this comparison, we assume that vertical displacement is solely caused by ocean tides, and is therefore directly comparable. The landward extent of the AODTM-5 tide model domain ends 71 km from the Petermann Glacier grounding line (Figure 3-3) which, for the majority of our survey period, is seaward of the ice shelf calving front. Consequently, it is not possible to obtain tidal predictions at locations present in the interferometric data. To assess the impact of this mismatch, we examined the spatial variability of modelled tides at the time of each SAR image acquisition in the Petermann Glacier fjord and the open ocean, from the Hall Basin towards the Kennedy (South) and Robeson (North) Channels in the Nares Strait (Figure 3-3). Within the fjord, the AODTM-5 model predicts tides in the range -0.6 to +1.1 m, with a variability of less than 1 cm along each transect. In the open ocean, the predicted tidal range to the North of the Nares Strait is slightly smaller, at just under 1.7 m, whereas to the South it is considerably larger at over 3.6 m. The dispersion of predicted tides is relatively large in the open ocean, at 10 and 15 cm to the North and South, respectively. North of the fjord, tidal range decreases with distance, whereas to the South it increases. Taking the spatial variation of tides into account, we estimate that tidal amplitudes at the Petermann Glacier ice shelf will be within 1 cm of those at the closest available model grid cell.

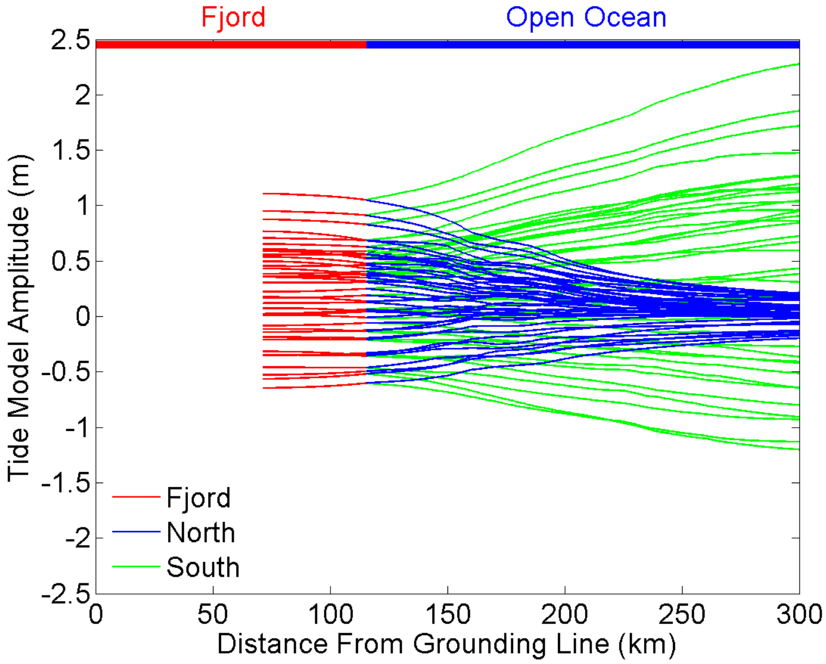

Figure 3-3 *Ocean tide amplitude in the Petermann Glacier fjord (red), and to the North (blue) and South (green) of the fjord in Nares Strait, as predicted by the AODTM-5 Arctic tide model. Each line shows tidal amplitude at the time of the ERS SAR acquisitions used in this study along longitudinal transects in the three different regions (see Figure 3-1). The AODTM-5 tide model domain begins 71 km from the grounding line.*

We compared tidal amplitudes at the AODTM-5 model grid cell closest to the front of the Petermann Glacier; 81.2° N, -62.2° W (Figure 3-1) to vertical displacements recorded in the interferometric data (Table 3-2). Differential tides were computed (Equation 2) as the linear sum and difference of model tides on the dates and times (Table 3-1) of each individual SAR acquisition used to produce each quadruple differential interferogram (Table 3-2). Although modelled tidal amplitudes at the times of the SAR acquisitions span 1.5 m in range, from -0.5 to +1.0 m, the spread of the modelled differential tides is, at 2.2 m (-1.0 to +1.2 m), considerably higher, indicating that the displacement of floating ice recorded in differential interferograms is large relative to the range of absolute tide amplitudes.

$$DMT = \frac{(S1MT - M1MT)}{(S2MT - M2MT)} \tag{2}$$

Table 3-2. *Table showing the modelled ocean tide predicted by the AODTM-5 Arctic tide model for the date and time of each SAR acquisition, the total modelled differential tide calculated from the data using Equation 2. The vertical displacement measured by QDInSAR on the floating ice shelf is also shown for comparison, along with the grounding line location ID.*

GL ID	Master 1 Modelled Tide (*M1MT*) (m)	Slave 1 Modelled Tide (*S1MT*) (m)	Master 2 Modelled Tide (*M2MT*) (m)	Slave 2 Modelled Tide (*S2MT*) (m)	Differential Modelled Tide (D*MT*) (m)	QDInSAR Vertical Displacement (m)
GLL_01	0.59	0.02	0.02	-0.21	-0.34	-0.80
GLL_02	0.02	-0.21	-0.21	0.59	-1.02	-0.86
GLL_03	-0.21	0.59	0.59	1.10	0.29	0.35
GLL_04	0.59	1.10	1.10	0.36	1.25	1.43
GLL_05	1.10	0.36	0.36	-0.14	-0.24	-0.14
GLL_06	0.36	-0.14	-0.14	0.07	-0.72	-0.98
GLL_07	-0.14	0.07	0.07	0.58	-0.30	-0.35
GLL_08	0.07	0.58	0.58	0.87	0.22	0.25
GLL_09	0.58	0.87	0.87	0.56	0.60	0.93
GLL_10	0.56	-0.08	-0.08	-0.11	-0.61	-0.56
GLL_11	-0.08	-0.11	-0.11	0.76	-0.91	-1.24
GLL_12	-0.11	0.76	0.76	0.94	0.69	0.96
GLL_13	0.03	0.38	0.17	0.01	-0.52	-0.67
GLL_14	0.17	0.65	-0.56	0.17	0.24	0.20
GLL_15	0.65	0.35	-0.56	0.17	1.02	1.13
GLL_16	0.53	0.70	0.70	0.02	0.85	0.68
GLL_17	0.35	0.65	0.65	0.17	0.78	0.68

3.5. Results and Discussion

3.5.1. Ice Shelf Relative Displacement

We compared modelled tidal differences to the relative displacement of the Petermann Glacier ice shelf, as recorded in each quadruple difference interferogram, along seven stream-wise transects bisecting the grounding zone (Figure 3-4). On the inland (grounded) ice there is very little vertical displacement, and the mean range of relative heights is 3.7 ± 2.0 cm which is attributed to error in the QDInSAR vertical displacement measurement. In contrast, relative displacement of the floating ice shelf is much larger due to the effects of the ocean tide, and spans a range of 2.8 m over the study period. Overall, there is close agreement between the magnitude of the ice shelf relative displacement and the size of differential tides predicted by the AODTM-5 model, with positive or negative displacements recorded at times of high and low differential tides, respectively. Across the boundary between grounded and freely-floating ice, there is a rapid change in vertical displacement in all 17 interferometric displacement profiles (Figure 3-4 and Figure 3-5). The zone of tidal flexure is on average 4.4 ± 0.8 km wide; however, the relatively large range of 2.8 km is caused by 3 outliers that correspond to low (< 0.5 m) observed tide amplitudes. Although the change in slope is most abrupt at times of high relative displacement, the transition between grounded and floating ice remains distinct in all profiles, allowing the grounding line to be located as the landward break in surface slope across the zone of ice shelf flexure (Rignot et al., 1996). The displacement profiles indicate that there has been no significant change in position of the Petermann Glacier grounding zone and the landward limit of flexure over the 19-year survey period.

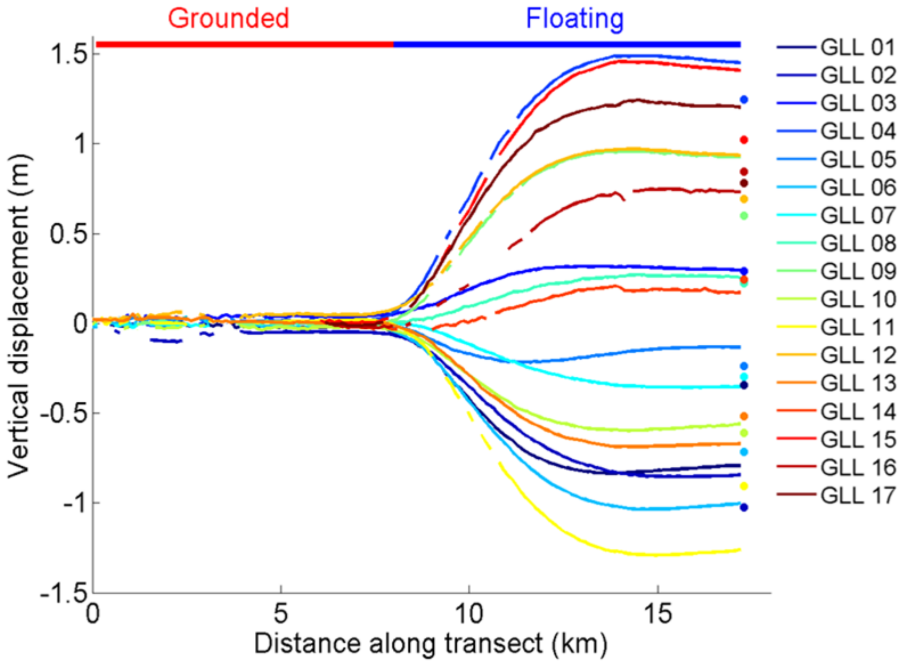

Figure 3-4. *Relative vertical displacement along a flow-line profile of the Petermann Glacier grounding zone measured using 17 quadruple difference interferometry (see Table 3-1). Also shown (coloured dots) are relative tidal amplitudes at the same epoch as determined from the AODTM-5 model Arctic Ocean tide model. Between 0 and 8 km, there is no vertical displacement, indicating that this section of the glacier is grounded on bedrock. However, from 8 km and farther seaward, up*

to 1.5 m of relative displacement are recorded, indicating this section of the glacier is influenced by the ocean tide and therefore floating.

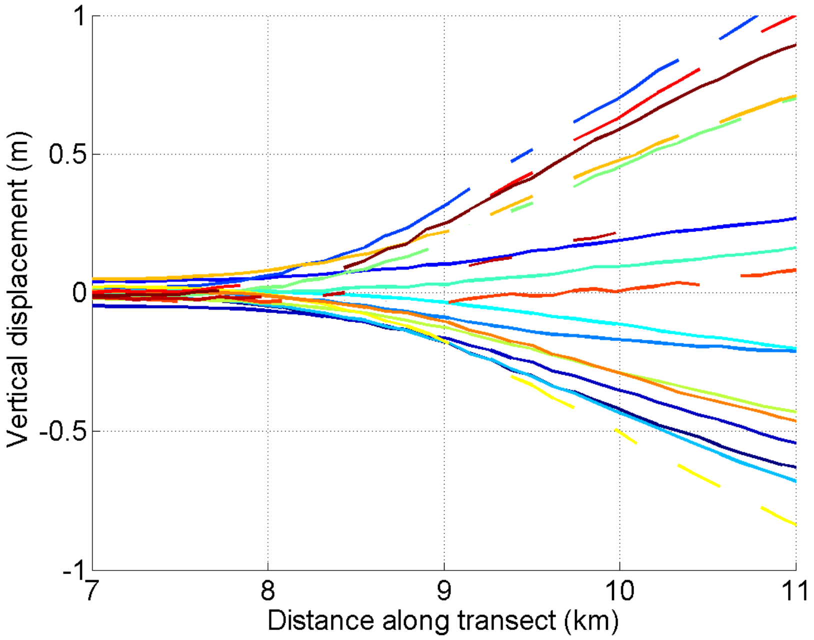

Figure 3-5. *Zoomed in view of the relative vertical displacement along a flow-line profile of the Petermann Glacier grounding zone measured using 17 quadruple difference interferometry (see Table 3-1).*

3.5.2. Tide Model Validation

We compared the modelled differential tide amplitude with the QDInSAR vertical displacement to assess the degree to which the datasets agree. For this comparison, we used estimates of relative vertical displacement determined from the interferometric data in an area of the glacier floating freely and just seaward of the grounding line location (Figure 3-1). There is a strong (R^2= 0.95) positive correlation between the modelled tidal difference and the relative vertical displacement of the floating ice, and the mean difference is only 16.8 ± 20.6 cm (Figure 3-6). We estimate that 0.9 cm of this difference is caused by spatial variability of the tide in the 70 km section of the fjord separating the locations of the tidal prediction and the interferometric data, and that 3.7 cm of the difference is caused by error on the interferometric measurement. The remaining difference could arise through errors in the tidal predictions, or through other factors affecting the vertical displacement of the ice shelf – for example atmospheric pressure variations or non-tidal changes in local sea level height. It is also possible that the Petermann Glacier ice shelf is not freely floating in hydrostatic equilibrium with the ocean; however, the strong correlation between modelled and observed tides indicates that this is the case. The strong relationship and small difference between both datasets indicates that the tide model predicts both the phase and the amplitude of the ocean tide to within 12.2 cm.

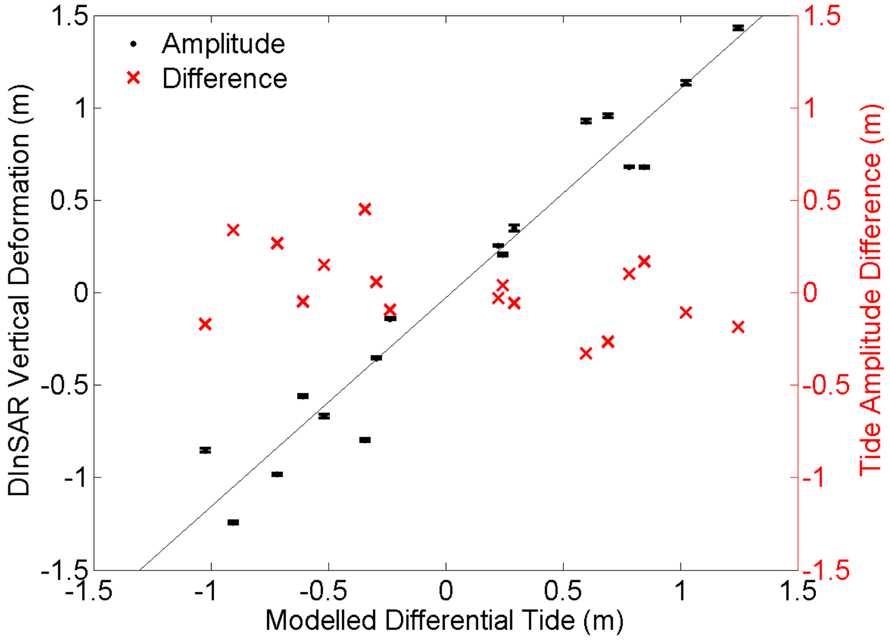

Figure 3-6. *Comparison between ocean tidal amplitude differences, as determined from the AODTM-5 Arctic tide model (Padman and Erofeeva 2004), and relative vertical displacement of the Petermann Glacier ice shelf, as determined from quadruple difference interferometry (black points). Error on the QDInSAR vertical displacement measurement is quantified as the maximum range of vertical motion measured on the stable grounded portion of the ice stream. Also shown is the difference (anomaly) between the two measurements (red crosses).*

Accurate estimates of ocean tides are required for many glaciological applications, including analysis of ice shelf thickness changes using satellite altimetry (Shepherd et al., 2003), assessments of ice sheet mass change using satellite gravimetry (Velicogna and Wahr, 2013), and for characterising patterns of ice shelf basal melting derived from satellite radar interferometry (Joughin and Padman, 2003). Direct observations of ocean tides are, however, sparse, and the certainty of ocean tidal predictions is limited by the paucity of bathymetric data (Padman et al., 2002). These problems are especially pronounced at the ice sheet margins which are relatively inaccessible, and which often exhibit rugged and steep bathymetric slopes. Satellite observations have been used to evaluate ocean tide model predictions in such remote and inaccessible regions. For example, in the Weddell and Amundsen Seas, modelled ocean tidal differences have been shown to deviate from observations of ice shelf relative displacement by 9 cm, on average (Fricker and Padman, 2002; McMillan et al., 2011). Because there are few floating ice shelves in the Northern hemisphere, an assessment of the utility of ocean tide models for glaciological applications in this region has been lacking. Our assessment that tides predicted by the AODTM-5 model differ from the observed displacement of the Petermann Glacier floating ice shelf by 16.8 cm, on average, confirms, therefore, that ocean tide models perform comparably well for glaciological applications in the Northern hemisphere as they do in the Southern hemisphere.

3.5.3. Grounding Line Migration

Although there has been clear movement of the Petermann Glacier grounding line since 1991, a progressive retreat or advance has not occurred, and its relative shape has remained broadly constant over the 19 year survey period, with prominent meanders present in each set of interferometric data (Figure 3-7). The most distinctive features are the inland-pointing notches on the North-Eastern and South-Western margins of the ice stream, which is in line with observations showing that the ice is thicker towards the centre of the glacier (Joughin et al., 1999) as is the case in other fast flowing ice streams. The furthest inland grounding line locations we have recorded occurred in February 1992 (GLL_04) and in May 2011 (GLL_15). Relative to these positions, grounding lines recorded at other times are located up to several kilometres downstream, and there is no obvious progression through time.

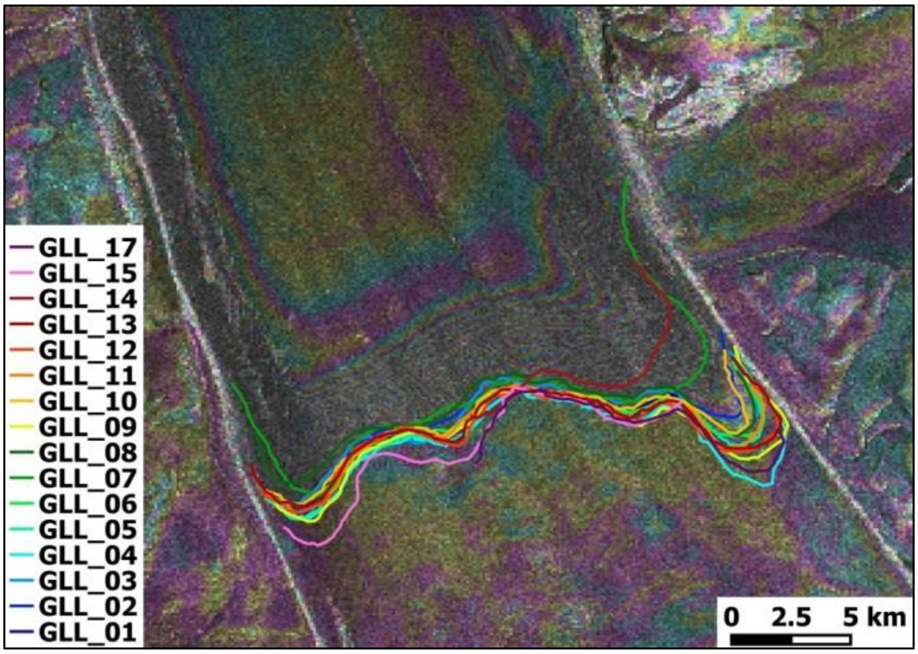

Figure 3-7. *Petermann Glacier grounding line measured between 1992 and 2011. Each coloured line represents a grounding line produced from quadruple difference interferometry at distinct time periods (see Table 3-1).*

To characterise the temporal variability of the Petermann Glacier grounding line location, we measured the relative grounding line position along 7 transects perpendicular to the grounding zone in all 17 quadruple differential interferograms (Figure 3-8). Over the 19 year study period, the mean absolute variability of the grounding line position was 0.5 ± 0.03 km. The maximum range of grounding line locations was 7.0 km, with the most inland and seaward positions measured at -2.1 km and +4.9 km from the midpoint, respectively. Both extremes occurred at the northern edge of the glacier, along transect 7, which bisects the broadest section of the grounding zone. Elsewhere, the range (2.8 km) and variability (0.3 ± 0.4 km) of grounding line positions are considerably lower. This demonstrates that, while the mean grounding line variability is relatively low, this does not preclude large, isolated, movements, and so sparse temporal records should be analysed with care (Figure 3-8).

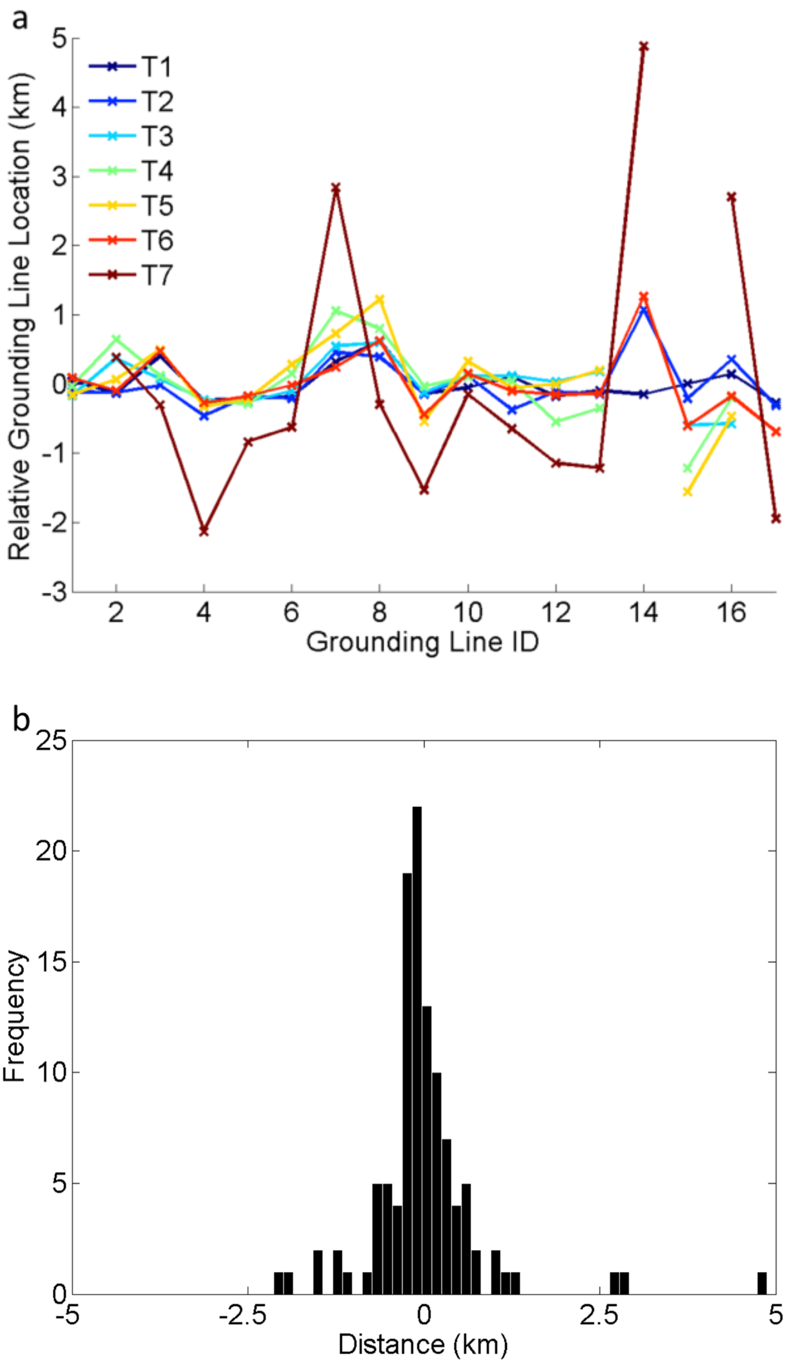

Figure 3-8. *(a) Distance of grounding line relative to the start of 7 stream-wise transects straddling the Petermann Glacier grounding zone (see* Figure 3-1*) between February 1992 (GL1) and June 2011 (GL17). (b) Histogram of relative grounding line positions.*

If the observed variability in grounding line position is attributed to a progressive change over time, the average grounding line retreat would be 0.8 km, equivalent to an average retreat rate of 43 m/yr – in line with estimated rates of 120 m/yr grounding line retreat over the Holocene inferred from the geological record (Conway et al., 1999), but two orders of magnitude lower than those recorded in regions of contemporary imbalance (Park et al., 2013). However, there is no significant correlation between grounding line location and time (Figure 3-9), which suggests that the Petermann Glacier has remained relatively stable over the past 19-years, despite the occurrence of large calving events (Nick et al., 2012) during the same period. Although the presence of a modest secular trend in grounding line position cannot be ruled out, the absence of a direct correlation suggests that time is not the dominant controlling factor and therefore the observed variability may be due to factors other than ice dynamical imbalance.

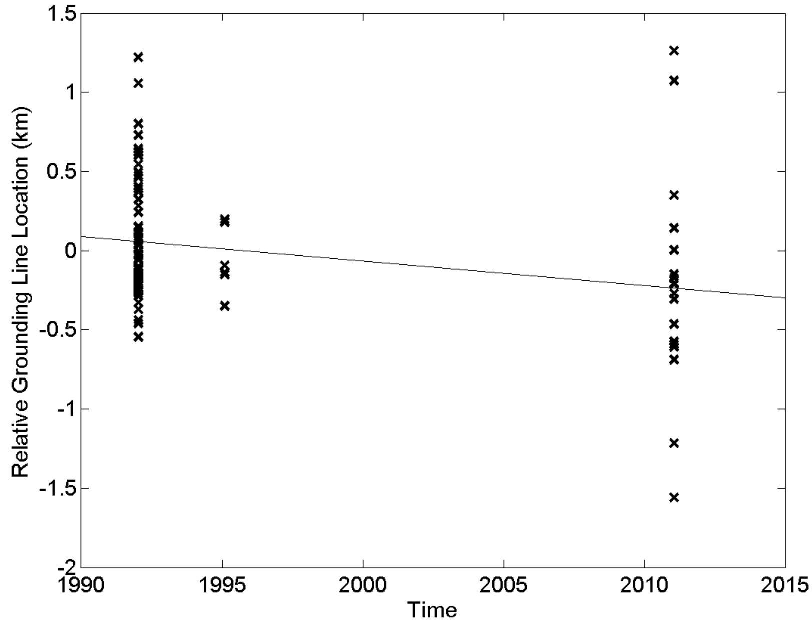

Figure 3-9. *Change in grounding line position over time between February 1992 (GL1) and June 2011 (GL17).*

3.6. Drivers of Grounding Line Migration

The position of an ice sheet grounding line is influenced by many factors, including the bedrock geometry, basal friction, ice shelf buttressing, ice thickness, ice velocity and ocean tides (Thomas, 1984). Although progressive grounding line retreat has been observed over annual to decadal timescales as a consequence of ice thinning following ice shelf collapse (Rack and Rott, 2004) and sustained ocean-driven melting (Park et al., 2013), the location also changes over shorter (sub-daily) timescales due to other factors – notably the vertical displacement caused by ocean tides (Figure 3-10). While ground based observations show that the inland limit of tidal flexure at the glacier surface does not necessarily fall directly above the grounding line (Smith, 1991), in elastic-beam theory the point of minimum deflection does, and changes in hinge line position are often taken as a proxy for changes in grounding line location (Rignot, 1996). The magnitude of tidally-induced grounding line displacement depends primarily on the bedrock slope and on the tidal range, and previous studies have shown that ocean tides can cause over 130 m change in grounding line position at the Filchner Ronne ice shelf (Smith, 1991). Other factors, such as localised, temporary ice thickness changes advected downstream, may also lead to short-term changes in grounding line position (Figure 3-10).

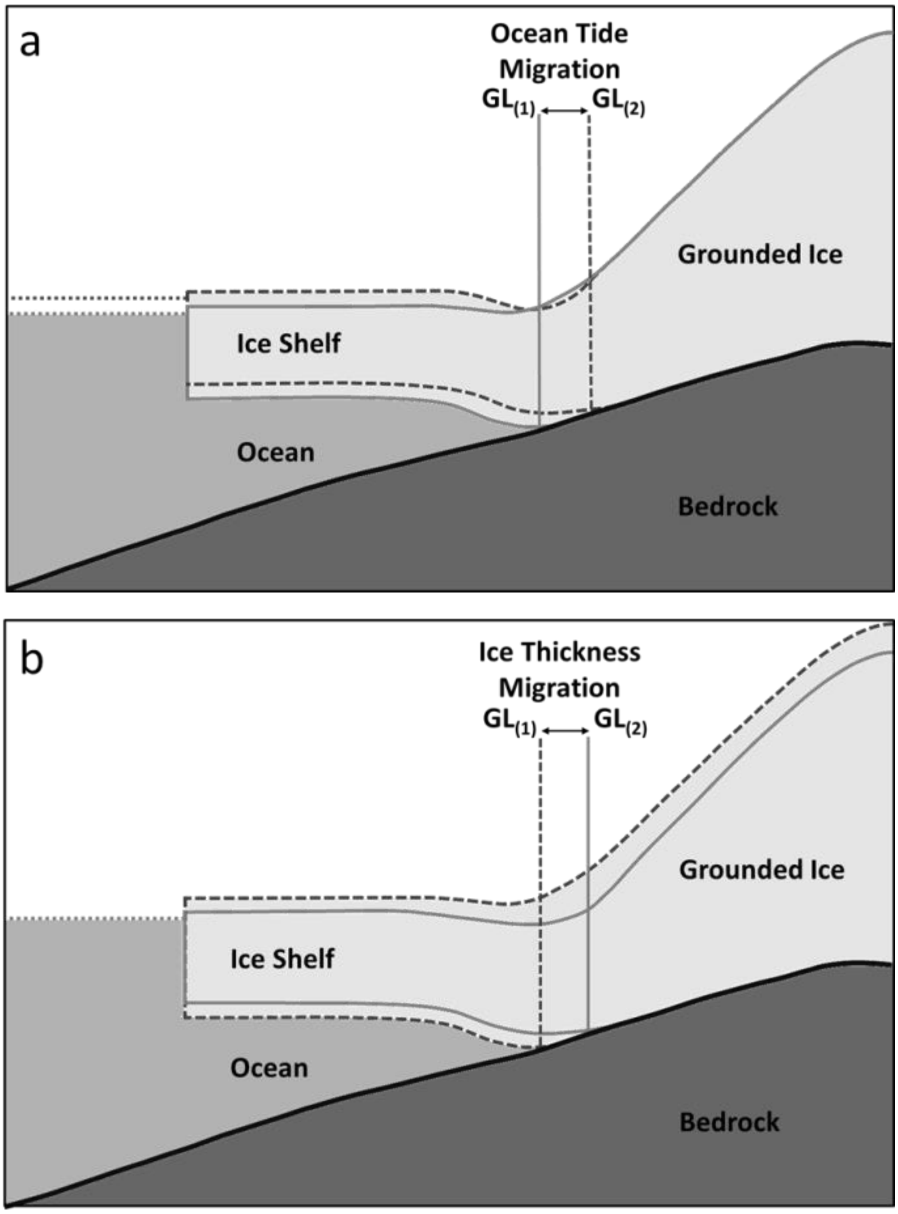

Figure 3-10. *Illustration of grounding line migration caused by (a) change in ocean tide amplitude and (b) change in ice thickness.*

Given that such a strong relationship exists between ice shelf vertical displacement and ocean tides at Petermann Glacier (Figure 3-6), we conclude that the floating section is in hydrostatic equilibrium with the surrounding ocean, meaning that the grounding line position ought to be sensitive to short term changes in sea surface height. Moreover, because the Petermann Glacier grounding line has moved forwards and backwards on many occasions over our survey period, it seems likely that a short-term forcing is responsible for the observed migration. To examine this possibility, we use a simple geometrical relationship to simulate the effects of short-term fluctuations in ocean tide and glacier ice thickness on the position of the grounding line (Rignot, 1998b). In this formulation (Equation 3), grounding line positions ($\dot{x}$) migrate back and forth with time by following changes in ocean tide ($\dot{z}$) and ice thickness ($\dot{h}$).

$$\dot{x} = \left(\frac{\rho_w}{\rho_i}\right)\left(\frac{1}{[\alpha - \beta(1-\rho_w/\rho_i)]}\right)\dot{z} - \frac{\dot{h}}{[\alpha - \beta(1-\rho_w/\rho_i)]} \qquad (3)$$

where $\dot{h} > 0$ for thickening, $\dot{x} > 0$ for hinge-line retreat, alpha and beta are the surface and basal slopes, respectively, counted positive upward, and ρ_w and ρ_i are the densities of sea water (1027.5 kg m^{-3}) and ice (900 kg m^{-3}), respectively. Using this relationship, changes in grounding line position associated with changes in tide and thickness can be simulated, independently.

To estimate the surface and bedrock slopes and the potential scale of short-term fluctuations in glacier thickness, we used geometry data acquired along two stream-wise profiles on Petermann Glacier in 2010 by the NASA Operation Ice Bridge Airborne Topographic Mapper (ATM) lidar and Multichannel Coherent Radar Depth Sounder (MCoRDS) (Allen, 2013). Although the ice surface elevation is similar in both flight lines, there are large differences in the elevation of the ice base (Figure 3-11). Along the western flight-line, there is an abrupt 420 m change in the elevation of the glacier base over a 2.6 km distance, in sharp contrast to the eastern flight-line where the step is only 75 m over a similar distance (Figure 3-11 a and c). The MCoRDS instrument detects the ice-bedrock interface on the grounded portion of the ice stream and the ice–ocean interface on the ice shelf, therefore the ice base only represents the bedrock topography inland of the grounding line. We calculated ice surface and bedrock slopes along a 4.4 km section (the mean width of the flexure zone) of each flight-line centred on the most inland grounding line position measured from the interferometric data (Figure 3-11). The estimated ice surface and bedrock slopes from the western flight-line are 0.83% and -0.11%, respectively, and from the eastern flight-line they are 0.94% and 0.42%, respectively.

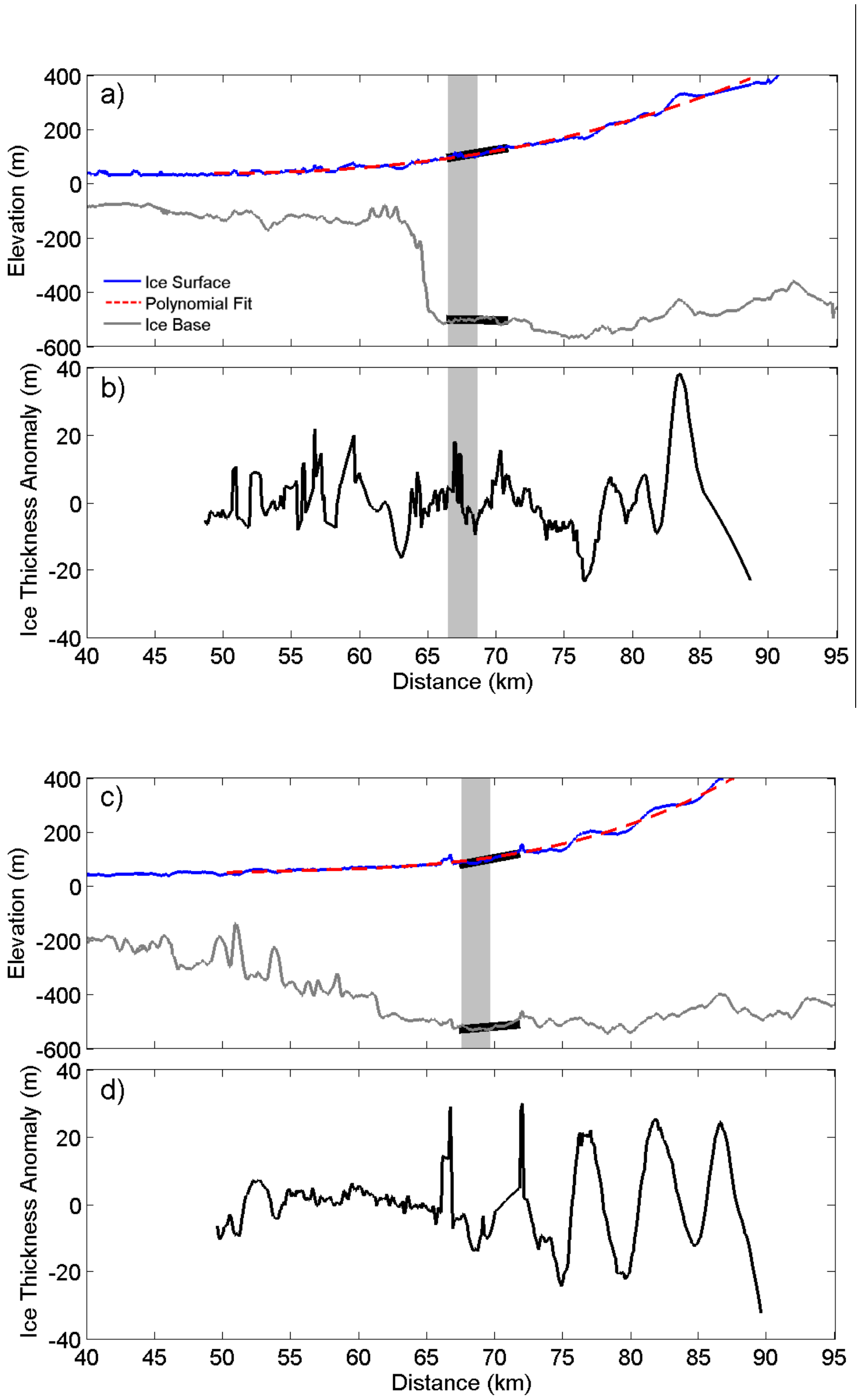

Figure 3-11. *Ice surface (blue line) and ice bottom (grey line) elevation measured along adjacent*

western (a) and eastern (c) stream-wise profiles of the Petermann Glacier (see Figure 3-1 *for locations). The spread of grounding line positions measured in this study are highlighted (grey shaded area). Regions over which the surface and bedrock slopes are computed (see text) are highlighted by a thick black line (a, c). Also shown (red dashed line) is a polynomial fit to the ice surface elevation from which ice thickness anomalies (black line in b, d) in the vicinity of the grounding zone are calculated.*

We estimate that ocean tides cause between 114 and 141 m grounding line movement at Petermann Glacier for every metre of tidal displacement, and that fluctuations in ice thickness cause between 100 and 123 m of grounding line movement for every metre change. The spread of values reflects differences in the ice surface and bedrock slopes determined along the two flight-lines. For comparison, the rate at which the Petermann Glacier grounding line migrates through changes in tidal displacement or ice thickness is approximately three times smaller than at the Pine Island Glacier in West Antarctica (Rignot et al., 1998b), where the bedrock slope, in particular, is more pronounced.

We simulated the degree of grounding line migration caused by ocean tides by scaling estimates of the differential tide ($\dot{z}$) derived from the AODTM-5 Arctic tide model (Table 3-2) by each of the tidal migration factors. The mean simulated tidally-induced grounding line motion was 88 and 71 m along the western and eastern flight-lines, respectively, and the maximum was 319 and 259 m, respectively, at the time of the minimum (-1.02 meters) and maximum (1.25 meters) modelled differential tides (Figure 3-12). By comparison, the mean actual grounding line variability measured along transects T1 and T2 adjacent to each flight-line was 193 and 281 m, respectively, indicating that, on average, the tides account for around one third of the recorded movement. Based on the maximum expected differential tide range (4.4 m), we estimate that the Petermann Glacier experiences up to 560 m of tidally-induced grounding line motion. This degree of motion is too small to account for the range of grounding line variability we have recorded (Figure 3-8). Moreover, when applied as a correction, the simulated tidal motion does not reduce the variance in the observed grounding line position (Figure 3-12), suggesting that ocean tides are not the dominant cause of grounding line variability on Petermann Glacier.

Fluctuations in glacier thickness also drive changes in grounding line position. First, we computed the ice thickness change required to account for the observed grounding line variability using the scaling factors determined along the two flight-lines, to assess the likelihood that this may have occurred. The ice thickness anomaly required to account for the observed mean variability in grounding line position is 2.2 ± 2.9 m, with a maximum variability of 5.0 m and 10.7 m along the western and eastern flight-lines, respectively. Although there is some evidence for modest long term change in dynamic ice thickness (0.15 m/yr) on Petermann Glacier (Pritchard et al., 2009), there are significantly larger (± 25 m) stream-wise fluctuations in the thickness of the floating section (Figure 3-11), which could potentially influence the location of the grounding line as they are advected downstream. We computed the ice thickness anomaly by differencing the mean polynomial fit from the ice surface elevation profiles within a 40 km region centred on the 2011 grounding line (Figure 3-11). The average variability was 7.1 to 8.1 m along the western and eastern flight-lines, respectively, with peak changes in the range 23.5 to 38.0 m. Were all of the observed localised ice thickness anomaly to cause change in grounding line position, it would be equivalent to a mean 0.9 ± 1.2 km of motion, with a maximum range of 7.9 km (Figure 3-12). While localised ice thickness change many not fully translate into change in grounding line position due to the effect of lateral support from surrounding ice, the motion attributed to the range of ice thickness anomalies is 94% greater than the observed mean grounding line variability and is therefore sufficiently large to account for all the observed motion.

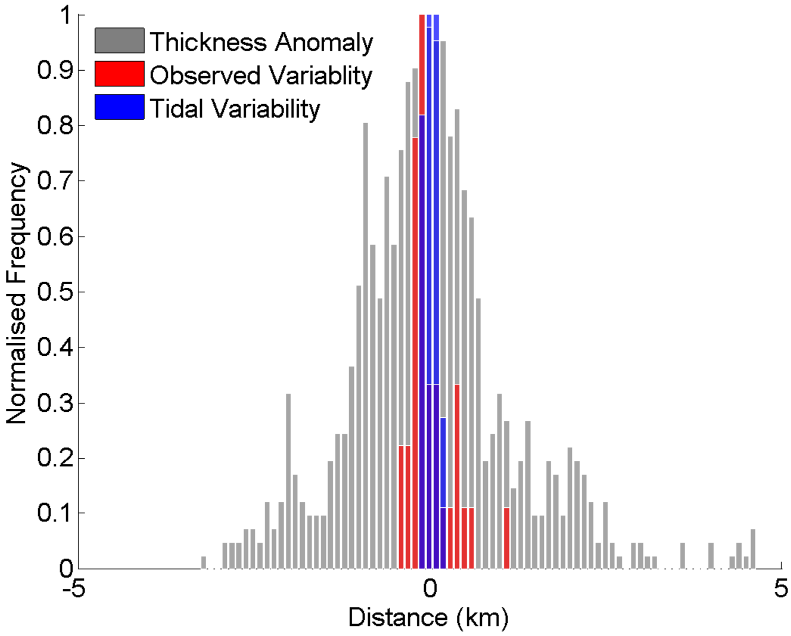

Figure 3-12. *Normalised distribution of observed (red) changes in Peterman Glacier grounding line position and of the simulated change due to fluctuations in ocean tide (blue) and thickness anomaly (grey).*

3.7. Conclusions

We have used estimates of Petermann Glacier ice shelf tidal motion derived from synthetic aperture radar interferometry over the period 1992 to 2011 to assess the ability of the AODTM-5 Arctic ocean tide model to simulate differential tides. The root mean square difference between the observed and modelled differential tides is 20.6 cm, approximately 5 % of the tidal range in the Nares Strait, indicating that AODTM-5 provides reliable predictions in this region. From the same data, we have also determined the location of the Petermann Glacier grounding line on 17 different occasions using quadruple-difference interferometry – the most comprehensive record for an ice stream to date. During this period, the grounding line advanced and retreated on numerous occasions and, while the average movement was just 0.5 km over the 19-year period, the range of positions spanned a 7.0 km distance. We conclude, therefore, that the Petermann Glacier is dynamically stable, consistent with observations of only modest changes in the thickness of the grounded ice inland (Pritchard et al., 2009), though in contrast to several ice streams on the south-western coast of Greenland (Moon et al., 2012; Joughin et al., 2014a). Using a simple geometrical relationship, we estimate that one third of the observed variation in grounding line position can be attributed to the influence of ocean tides. On the other hand, all of the observed migration could arise through modest (< 11 m) fluctuations in the glacier thickness - one third of the variability that is typical of ice in the vicinity of the glaciers grounding zone.

Although the technique of quadruple-difference synthetic aperture radar interferometry provides a precise estimate of ice shelf tidal motion (to within 3.7 cm, on average) and of grounding line position (to within 810 m, on average), our analysis suggests that short-term fluctuations in grounding line position can be large in comparison. The impact of such changes should be taken into account when assessing grounding line migration over time; for example, had our survey consisted of measurements acquired in 1992 and 2011 only, the change in grounding line position could have been misinterpreted as a 2.3 km retreat across the main trunk (T4) – 4.8 times larger than the mean variability (0.5 km) based on the complete dataset. Moreover, at Petermann Glacier the degree of grounding line motion associated with ocean tides and changes in ice thickness is relatively small when compared to other locations (Padman et al., 2002; McMillan et al., 2014), and so the impact of short term variations could be even larger elsewhere. To overcome this problem, grounding line positions should be monitored on several occasions when attempting to quantify rates of migration over time.

Chapter 4

Differential Range Direction Offset Tracking (DRDOT): A Technique For Measuring the Ice Sheet Grounding Line in Incoherent Synthetic Aperture Radar Data

4.1 Abstract

Grounding lines are an important glaciological parameter, because they mark the lateral extent of ice sheets and because their migration is a key indicator of dynamic instability. However, a paucity of suitable data has limited the spatial and temporal extent with which they have been measured. We present a technique for mapping ice sheet grounding lines using differential range direction offset tracking (DRDOT) in incoherent synthetic aperture radar data. We apply the technique to determine the grounding line position on Petermann Glacier using a sequence of 11 TerraSAR-X SAR images acquired between 23rd June and 22nd October, 2009. We find that the DRDOT technique is successful when predicted differential ocean tide amplitudes are greater than 0.5 m, allowing us to detect the grounding line on 4 separate occasions with a lateral precision of 0.8 km. Petermann Glacier also exhibited a seasonal increase in the rate of ice flow of up to 20.5% over the survey period, which was accounted for when tracking differential range offsets. An intercomparison of the DRDOT and quadruple difference interferometry (QDInSAR) techniques shows good agreement with the location and relative shape of the grounding line reproduced across the ice stream. The mean position of the DRDOT grounding line varied by 0.8 km which was 44 % greater than the mean variability observed by QDInSAR. The DRDOT technique can be applied to historical and future incoherent synthetic aperture radar data to complement measurements determined from QDInSAR which, though more accurate, are spatially and temporally sparse.

4.2 Introduction

The grounding line marks the boundary between bedrock, the floating ice shelf and the grounded ice sheet (Figure 4-1). The position can fluctuate on short, sub-daily timescales due to the effects of ocean tides and localised ice thickness change (Chapter 3), and over long, annual to decadal timescales when sustained ice thickness change occurs (Rignot et al., 1998b; Park et al., 2013). The grounding line is of critical importance as it constrains the lateral extent of the ice sheet margin and is used for determining the optimal location of flux gate boundaries used in mass budget calculations. It is a sensitive indicator of ice sheet stability and when change in grounding line position is observed it provides important information on the location and extent of dynamic imbalance (Rignot et al., 1998b; Park et al., 2013; Rignot et al., 2014) and can indicate the existence of ocean forcing mechanisms (Dutriux et al., 2014). Measuring the present day change in grounding line allows us to better understand the contemporary ice sheet contribution to sea level rise, and to evaluate the skill with which ice sheet models are able to simulate dynamical imbalance (Favier et al., 2014).

The grounding line is located at the base of the ice sheet therefore it cannot be directly measured by satellite Earth observation techniques. However, the ice sheet hinge line - defined as the inland limit of tidal flexure at the ice surface - can be observed from above (Figure 4-1). Although there may be small lateral variations in the location of the hinge line and grounding line, their migration rates are similar, and it is assumed that measuring either parameter is an accurate measure of grounding line motion or stasis (Rignot et al., 1998b).

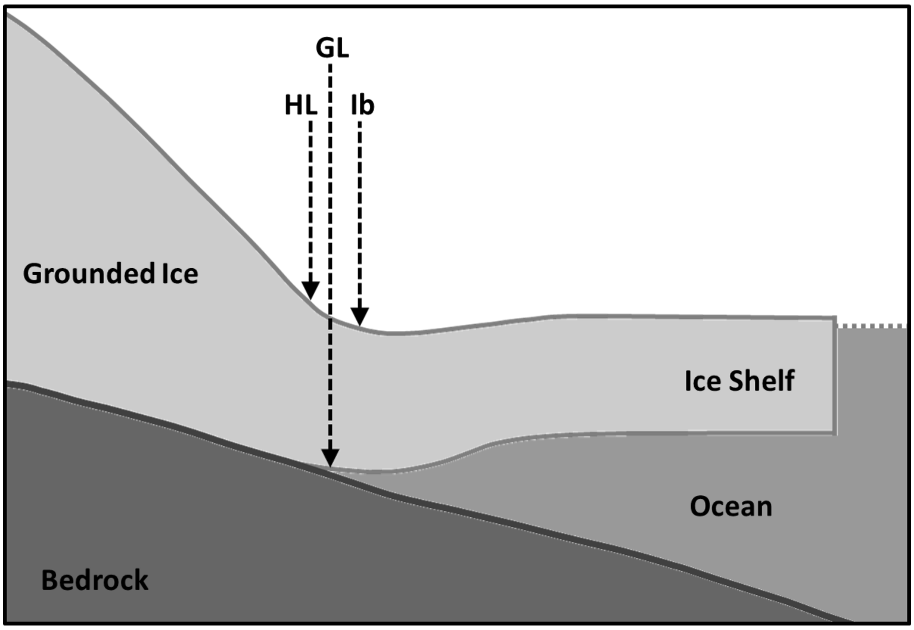

Figure 4-1. *Illustration showing the location of the ice sheet grounding line (GL), hinge line (HL), break in surface slope (Ib) (adapted from Bindschadler et al., 2011).*

Three independent Earth observation techniques have been used to measure the ice sheet grounding line position; shadow in optical satellite imagery (Bindschadler et al., 2011), and vertical displacement in both repeat track laser altimetry (Fricker and Padman, 2006) and quadruple difference interferometric synthetic aperture radar (QDInSAR) (Goldstein et al., 1993). An abrupt change in ice surface topography occurs at the boundary between the steeply sloping grounded ice sheet and the flat ice shelf (Figure 4-1), and this is visible as a band of topographic shadow in radiometrically calibrated optical satellite data (Bindschadler et al., 2011). The shadow boundary is used as a proxy for the grounding line, because in regions of high basal drag the basal and driving stress balance, which in turn controls the location of the break in ice surface slope (Payne et al., 2004; Schoof et al., 2007). However, in regions of low basal drag, such as ice plains (Brunt et al., 2011), a break in surface slope is not always present, limiting the extent to which this technique can be applied.

As an alternative approach, the hinge line can be detected as the limit of floating ice displacement by ocean tides. Using altimetry, this technique has only been successfully applied to data acquired by the Ice, Cloud, and land Elevation Satellite (ICESat) which was limited by its short (6-year) mission lifetime between 2003 and 2009 (Fricker and Padman, 2006). QDInSAR, which measures tidal displacement of the floating ice shelf with centimetre-scale vertical accuracy and metre-scale spatial resolution (Rignot, 1998a), is to date the only technique which has been successfully used to monitor change in grounding line position over time (Park et al., 2013; Rignot et al., 2014). However, the spatial coverage and temporal density of synthetic aperture radar (SAR) image triplets with a sufficiently short temporal baseline (days) to maintain phase coherence on fast flowing ice streams is sparse. This paucity of coherent SAR data has limited the extent to which changes in grounding line position have been measured by QDInSAR, and even in the most frequently observed areas such as Pine Island Glacier in West Antarctica, grounding lines have only been measured 5 times over the last 25 years (Park et al., 2013; Rignot et al., 2014). Consequently, new techniques are required to fully exploit the satellite data archives to improve the temporal and spatial coverage of grounding line measurements.

4.3 Study Area

Located on the North West coast of Greenland (81°N, 62°W), Petermann Glacier is one of only 7 marine terminating ice streams on the Greenland ice sheet (Moon et al., 2012). It has a large, 70 km long and 20 km wide ice tongue which is freely floating in hydrostatic equilibrium with the ocean (Chapter 3) (Figure 4-2). Over the past 25 years, surface lowering (Pritchard et al., 2009, Helm et al., 2014) and ice speedup (Moon et al., 2012) have been observed on many fast flowing ice streams in South East and West Greenland. However, the Petermann Glacier has remained relatively stable, with no significant long-term ice speedup or thinning, despite the occurrence of large, episodic iceberg calving events in 1992, 2010 and 2012 (Nick et al., 2012; Munchow et al., 2014) or a progressive ice front advance between 1992 and 2009 (Figure 4-2). Although large, the Petermann Glacier calving events are therefore symptomatic of its natural cycle (Falkner et al., 2011). A numerical model simulation (Nick et al., 2013) has shown that the glaciers low sensitivity to change in terminus position is partly because its relatively thin floating ice tongue is subject to very low lateral drag, and therefore does not provide substantial resistive force. Instead, the dominant mechanism for its ice loss is basal melting by warm ocean water concentrated at the grounding line (Rignot and Steffen, 2008), indicating that any future dynamical change will likely be triggered by changes in ocean conditions. However, an assessment of the Petermann Glacier grounding line position between 1992 and 2011 using QDInSAR shows that it has remained stable for the past two decades (Chapter 3), confirming the absence of dynamic instability prior to 2011.

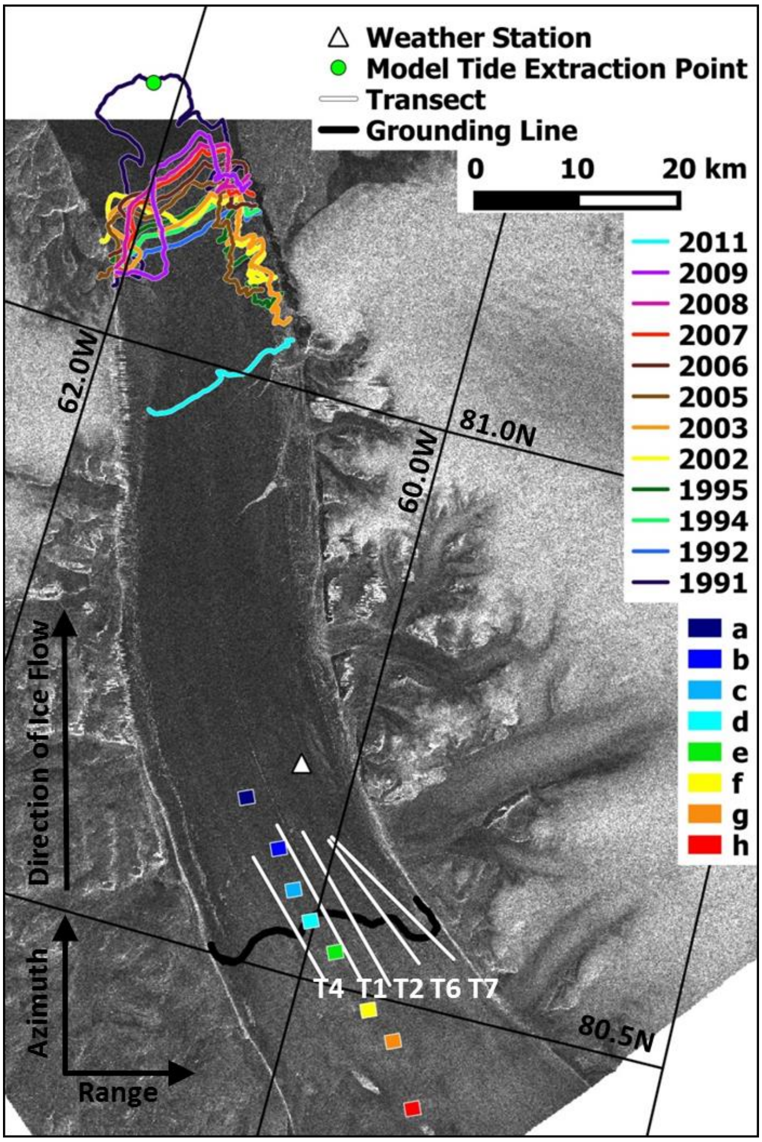

Figure 4-2. *Map of Petermann Glacier in North West Greenland shown by an ERS-1 synthetic aperture radar (SAR) backscatter intensity image. Also shown is a time series of ice stream calving front locations (coloured lines), the tide model extraction point (green dot), a weather station (white triangle), the location of transects (white lines), polygons where ice speed was measured (a (blue) to h (red)), and the 1995 grounding line determined from quadruple difference interferometry (QDInSAR) (thick black line) (*Chapter 3*). The direction of ice flow, and the TerraSAR-X range and azimuth look directions are also annotated.*

4.4 Data

4.4.1. Synthetic Aperture Radar Data

We used a time series of 11 TerraSAR-X single-look slant-range complex (SSC) Synthetic Aperture Radar (SAR) images of Petermann Glacier, acquired between the 23rd June 2009 and the 22nd October 2009 (Table 4-1). The 30 km wide by 50 km long images were acquired in strip map mode HH polarization at a 41 degree incidence angle, on an ascending track with a relative orbit number of 42. Each image was acquired at the TerraSAR-X nominal 11-day repeat period, apart from one date (17th August 2009) when an image was not acquired. A total of 9 image pairs were formed from the time series of SAR data. TerraSAR-X is an X-band SAR satellite operating at a central frequency of 9.65 GHz, with a 3.1 cm radar wavelength, just over half that of C-band (5.6 cm) SAR sensors such as ERS-1/2, ENVISAT and Sentinel-1. Phase coherence is more rapidly lost at high frequencies such as X-band, which further reduces the number of interferometrically viable image pairs in comparison to C-band SAR. Preserving phase coherence on ice covered terrain is particularly challenging because change in surface characteristics can occur within days due to meteorological effects such as snow melt, snowfall and blowing snow, and rapid surface displacement caused by the flow of ice. Coherence images produced from the cross correlation coefficient of each SAR pair confirmed that phase coherence is maintained at X-band over 11 days on stationary mountainous areas; however, all 9 TerraSAR-X image pairs are incoherent on the main trunk of the Petermann Glacier ice stream which flows at speeds greater than 1 km per year. Because phase coherence is not preserved within the TerraSAR-X time series, the QDInSAR technique for detecting grounding line locations cannot be used on these data. Instead, we develop a new technique for measuring the grounding line using the real-valued intensity information rather than the phase component of the SAR image.

Table 4-1. *Specification of all TerraSAR-X SAR data used in this study including; grounding line pair ID, master and slave image acquisition dates and day of the calendar year, tide amplitude extracted from the AOTIM-5 Arctic Tide model at the master and slave image acquisition time, and the modelled differential tide amplitude (Padman and Erofeeva, 2004).*

Grounding Line Pair ID	Master Date	Slave Date	Master Day of the Year	Slave Day of the Year	Master Model Tide Amplitude (m)	Slave Model Tide Amplitude (m)	Modelled Differential Tide (m)
GL_01	20090623	20090704	174	185	-0.17	-0.56	0.38
GL_02	20090704	20090715	185	196	-0.56	0.21	-0.76
GL_03	20090715	20090726	196	207	0.21	0.54	-0.33
GL_04	20090726	20090806	207	218	0.54	-0.25	0.79
GL_05	20090828	20090908	240	251	0.26	0.51	-0.25
GL_06	20090908	20090919	251	262	0.51	-0.31	0.82
GL_07	20090919	20090930	262	273	-0.31	-0.49	0.18
GL_08	20090930	20091011	273	284	-0.49	0.34	-0.83
GL_09	20091011	20091022	284	295	0.34	0.47	-0.12

4.4.1. Ocean Tide Model

We estimated the ice shelf vertical displacement present in all 9 TerraSAR-X image pairs using predictions of tidal amplitude from the AODTM-5 Arctic tide model (Padman and Erofeeva, 2004) during the study period. This provides an independent assessment of the predicted tidal displacement present in each SAR image pair as it is unlikely that the ice stream flexure zone will be resolved at very low tide amplitudes. The AODTM-5 model estimates ocean tide phase and amplitude from 8 tide constituents including the semi-diurnal principal lunar (M2), principal solar (S2), larger lunar elliptic (N2), lunisolar (K2) constituents, and the diurnal principal lunar (O1), principal solar (P1), lunisolar (K1) and elliptical lunar (Q1) constituents. The total tide amplitude was retrieved every hour throughout the 4 month study period (Figure 4-3) and at the time of each SAR image acquisition (Table 4-1), from a point located at the inland limit of the tide model domain in the Petermann Glacier fjord, 71.4 km away from the grounding line (Figure 4-2). Although the tidal range during the 4 month study period was 2.1 m, the TerraSAR-X images sampled only half (1.1 m) of the spread, with an mean absolute amplitude of 0.37 m. Differential tidal amplitudes were calculated as the difference between the tide predictions at the times of master and slave SAR image acquisitions, respectively (Table 4-1). At 1.7 m, the range of differential tides is 35 % greater than the range sampled by the individual SAR images, with a mean absolute differential tide of 0.50 m. Of the 9 TerraSAR-X image pairs, 5 have small differential tides (<0.5 m) and 4 have large differential tides (>0.5 m).

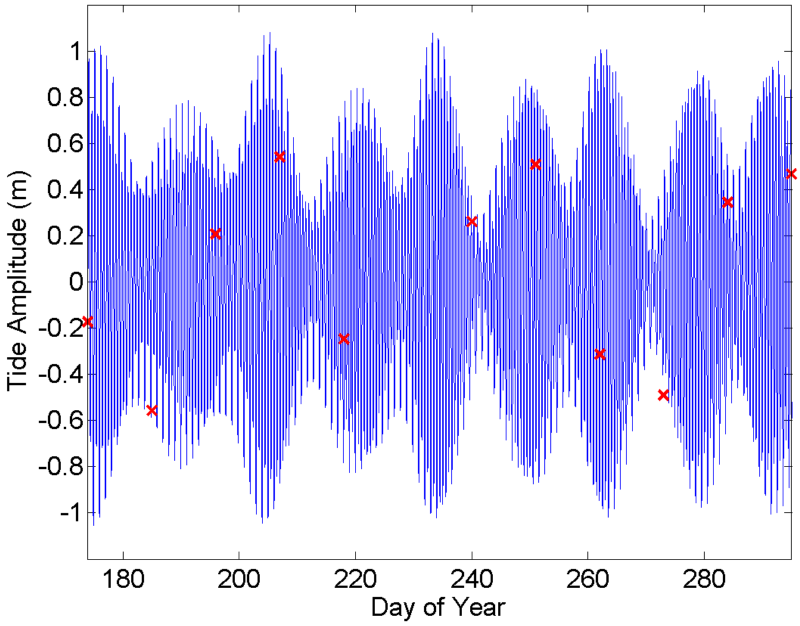

Figure 4-3. *Ocean tide amplitude retrieved every hour from the AODTM-5 Arctic tide model between the 23rd June 2009 and the 22nd October 2009 (blue line) at Peterman Glacier (Figure 4-2). The model tide amplitude prediction retrieved at the time of each TerraSAR-X SAR acquisition (red cross) (Table 4-1) illustrates that the tidal range sampled by the SAR data is 50 % less than the total tide range estimated for the study period.*

4.5 Ice Speed Methods and Results

4.5.1. Tracking Ice Motion

Ice surface velocity was measured on Petermann Glacier during the 4 month study period using standard two-dimensional (2D) offset tracking of intensity features (Strozzi et al., 2002). Temporally sequential repeat pass image pairs were formed from Single Look Complex (SLC) SAR images in the TerraSAR-X time series (Table 4-1). All 10 images were co-registered to the first image (23rd June 2009) of the time series. TerraSAR-X orbital state vectors were used to compute an initial estimate of the global range and azimuth offset fields, which was subsequently refined using offsets calculated from common intensity features on stable, non-deforming terrain outside the known area of fast ice flow, which corresponds to the cyan areas in the 2D surface displacement field (Figure 4-4). The slave images were resampled to the reference frame of the master image by fitting a bilinear polynomial function to the global offsets. Dense networks of local 2D range and azimuth offset fields were determined from the normalised cross-correlation of real-valued intensity features in regularly spaced image patches. We used a 512 by 512 pixel patch size with a 36 pixel step interval (Strozzi et al., 2002). Local offsets with a low signal to noise ratio were rejected, and the 2D range and azimuth surface displacements were then projected into horizontal velocities using an auxiliary ASTER Digital Elevation Model (DEM) (ASTER, 2009) and information on the SAR imaging geometry. On Petermann Glacier, the 2D ice speed measurements are dominated by ice flow in the azimuth direction, with very little surface displacement observed in the range direction (Figure 4-4).

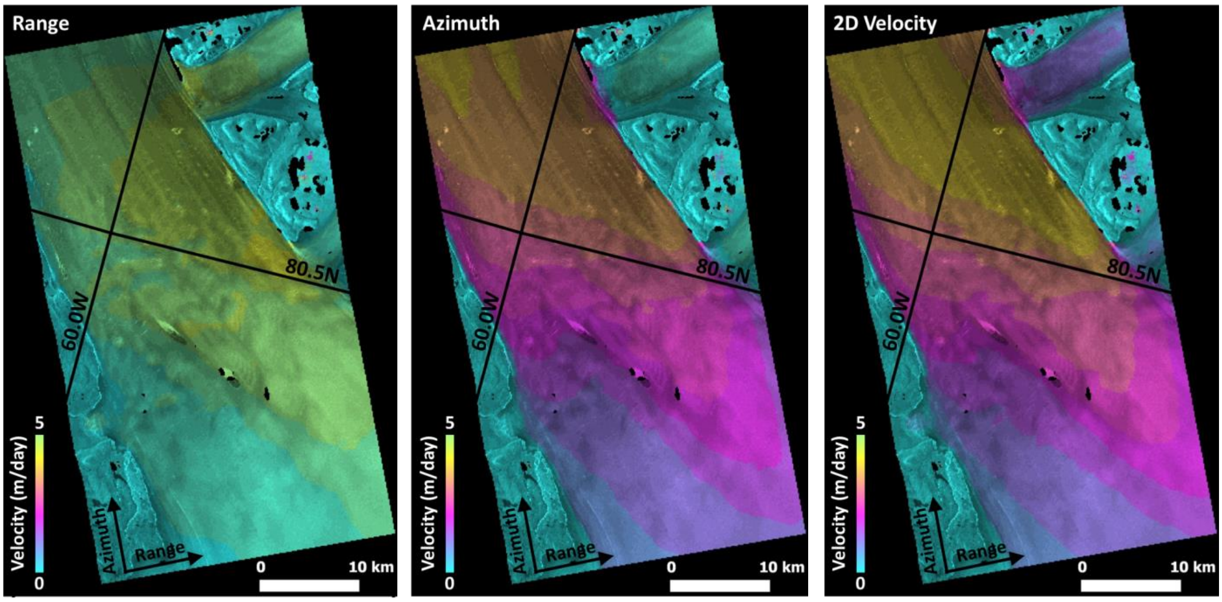

Figure 4-4. *Range, azimuth and combined 2D horizontal surface displacement calculated from the normalised cross correlation of image patches in a pair of TerraSAR-X Synthetic Aperture Radar (SAR) images acquired over Petermann Glacier on the 8th and 19th September 2009 (Table 4-1). Cyan areas show areas with little or no surface displacement and pink and yellow areas represent regions of larger surface displacement.*

4.5.2. Ice Speed Results

4.5.2.1. Spatial Variations in Ice Flow

First, we examined the spatial variability of ice flow at the Petermann Glacier by comparing velocities retrieved within eight 1.5 km by 1.5 km polygons oriented in a stream-wise direction across the centre of the grounding zone (Figure 4-2). It is necessary to measure ice speed variations associated with the seasonal cycle because this signal will be aliased into the differential displacements which are later used to isolate short term variations associated with ocean tides. Throughout the 4 month study period, maximum ice velocities of up to 1.4 km per year (3.7 m per day) were recorded on the floating ice shelf seaward of the grounding line (polygons ‘a’ to ‘d’) (Figure 4-5). Ice velocities retrieved from the floating ice shelf within 15 km of the grounding line were almost constant in each SAR image pair, with a standard deviation of only 11.4 m per year (0.8 % of the maximum speed). Much larger spatial variability was measured on the grounded ice stream where ice velocities ranged from a maximum of 1.3 km per year at the grounding line (polygon ‘d’), to a minimum of 0.7 km per year 20 km inland of the grounding line (polygon ‘h’) (Figure 4-5). The spatial variability of ice speed is an important factor when considering the placement of flux gates used in mass balance calculations, and these results show that on Petermann Glacier a 210 m per year (18.0 %) difference in mean ice speed would be obtained if a flux gate was located just 9.5 km inland rather than at the fastest point at the ice stream grounding line (Table 4-2), which is over 4 times larger than the ice thickness variability over the same distance (± 47.6 m) (Chapter 3; Allen, 2013). Overall the mean ice speed measured on Petermann Glacier in all 8 polygons throughout the 4 month study period was 1.1 km per year, consistent with previous estimates (Nick et al., 2013).

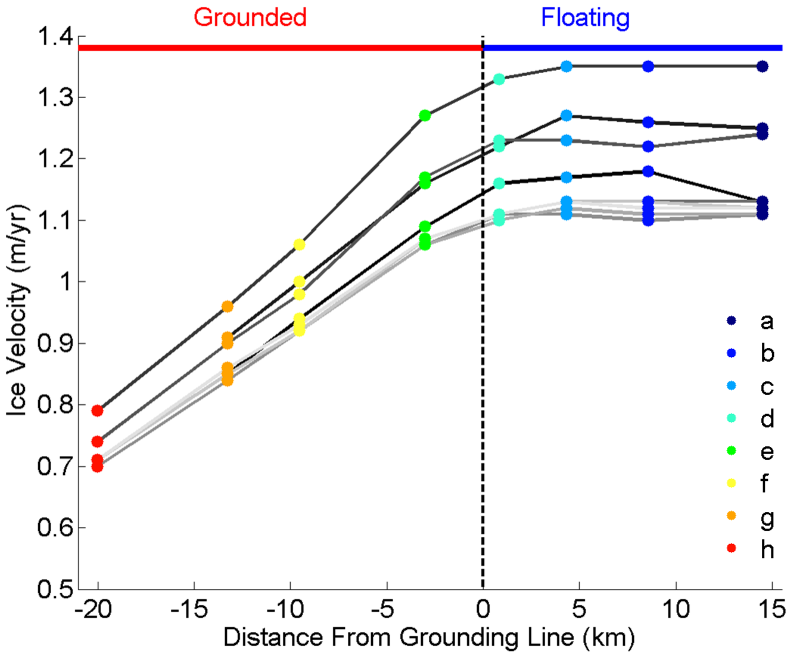

Figure 4-5. *Average rate of ice flow along a stream-wise transect crossing the Petermann Glacier grounding zone (Figure 4-2). Colour coding of the dots in Figure 4-5 corresponds to the colour coding of polygons 'a' to 'h' in Figure 4-2. The grounding line is shown as a black dashed line, and each solid line represents data retrieved from a different SAR image pair in the TerraSAR-X time series from the 23rd June 2009 (solid black line) to the 22nd October 2009 (solid light grey line) (Table 4-1).*

Table 4-2. *Average ice speed measured in polygons 'a' to 'h' (Figure 4-2) throughout the 4 month study period in 2009.*

	Ice speed (km/yr) per polygon							
Master image day of the year	**a**	**b**	**c**	**d**	**e**	**f**	**g**	**H**
174	1.13	1.18	1.17	1.16	1.09	0.94	0.85	-
185	1.25	1.26	1.27	1.22	1.16	1.00	0.91	-
196	1.35	1.35	1.35	1.33	1.27	1.06	0.96	0.79
207	1.24	1.22	1.23	1.23	1.17	0.98	0.90	0.74
240	1.13	1.13	1.13	1.11	1.07	0.92	0.85	0.71
251	1.11	1.10	1.11	1.11	1.06	0.92	0.84	0.70
262	1.11	1.11	1.12	1.10	1.06	0.92	0.85	0.71
273	1.12	1.13	1.13	1.11	1.07	0.92	0.85	0.71
284	1.12	1.12	1.13	1.11	1.07	0.93	0.86	0.71

4.5.2.1. Temporal Variations in Ice Flow

Although there are large spatial variations in the rate of ice flow at the Petermann Glacier (Figure 4-5 and Table 4-2), there are also marked temporal variations, and these will affect our ability to measure grounding line locations in differential range direction offset tracking, because the technique utilises tidal displacement relative to an assumed mean. To account for this, we examined the temporal variations in ice motion in finer detail. At marine terminating glaciers, seasonal variations in rates of ice flow arise due to meteorological forcing, through surface melting and runoff, and due to oceanographic forcing, through changes in the rate of basal glacier ice melting or in the degree of ice melange buttressing at their termini (Howat et al., 2010; Sundal et al., 2011; Sundal et al., 2013; Moon et al., 2014). An appreciation of this seasonal cycle is important when analysing rates of ice discharge, and when designing numerical models of ice flow. At Petermann Glacier, seasonal ice speed variations are thought to be primarily controlled by changes in surface melting during the summer period (Nick et al., 2012), although changes in ocean temperature may also be an influencing factor. Air temperatures measured at an automatic weather station on the Petermann Glacier floating ice shelf (Figure 4-2) showed that during the summer of 2005 the mean temperature rose above 0°C for 71 days (Figure 4-6). In Greenland the number of positive degree days varies annually and therefore air temperatures from 2005 may not adequately represent the conditions in 2009 when the ice speed measurements were made. However, between 2002 and 2005 when the Petermann Glacier ice shelf weather station was in place, the seasonal cycles followed a similar annual pattern with the number of positive degree days varying by a standard deviation of 4 days. This suggests that in the absence of other temporally coincident weather station data, air temperatures from 2005 may be indicative of the annual temperature cycle at this location in 2009 when the seasonal ice velocity was measured.

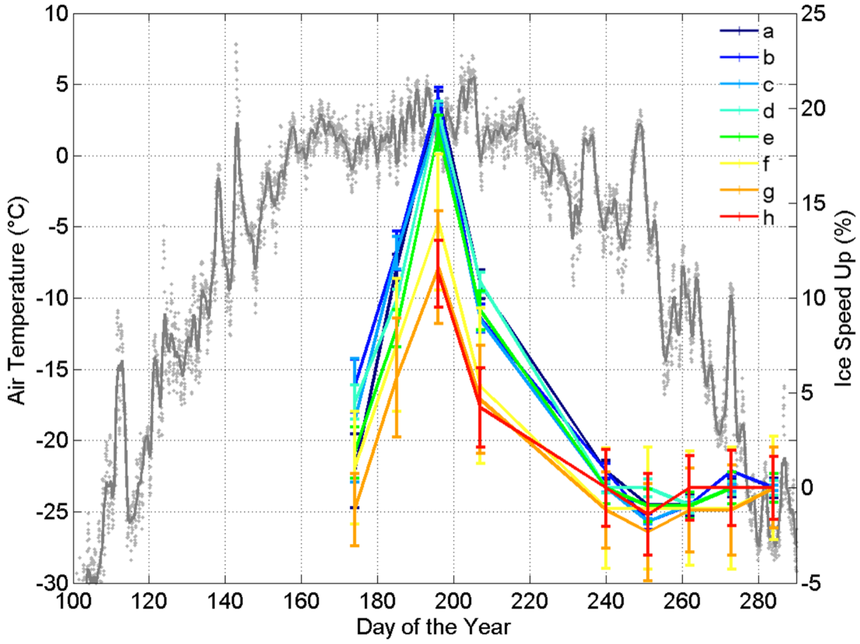

Figure 4-6. *Air temperature with running mean (grey dots and grey line respectively), measured during the 2005 season from a weather station on Petermann Glacier (80.7 N, -60.3 W). Seasonal speedup in ice speed flow on Petermann Glacier between June and October 2009, relative to the slower flowing, autumn average, within 8 polygons distributed along a stream-wise transect crossing the grounding zone (Figure 4-2). Error bars show the standard deviation of the speeds from the mean recorded in each polygon.*

We examined seasonal ice speed variations on Petermann Glacier during 2009 by comparing the mean ice speed recorded in each image pair to the slower flowing, autumn average (Figure 4-6). Along the glacier as a whole, the average summertime speedup peaked at 17.0 ± 4.0 % between 15th and 26th of July in 2009 (Figure 4-6). At this time, a maximum speed up of 20.5 % occurred at a location 14.5 km seaward of the grounding line (Figure 4-7), and a speedup of 11.3 % was recorded 20 km inland, at the limit of the TerraSAR-X image. Our result is commensurate with ice speed observations from other Greenland ice streams where the seasonal cycle was observed up to 30 km inland of the grounding line (Howat et al., 2010; Joughin et al., 2014a). Although sampled in different years, the period of summertime ice speed up in 2009 coincides with the period of summer melting in 2005 (Figure 4-6), with the peak speed up occurring at approximately the same date (days 196 to 207) as the midpoint of summer melting (day 192). This suggests that the Petermann Glacier seasonal ice speed cycle is driven by surface melting; however, the magnitude of the ice speed up is smaller than the summer cycle observed on ice streams in the South West of Greenland (>50 %) (Joughin et al., 2008). In 2009, speed up had started by the 23rd of June, and following a ~2 month autumn slowdown ice velocities reached a minimum speed of 1.3 ± 0.7 % less than the annual mean between the 8th and 19th of September. Recent observations of seasonal ice speed on Jakobshavn Isbrae showed a much larger peak summer speed up of over 90 % in 2012 relative to the previous winter minimum (Joughin et al., 2014a). Although the seasonal flow variability observed on Petermann Glacier is significantly smaller than on Jakobshavn Isbrae, the Jakobshavn Isbrae 2012 peak was 30 % to 50 % greater than previous seasonal maxima demonstrating that there can be significant interannual variability in the seasonal cycle (Joughin et al., 2014) which should be characterised and monitored.

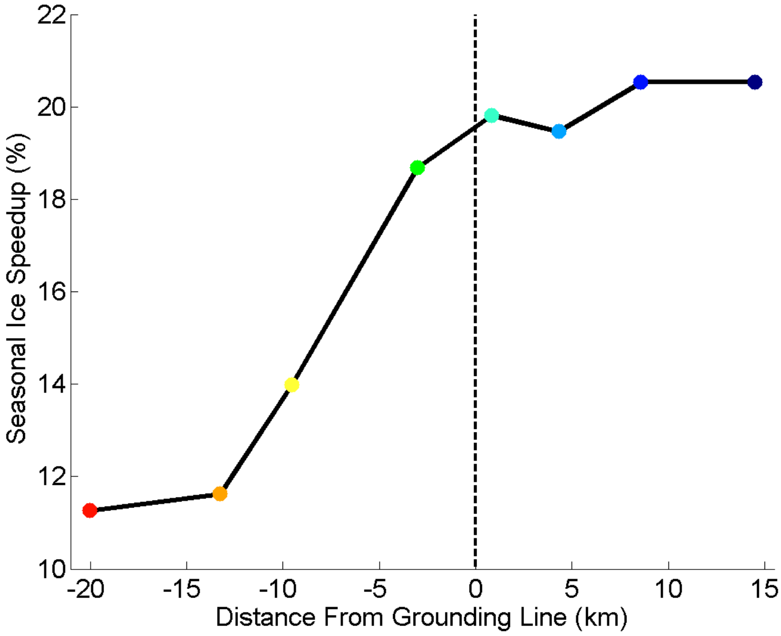

Figure 4-7. *Peak seasonal ice speed variation observed along a stream-wise transect of the Petermann Glacier (Figure 4-2) between 11.3 % and 20.5 % faster relative to the slower flowing, autumn average speed. Colour coding of the dots in Figure 4-7 corresponds to the colour coding of polygons 'a' to 'h' in Figure 4-2 and the grounding line is shown as a black dashed line.*

4.6 Grounding Line Methods and Results

4.6.1. Grounding Line Methods

4.6.1.1. Differential Range Direction Offset Tracking

Vertical displacement of a floating ice shelf causes a change in slant range path length which is visible in the ground range direction offsets, provided the range resolution of the SAR sensor is sufficiently fine. SAR range resolution can be calculated from the bandwidth (β) and speed of light (c) (Equation 4) (Jackson and Apel, 2004). Strip map mode TerraSAR-X data has a ~1 m range resolution (β = 150 MHz; Eineder et al., 2008) which is smaller than the amplitude of the displacement caused by a differential ocean tide (Table 4-1), enabling this signal to be detected.

$$Range\ Resolution = \frac{c}{2\beta} \tag{4}$$

Previous studies have discussed the suitability of TerraSAR-X for measuring tidal displacement from incoherent offset tracking, and have applied the technique to a single set of image pairs (Joughin et al., 2010; Hogg et al., 2013; Marsh et al., 2013). We developed a method for detecting ice sheet grounding lines using differential range direction offset tracking (DRDOT) to measure ice shelf vertical displacement caused by ocean tides, and we comprehensively assess the results through an intercomparison with QDInSAR. On Petermann Glacier of the 1.1 km/yr total mean 2D ice speed, approximately 92 % occurs in the azimuth direction and 8 % occurs in the range direction (Figure 4-4). At high tide amplitudes, vertical displacement of the floating ice shelf will comprise a significant and measurable component of the range direction surface displacement (Joughin et al., 2010). For example, a 1 m vertical displacement equates to 42 % of the range (0.24 m/day) and 4 % of the azimuth (2.77 m/day) mean daily surface displacement respectively. We calculated the mean range direction offsets using all 9 range direction offset tracking images in the TerraSAR-X time series. The mean range direction surface displacement map has a small residual differential tide amplitude of -0.01 m on the floating ice shelf (Table 4-1). A time series of 9 differential range direction offset tracking (DRDOT) maps (Figure 4-8) were produced from the difference between each individual range direction offset map and the mean, and the differential motion was projected into vertical displacement using the satellite imaging geometry. Image pairs with high differential tides (GL_02, GL_04, GL_06, GL_08) show a significant change in surface displacement on the floating and grounded ice stream either side of the 1995 QDInSAR grounding line (Figure 4-8).

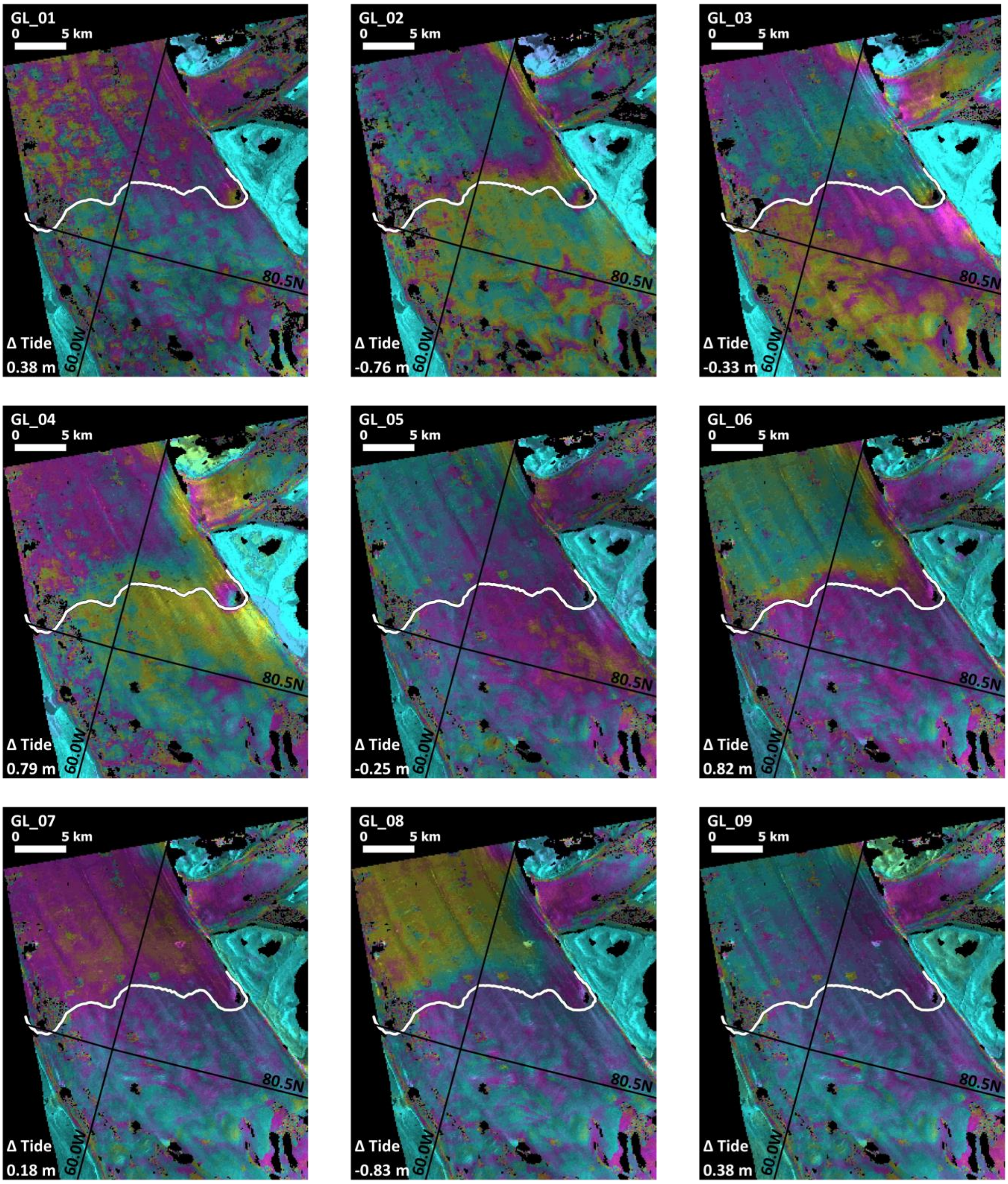

Figure 4-8. *Maps of differential range direction offsets tracked in all 9 TerraSAR-X image pairs acquired over Petermann Glacier (Table 4-1). The location of the QDInSAR grounding line (white line) is shown along with the differential model tide prediction (Δ Tide) extracted from the AODTM-5 tide model at Petermann Glacier (Figure 4-2).*

When calculating the differential range direction offsets (Figure 4-8), the differences are computed relative to the average of the full sequence. However, the seasonal ice speed variations (Figure 4-6) will also be aliased into the differential offsets, because they are not compensated for when computing the sequence average motion. To account for these effects, we quantified correction factors equal to the magnitude of the seasonal ice speed variations in the range offsets at each epoch. We calculated these correction factors from the displacement anomaly measured along the inland grounded portion of the Petermann Glacier, where tidal motion does not occur (Figure 4-2). The correction factor has a 2.1 metre range and inversely mirrors the seasonal ice speed cycle, peaking at 0.7 m for GL_05 at the time of the slower flowing, minimum speed, and reaching a minimum of -1.4 m for GL_03 at the time of the peak summer speedup. After applying the correction factor to account for the impact of seasonal velocity changes, the tidal displacement of Petermann Glaciers' floating section is clearly visible in the differential range direction offsets (Figure 4-9). All 9 TerraSAR-X images pairs show low levels of displacement inland of the QDInSAR grounding line compared with larger vertical displacements of up to 1.5 m on the floating ice shelf. Vertical displacement of this magnitude is in line with predictions of differential tide at Petermann Glacier (Figure 4-3). An assessment of the differential tide amplitudes retrieved from the AOTIM-5 tide model at Petermann Glacier suggests that for the DRDOT technique to be successful, an estimated differential tide greater or less than 0.5 m needs to be present in order for vertical displacement of the ice shelf to be resolved by the DRDOT technique.

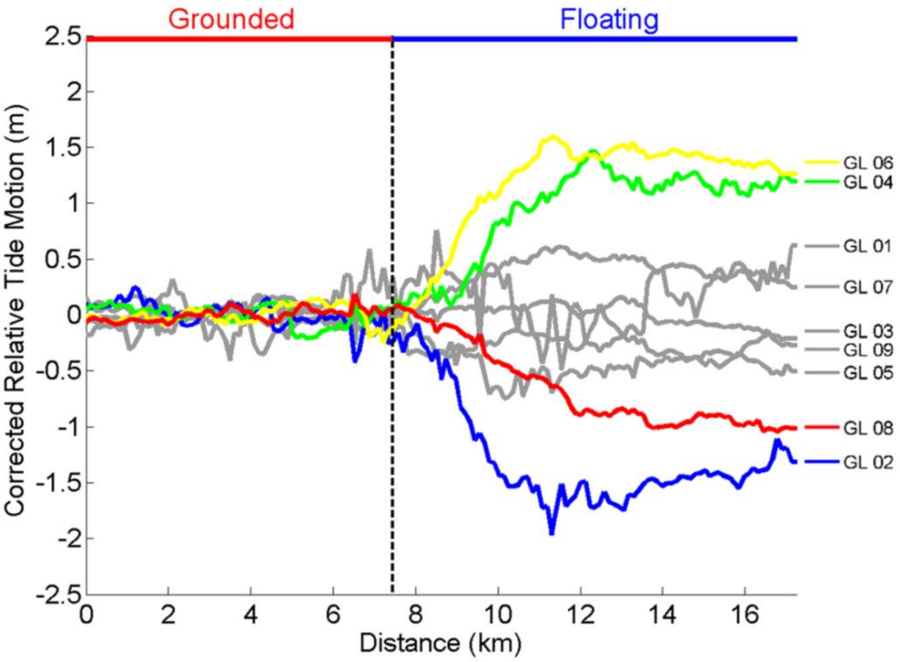

Figure 4-9. *Differential vertical displacement, corrected for seasonal ice speed variations, along a stream-wise transect of the Petermann Glacier (Figure 4-2) as determined from 9 TerraSAR-X image pairs (Table 4-1). The vertical displacement retrieved from image pairs GL_02 (blue line), GL_04 (green line), GL_06 (yellow line) and GL_08 (red line) is sufficiently large to identify the glacier grounding line as the limit of tidal flexure and to pick a grounding line. The location of the 1995 grounding line derived from QDInSAR is also shown (black dashed line).*

4.6.1.2. Delineating the Grounding Line

We map the grounding line position as the inland limit of tidal flexure in the differential range direction offset tracking maps, following the same approach employed when using maps of relative tidal displacement derived from QDInSAR (Park et al., 2013; Rignot et al., 2014). Differential ocean tides were sufficiently large (> 0.5 m) in 4 out of the 9 image pairs to affect a significant vertical displacement of the floating ice shelf relative to the stable grounded ice stream, allowing the zone of flexure to be identified (e.g. Figure 4-10). To increase the contrast between floating and grounded ice, the sign of the displacement anomaly was determined and then the range direction offsets were colour coded between 0 and 0.5 m to ensure the flexure zone was consistently viewed. Grounding lines were manually delineated as the inland limit of flexure determined to be the location where no vertical displacement was first recorded. The Petermann Glacier grounding line was measured in image pairs GL02, GL_04, GL_06 and GL_08 (Table 4-1), and in all 4 differential range direction images it was not possible to identify the inland limit of tidal flexure at the

Western margin at up to ~ 4.5 km from the shear zone, due to a poor signal to noise ratio. The error on the DRDOT measurement was estimated by converting noise in the vertical displacement profiles to a lateral error in the grounding line position. A running mean was computed from profiles of vertical displacement retrieved along Transect 1 (Figure 4-2), from the 4 differential range direction tracking images that were successfully used to measure the grounding line. We computed the residuals as the difference of each point from the mean, and then extracted the standard deviation of the residuals at the grounding line. This was converted into lateral error in grounding line position by measuring the distance seaward of the grounding line over which the mean vertical displacement was within the range of error. The mean absolute variability of the DRDOT residuals is 4.9 ± 2.0 cm with a total range of 57.1 cm. This is 89 % greater than the noise measured in vertical displacement retrieved from QDInSAR at the same geographic location. The mean lateral accuracy of the DRDOT grounding line position is 0.8 ± 1.0 km with a total range of up to 2.1 km, which is 163.2 % of the mean grounding line separation (0.5 km). This indicates that significant portion of the grounding line variability observed using the DRDOT technique may be attributable to measurement error rather than real change in grounding line position. This confirms that although the grounding line position can be measured using DRDOT, phase sensitive techniques such as QDInSAR are able to measure vertical displacement with much greater vertical precision.

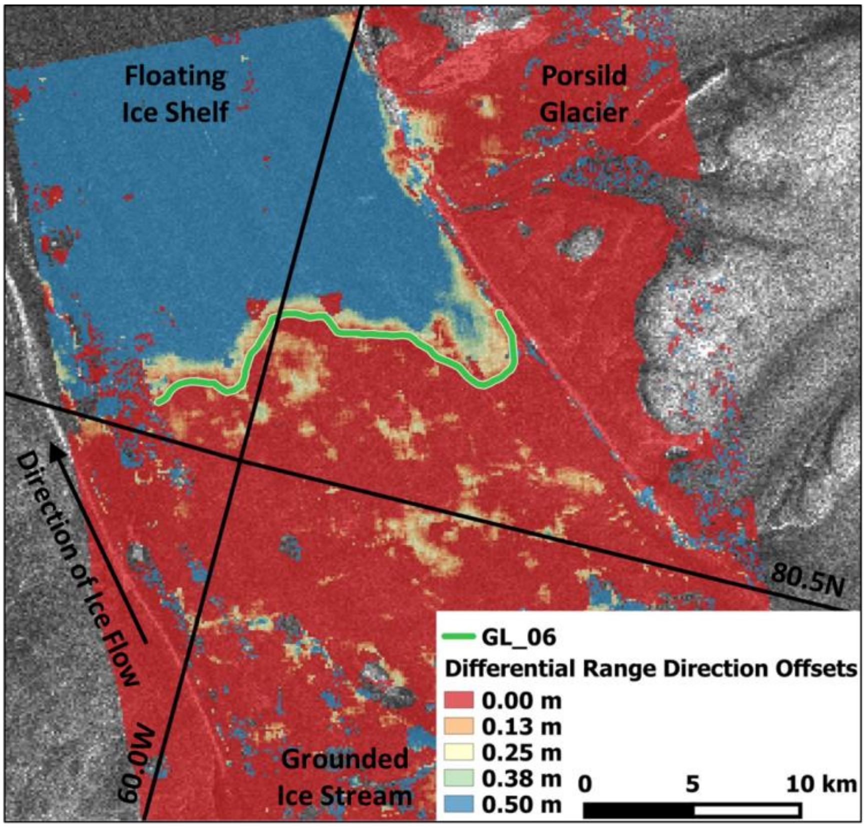

Figure 4-10. *Petermann Glacier tidal flexure (colour scale) and grounding line (green line) located using differential range direction offset tracking (DRDOT) of TerraSAR-X data acquired on the 8th and 19th of September 2009. Grounded ice inland of the grounding line shows low levels of vertical displacement, whereas the floating ice shelf exhibits more than 0.5 m of relative displacement.*

4.6.2. Grounding Line Results

4.6.2.1. Intercomparison of DRDOT and QDInSAR Grounding Line Positions

The Petermann Glacier grounding line has previously been mapped on numerous occasions between 1992 and 2011 using the established technique of quadruple difference interferometry (QDInSAR) (Rignot et al., 1998a; Chapter 3). We used a grounding line determined from ERS-1 and ERS-2 QDInSAR data acquired between 28th October 1995 and 1st March 1996 to evaluate the performance of the differential range direction offset tracking (DRDOT) technique presented in this paper. All four DRDOT grounding lines reproduce the approximate location and relative shape of the QDInSAR grounding line, including distinctive features such as the inland pointing notch at the East ice stream margin (Figure 4-11). The absence of any significant change in grounding line position between the 1995/6 and 2009 confirms that no significant grounding line retreat has occurred on Petermann Glacier, in line with previous studies (Chapter 3). We assessed the variability of the 4 DRDOT grounding lines by calculating the separation with respect to the QDInSAR grounding line along 5 transects across the ice stream grounding zone (Figure 4-2). Along these 5 transects, the mean separation of the differential range direction offset tracking grounding lines was 1.3 ± 1.2 km, with a minimum and maximum separation of -1.5 and 5.3 km respectively, where positive values correspond to inland migration (Table 4-3). Previous studies have observed unusually large grounding line variability on the inland notch on the Eastern ice stream margin which is not characteristic of the rest of the grounding line (Chapter 3). Our results also show greater variability in the DRDOT grounding line in this region, with a 69 % larger mean separation observed on Transect 7 in comparison to Transect 6, the next most variable transect (Figure 4-11). The sensitivity of grounding lines in this region may indicate the presence of locally shallow bedrock slope. Excluding this region from the analysis, the mean separation of the DRDOT and QDInSAR grounding lines is reduced by 39 % to 0.8 ± 0.9 km (Table 4-3) with a corresponding 63 % reduction in the range.

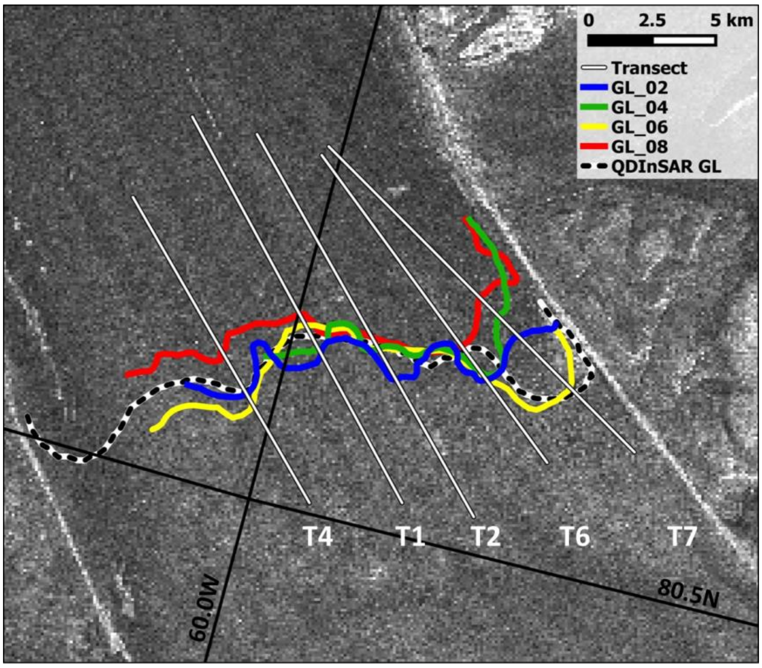

Figure 4-11. *Grounding line positions (GL_02 (blue line), GL04 (green line), GL_06 (yellow line), GL_08 (red line)) picked from differential range direction offset tracking (DRDOT) images (Table 4-1), shown relative to the 1995 grounding line measured using quadruple difference interferometry (QDInSAR) (black and white dashed line) (Chapter 3). The line colour coding used in this plot corresponds to the vertical displacement profiles (Figure 4-9).*

Table 4-3. *Separation of the grounding lines determined from differential range direction offset tracking (DRDOT) of TerraSAR-X data acquired in 2009 and from ERS-1/2 QDInSAR data acquired in 1995/6 (Chapter 3).*

Transect	Mean ± SD (km)	Min (km)	Max (km)	Range (km)
1	0.7 ± 0.9	-0.8	1.0	1.8
2	0.5 ± 0.8	-1.5	0.4	1.9
4	0.9 ± 1.3	-0.6	1.9	2.5
6	1.0 ± 0.8	-1.5	0.2	1.6
7	3.2 ± 2.2	0.3	5.3	5.0
Combined: All	**1.3 ± 1.2**	**-1.5**	**5.3**	**6.8**
Combined: Transects 1 to 6	**0.8 ± 0.9**	**-1.5**	**1.9**	**2.5**

4.6.2.2. Wider Implications for the DRDOT Technique

Our results demonstrate that incoherent TerraSAR-X SAR data can be used to detect ice shelf tidal displacement (Figure 4-10), and to delineate the grounding line as the landward limit of ice shelf tidal flexure (Figure 4-11). Along one transect (Transect 1, Figure 4-2), the mean absolute variation in grounding line position recorded in 4 DRDOT images was 0.8 ± 0.9 km, similar to that observed in a sequence of 17 QDInSAR images (0.5 ± 0.003 km; Chapter 3). Although the QDInSAR technique provides significantly improved definition of the grounding zone, it has been shown (Chapter 3) that short-term variations in grounding line position of around 0.5 km arise due to a range of factors, including changes in tidal displacement, ice thickness, and ice speed. More extensive studies are required to improve our understanding of the magnitude of short and long term grounding line variability, and how this varies on different ice streams. The DRDOT technique is a useful additional tool which can be used to increase the number of grounding line measurements by utilising the extensive archive of TerraSAR-X SAR data. In the future, it should be possible to improve the accuracy of the DRDOT technique by using SAR data with a finer range resolution such as TerraSAR-X spotlight mode (~0.5 m, β = 300 MHz). SAR missions such as Sentinel-1 have a much larger swath width (250 km in interferometric wide mode) than high resolution sensors such as TerraSAR-X which enables data to be acquired over a much wider area. The 12-day repeat period is too long to maintain phase coherence on fast flowing ice streams; however, if Sentinel-1 SAR data was acquired in strip map mode then the range resolution

(β = 87.6 MHz; Aulard-Macler et al., 2011) may prove capable of resolving large differential tide displacements using the DRDOT technique.

Previous studies have discussed the suitability of TerraSAR-X for measuring tidal displacement from incoherent offset tracking, and have applied the technique to a single set of image pairs (Joughin et al., 2010; Hogg et al., 2013; Marsh et al., 2013). Here, we outlined and applied the method, provided a comprehensive evaluation of the results, and quantified the error in the technique through an intercomparison with QDInSAR. We also developed an approach to account for the effects of seasonal variations in ice flow, which are commonplace in Greenland. An assessment of the differential tide amplitudes predicted by the AOTIM-5 tide model at Petermann Glacier suggests that for the DRDOT technique to be successful, a differential tide greater than 0.5 m in amplitude needs to be present to allow vertical displacement of the ice shelf to be resolved by the DRDOT technique.

Grounding lines are of critical importance because they delimit the lateral extent of the ice sheet, and when retreat is observed it indicates the presence of dynamic instability which forms a significant component of the present day ice sheet contribution to sea level rise. However, poor spatial and temporal coverage of SAR data has limited the extent to which changes in grounding line position have been measured. A notable exception is the Amundsen Sea Sector in West Antarctica where retreat in excess of 30 km has been observed over the last 19 years (Park et al., 2013; Rignot et al., 2014). However, to date even in the most frequently monitored area of known retreat, the grounding line position has only been observed at 5 epochs during the satellite era. Our results have showed that using differential range direction offset tracking it was possible to successfully measure the grounding line 4 times within a short 4 month study period, only 1 less than 19 years of multi-mission SAR datasets have yielded elsewhere. In the future differential range direction offset tracking can be applied to historical and future incoherent SAR data to compliment the accurate, yet spatially and temporally sparse record of QDInSAR grounding line positions, allowing short term controls on grounding line position to be studied, and new areas of grounding line migration to be identified and monitored.

4.7 Conclusions

We present and evaluate a new technique for mapping ice sheet grounding lines using differential range direction offsets calculated from the normalised cross correlation of image patches in real-valued, incoherent, Synthetic Aperture Radar (SAR) intensity data. We have applied the technique to map the grounding line position of the Petermann Glacier in Northwest Greenland in the summer of 2009 using a sequence of 11 TerraSAR-X SAR images. The glacier exhibited a marked seasonal ice speed cycle during the survey period, with peak summer speeds up to 20.5 % greater than in autumn seaward of the grounding line, and it was necessary to account for the effects of these variations when mapping tidal flexure. Air temperature records acquired between 2002 and 2005 suggest that the seasonal ice speed cycle recorded in 2009 is temporally coincident with the typical period of summer melting. This provides supporting evidence to numerical model simulations which suggest that runoff may drive the seasonal variations in ice flow at Petermann Glacier (Nick et al., 2012). In the future, more frequent temporal sampling of ice speed on key outlet glaciers is required over multiple years to enable the seasonal and annual ice speed variations to be resolved and monitored, which will help improve our understanding of the underlying environmental forcing mechanisms controlling seasonal variability.

An assessment of modelled ocean tides indicates that the DRDOT technique is successful when the differential tide is greater than 0.5 m in amplitude. Given the spread of differential ocean tides, we have been able to map the Petermann Glacier grounding line position on 4 out of 9 possible occasions during the 4 month study period. This is a substantial increase in frequency when compared to the alternative technique of QDInSAR, which has been used to measure the grounding line on a maximum of 5 occasions in the last 23 years (Park et al., 2013; Rignot et al., 2014). Our differential range direction offset tracking results provide independent confirmation that, prior to 2009, the Petermann Glacier was a stable tidewater glacier which did not experience grounding line retreat during the study period (Chapter 3). The DRDOT technique can be applied to historical and future incoherent SAR data to compliment the accurate, yet spatially and temporally sparse record of QDInSAR grounding line positions, which will allow areas of change to be identified and monitored.

Chapter 5

Locating the Antarctic Ice Sheet Break In Surface Slope Using CryoSat-2

5.1 Abstract

The boundary between grounded and floating ice is an important glaciological parameter, because it delineates the lateral extent of an ice sheet and it marks the optimal location for computing ice discharge. We present a method for detecting the grounding line as the break in ice sheet surface slope, computed from CryoSat-2 elevation measurements using a plane-fitting solution. We apply this technique to map the break in surface slope in four topographically diverse sectors of Antarctica - the Filchner-Ronne ice shelf, the Ekström ice shelf, the Amundsen Sea Sector, and the Larsen-C ice shelf - using CryoSat-2 observations acquired between July 2010 and May 2014. An inter-comparison of the CryoSat-2 break in surface slope with independent measurements of the hinge line position determined from quadruple-difference synthetic aperture radar interferometry (QDInSAR) shows good overall agreement, with a mean separation of 4.5 km. In the Amundsen Sea Sector, where in places over 35 km of hinge line retreat has occurred since 1992, the CryoSat-2 break in surface slope coincides with the most recent hinge line position, recorded in 2011. The technique we have developed is automatic, computationally-efficient, and can be repeated given further data, and offers a complimentary tool for monitoring changes in the lateral extent of grounded ice.

5.2 Introduction

Grounding lines mark the boundary between floating and grounded sections of a marine terminating ice sheet on the sea floor (Thomas et al., 1979). They are a sensitive indicator of ice sheet stability and, when migration occurs, can indicate the influence of changes in the local environmental forcing (Joughin et al., 2010; Joughin et al., 2012; Dutrieux et al., 2014; Joughin et al., 2014b). Monitoring changes in grounding line positions allows regions of instability to be identified, and such measurements are a valuable reference for assessing the fidelity of ice dynamical models (Favier et al., 2014). The location of the grounding line can fluctuate on short (sub-daily) timescales, due to the effects of ocean tides and localised variations in ice thickness (Chapter 3), and over longer (annual to decadal) timescales, if sustained changes in ice thickness occur (Rignot, 1998b; Park et al., 2013; Rignot et al., 2014). The grounding line lies at the landward edge of a zone where ice shelf flexure occurs as a consequence of tidal displacement. This flexure zone can be over 4 km wide in the flow-line direction (Chapter 3) depending on factors such as bed topography, ice thickness and tide amplitude (Rignot, 1998b). Although grounding lines cannot be directly observed because they lie at the base of the ice sheet, their surface expression – the hinge line - can be detected using a range of in situ and remote-sensing techniques (Rignot, 1998b, Fricker and Padman, 2006). Although there may be small departures between the lateral positions of hinge- and grounding-lines (Figure 5-1), in areas of high basal sheer their migration rates are similar, and so tracking hinge line movement is an accurate measure of grounding line migration or stasis (Rignot, 1998b).

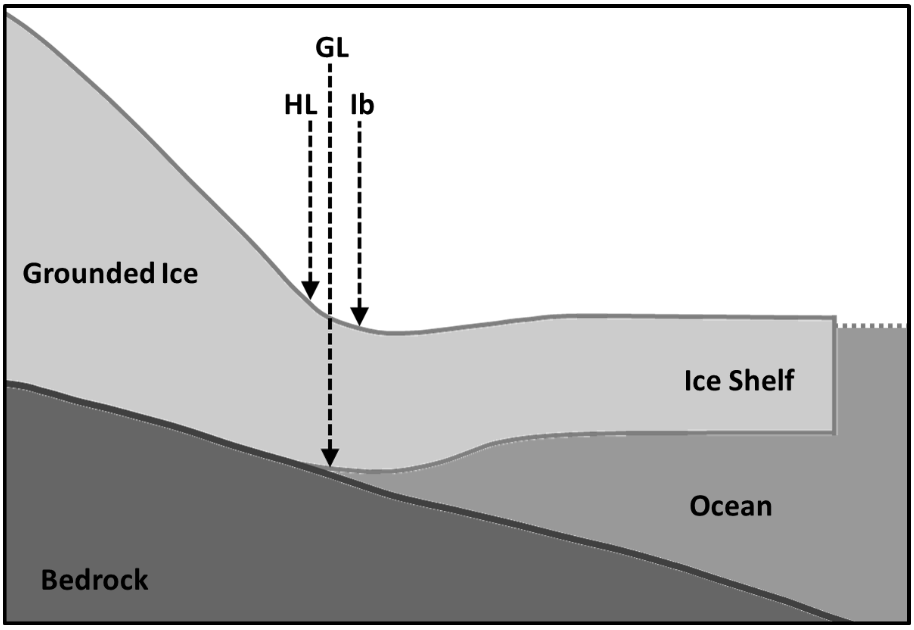

Figure 5-1. Illustration showing the location of the ice sheet grounding line (GL), hinge line (HL), break in surface slope (Ib) (adapted from Bindschadler et al., 2011).

Three techniques have been used to map ice sheet grounding lines using satellite observations; quadruple difference interferometric synthetic aperture radar (QDInSAR) (Rignot, 1998a), repeat laser altimetry (Fricker and Padman, 2006; Horgan and Anandakrishnan, 2006; Fricker et al., 2009; Brunt et al., 2010) and shadow in optical satellite imagery (Bindschadler et al., 2011). Each approach has strengths and weaknesses. Although QDInSAR provides a precise measurement of relative tidal displacement with fine spatial resolution, the spatial and temporal extent of suitable data is relatively poor, and there are few regions where the method has been applied repeatedly. Ice shelf tidal displacement is also detectable in repeat laser altimetry. The most extensive assessments are based on measurements acquired by the Ice, Cloud, and land Elevation Satellite (ICESat), but the mission lifetime was relatively short (6 -years), and the ground track coverage is relatively sparse. Finally, the break in ice sheet surface slope which often occurs in the vicinity of the grounding line causes, when correctly illuminated, shadow in optical satellite imagery (Bindschadler et al., 2011). The Antarctic Surface Accumulation and Ice Discharge (ASAID) project has produced a continuous grounded ice boundary for Antarctica through manual delineation of the shadow edge boundary, which in regions of markedly breaking slope agrees well with hinge lines detected using QDInSAR (Bindschadler et al., 2011); however, the technique is laborious and not easily repeatable. While progress has been made using all three techniques, the spatial and temporal extent of grounding line data sets remains sparse.

In areas of high basal sheer, the ice surface evolves in response to changes in grounding line location (Schoof, 2007; Joughin et al., 2010), and this relationship is the motivation for the use of the break in surface slope (Ib) (Figure 5-1) as a proxy for the grounding line position (Bindschadler et al., 2011). Here, we develop a computationally efficient, automated method for mapping the break in slope using geodetic surface height measurements, to assess the validity of this assumption. We map the break in slope using CryoSat-2 data in 4 topographically diverse study areas of Antarctica, namely the Amundsen Sea Sector, and the Filchner-Ronne, Larsen-C and Ekström Ice Shelves, and we evaluate the extent to which this coincides with the hinge line located using QDInSAR (Rignot et al., 2011).

5.3 CryoSat-2 Data

We use 3 years and 8 months of CryoSat-2 intermediate Level 2 (L2i) Synthetic Aperture Radar Interferometry (SARIn) mode radar altimeter measurements of ice sheet surface elevation, acquired between 16.07.2010 and 04.05.2014, as the basis for our slope calculation. The acquisition date and time, latitude and longitude at the slope corrected point of closest approach (POCA), surface height with respect to the ellipsoid, and the radar backscatter coefficient are obtained for each CryoSat-2 SARIn data point in all 4 areas of interest. Poor quality data is removed using the measurement confidence, measurement quality, retracker and height status flags, all of which are set to zero if the data quality is good. The range between the CryoSat-2 satellite and the ice surface is corrected for fluctuations in dry and wet tropospheric mass, the effect of the ionosphere, inverse barometric atmospheric pressure variations, and the solid Earth and ocean loading tides (Table 5-1). The elevation measurement is re-tided with the long period equilibrium ocean, geocentric polar and ocean tides provided in the ESA CryoSat-2 data product, and then the ocean tide amplitude is simulated and removed from the CryoSat-2 surface elevation measurement using the independent CATS2008 ocean tide model (Padman et al., 2002). We use the CATS2008 ocean tide correction rather than the FES2004 ocean tide correction provided with CryoSat-2 because the spatial extent of the CATS2008 model domain provides a better match to the known ocean - land boundary in Antarctica, and the phase and amplitude of the CATS2008 tide model is more accurate than other tide model simulations in coastal Antarctica (McMillan et al., 2011).

Table 5-1 *Geophysical corrections applied to the CryoSat-2 data and their typical range (CryoSat-2 Product Handbook, 2012).*

Correction	Minimum (cm)	Maximum (cm)
Dry troposphere	170	250
Wet troposphere	0	37
Ionosphere	6	12
Inverse barometric	-15	15
Solid Earth tide	-30	30
Geocentric polar tide	-2	2
Ocean loading tide	-2	2
Ocean tide	-50	50

The novel imaging mode on CroSat-2 improves sampling density in the topographically heterogeneous ice sheet margins making it particularly well suited for mapping slope relative to historical altimeter missions. The surface elevation measured by traditional pulse limited altimeters such as ERS-1/2, is the height of the closest point within the altimeter footprint, the size of which is determined by the altimeter instrument characteristics such as operating frequency, and platform imaging geometry. The SAR Interferometric Radar Altimeter (SIRAL) instrument operates in Synthetic Aperture Radar Interferometry (SARIn) mode in the ice sheet margins, and Low Rate Mode (LRM) in the Ice sheet interior. The CryoSat-2 SARIn mode is designed to improve data retrieval in areas of steeply sloping terrain where traditional pulse limited altimeters do not perform well (McMillan et al., 2014). The return radar signal reflected off the ground surface is received by the two SIRAL antennae mounted 1 m apart on the CryoSat-2 satellite, and any difference in the return signal time is caused by difference in the path length travelled. Difference in travel time can only result if the return signal did not originate at the satellite nadir, and the true echo origin, termed the point of closest approach (POCA), within the 0.3 km (along track) by 1.5 km (across track) CryoSat-2 footprint can be determined from the phase (across track location) and angle of arrival of the return signal (along track location) (Wingham et al., 2006). Furthermore, CryoSat-2 is operated in a 369-day drifting orbit with a 30-day sub cycle. The novel POCA retrieval combined with a drifting orbital cycle dramatically improves the spatial density of radar altimetry measurements retrieved in the ice sheet margins, increasing from 10% by ENVISAT to 49% from CryoSat-2 (McMillan et al., 2014). In the vicinity of the grounding line CryoSat-2 SARIn mode achieves a typical data density of 302 points per 5 km^2 (Figure 5-2).

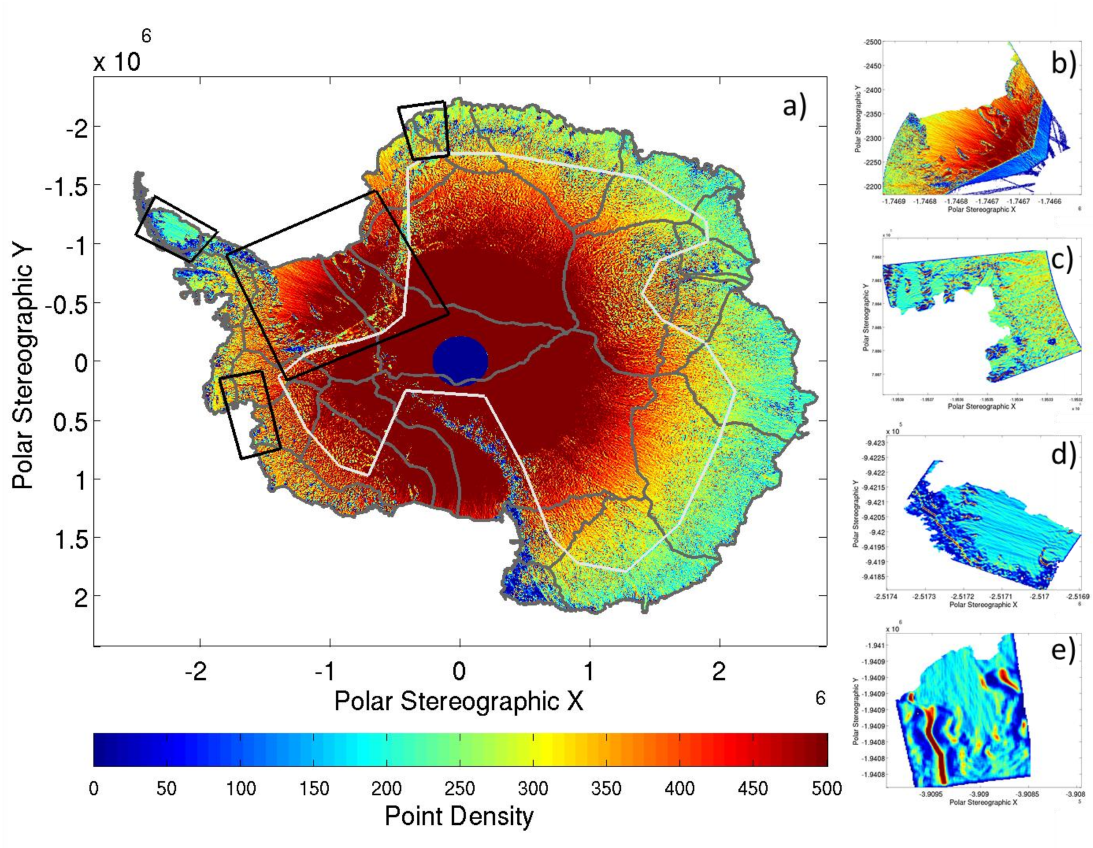

Figure 5-2. a) CryoSat-2 POCA point density per 5 km by 5 km grid cell before the plane fit solution is applied. The location of the four study areas (black box), drainage basin boundaries (grey) (Zwally et al., 2012) and CryoSat-2 SARIn/LRM mode mask boundary (white) is also shown. A close up of the point density for the Filchner-Ronne ice shelf (b), Amundsen Sea Sector (c), Larsen-C ice shelf (d) and Ekström ice shelf (e) is also shown.

An artefact of the SARIn acquisition mode is that high elevation topographic features, such as mountain ridges, are preferentially sampled relative to their surrounding terrain. This is particularly noticeable in the Larsen-C and Ekström ice shelf study areas (Figure 5-2d and e) where there is a high density of POCA points acquired along the spine of the Antarctic Peninsula and the Sorasen Ridge respectively. The disadvantage of this is that the area surrounding prominent topographic features are rarely or never sampled as the POCA, leaving data sparse regions not sampled by standard retracking of the CryoSat-2 SARIn mode data. In regions with complex mountainous terrain we also find a much higher incidence of elevation measurement retrieval error, which in Level 2 CryoSat-2 SARIn mode data is visible as a point located on the default nadir ground track. A CryoSat-2 measurement is deemed to be in error if the surface elevation differs by more than 50 m from an auxiliary 1 by 1 km grid resolution Digital Elevation Model (DEM). The Antarctic

Peninsula is ~70 km wide with mountains reaching over 2.5 km altitude, and consequently some areas within the Larsen-C ice shelf study region have more than 50 m of elevation change within a 1 km^2 area. The Antarctic Peninsula experiences the highest incidence of elevation measurement retrieval failure, however some of this may be attributable to the spatial resolution of the DEM against which the Level 2 CryoSat-2 surface elevation heights are evaluated, rather than error in the CryoSat-2 surface elevation measurement. While it is out of the scope of this study to investigate retracker performance, in the future it may be possible to increase the data density of POCA points in mountainous regions by evaluating Level 2 CryoSat-2 surface elevation data against a finer spatial resolution or more recently acquired DEM.

5.4 Study Areas

The CryoSat-2 break in surface slope was produced in 4 study areas chosen based on their scientific pertinence, availability of evaluation datasets or analogues topography relative to the rest of the Antarctic ice sheet. The Amundsen Sea Sector is grounded on bedrock that lies below current sea level with a topographic gradient that deepens inland towards the Byrd Trench. The region is of particular scientific interest because the low elevation sub-glacial topography allows incursions of warm deep water into the Byrd trench, making the region inherently unstable and particularly susceptible to uncontrolled grounding line retreat (Favier et al., 2014). Over 30 km of hinge line retreat has been observed in the Amundsen Sea Sector over the last two decades (Rignot, 1998b; Park et al., 2013; Rignot et al., 2014), and these observations provide the most extensive hinge line dataset in Antarctica for evaluating the performance of the break in surface slope as a proxy for grounding line position. The Ekström ice shelf study area was selected conversely because of its relative stability, as no significant ice thinning (McMillan et al., 2014) or grounding line retreat has been observed. The Larsen-C ice shelf, located on the Antarctic Peninsula, was selected as a study area because the steep mountainous terrain makes it a challenging region for obtaining reliable altimetry surface elevation measurements (Shepherd et al., 2012). Furthermore, in 1995 (Rott et al., 1996) and 2002 (Rack and Rott, 2004) catastrophic ice shelf collapse was observed on the neighbouring Larsen-A and B ice shelves respectively demonstrating regular, contemporary observations are required to monitor change in one of the most rapidly evolving sectors of the Antarctic ice sheet. The Filchner-Ronne ice shelf was selected as a big ice shelf study area because there is a larger volume of evaluation data available relative to the Ross ice shelf, as a smaller proportion of the grounding line is located in the Polar data gap which exists north of 81 degrees latitude in many right looking satellite missions.

5.5 Methods

5.5.1. Computing Ice Sheet Surface Slope

In the Amundsen Sea Sector, Larsen-C and Ekström ice shelf study areas the corrected and filtered CryoSat-2 data was accumulated into 5 km by 5 km geographical regions on an overlapping grid, with tile centres 1 km by 1 km apart. The grid cell spacing determines the spatial sampling of the CryoSat-2 slope break product, and the grid cell size governs the data density per grid cell which affects the success of the plane fit solution. We find that a 5 km by 5km grid provides the best trade-off solution between coverage and resolution given the volume and spatial coverage of CryoSat-2 SARIn mode data acquired over the 3 year 8 month long study period. We also use 5 km by 5 km square tiles in the Filchner-Ronne study area; however, in order to optimise processing speed for this significantly larger area, we overlap tile centres within 10 km of the auxiliary QDInSAR hinge line (Rignot et al., 2011).

We employed a plane fit solution (Equation 5) to compute surface slope in each grid cell in all 4 study areas (McMillan et al., 2014). Ice surface elevation (z) for each grid cell is modelled as a quadratic function of surface terrain (x, y), time (t), the geophysically corrected local mean surface elevation for each POCA point ($\bar{z}$), satellite heading (h) which is a time-invariant correction for anisotropy in the ascending and descending passes, and backscatter (s) which accounts for time varying properties of the ice sheet surface.

$$z = \bar{z} + a_0 x + a_1 y + a_2 t + a_3 h + a_4 s \qquad (5)$$

Data points deemed to be outliers were culled if there was more than 5 m difference from the modelled surface, and the plane fit solution was iterated for each grid cell until no more data points were removed. The model solution was retained for each individual grid cell if the CryoSat-2 data density is greater than 8 points, and if a time period of 2 years or more is spanned to minimise the influence of short term change. Surface slope was calculated as the gradient of the model plane within each grid cell and inverse-distance 2d interpolation is used to fill in any remaining gaps in the slope map (Figure 5-3a). Surface elevation and slope data retrieved from a transect across the Filchner-Ronne ice shelf illustrates that the QDInSAR hinge line corresponds with the point of most rapid change in surface elevation (Figure 5-3b) and surface slope (Figure 5-3c). At all 4 locations where the QDInSAR hinge line intersects the 1,090 km long transect, the most rapid change in surface slope (Figure 5-3c) corresponds with a peak in the derivative of the surface slope, termed the slope break (Figure 5-3d), greater than 0.1 degree. Slope break (Figure 5-3d and Figure 5-4c) is a more variable measurement than surface slope (Figure 5-3c and Figure 5-4b) because the input altimetry surface slope measurements are unsmoothed, and mountainous terrain far inland of the grounding line exhibits large change in surface slope relative to flat ice shelves. As the slope break and point of most rapid change in surface slope correspond, we pick the position, termed the CryoSat-2 break in surface slope, where surface slope exceeds a specified value, enabling a range of slope values to be evaluated and optimised relative to the QDInSAR hinge line position.

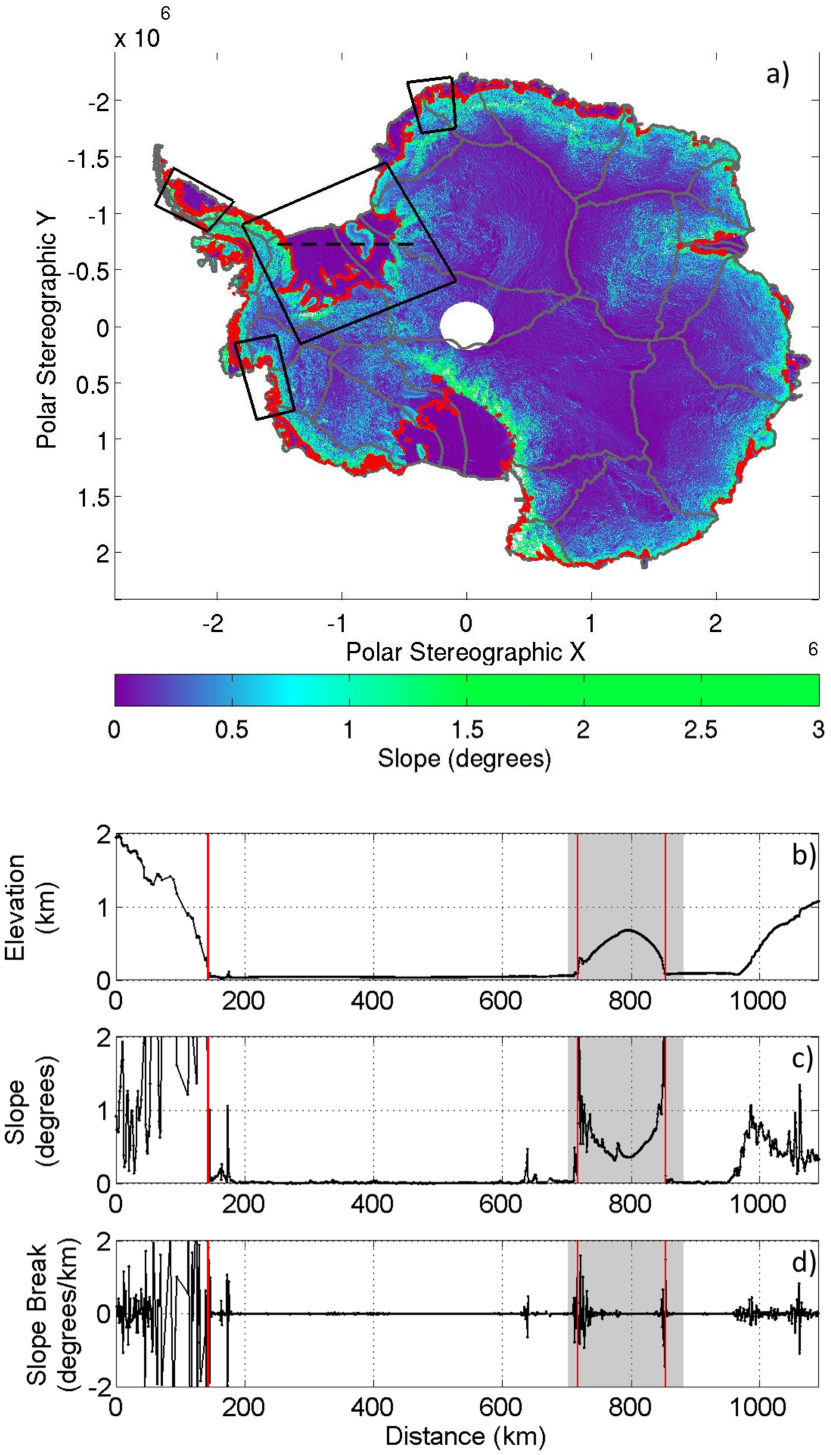

Figure 5-3. *(a) Antarctic ice sheet and ice shelf surface slope measured by CryoSat-2. Also shown are drainage basins (grey) (Zwally et al., 2012), hinge line determined from QDInSAR (red) (Rignot et al., 2011) and the four regions considered in detail in this study (black box). Ice surface elevation (b), slope (c) and slope break (d) along a profile of the Filchner-Ronne Ice Shelf (black dashed line in Figure 5-3a), shown relative to the QDInSAR hinge line crossing points (vertical red lines). The grey shaded area (b, c, d) indicates the location of Berkner Island on the transect.*

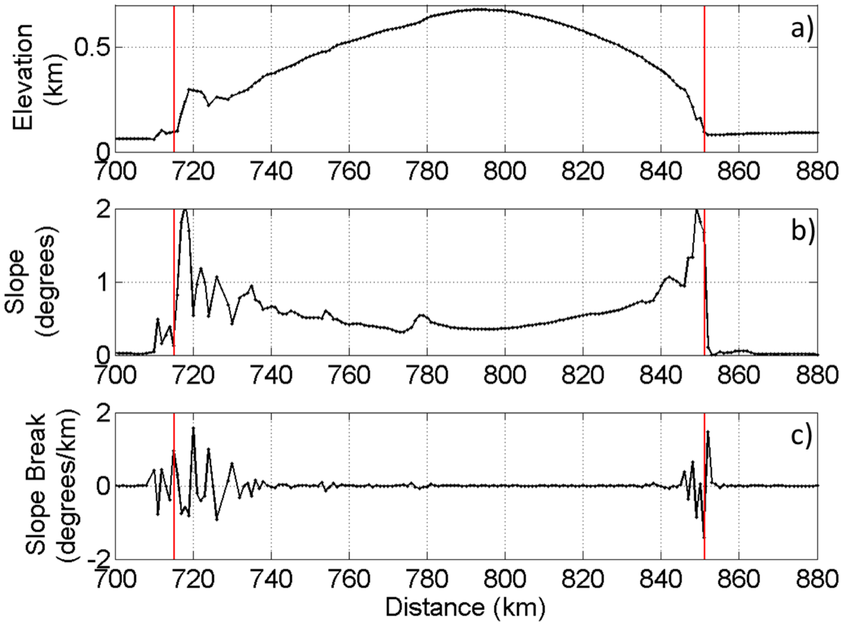

Figure 5-4. *Ice surface elevation (a), slope (b) and slope break (c) across Berkner Island on the Filchner-Ronne Ice Shelf (grey shaded area in Figure 5-3b), shown relative to the QDInSAR hinge line crossing points (vertical red lines).*

5.5.2. Identification of the Break In Surface Slope

As a first step towards locating the break in surface slope, we investigated the range of slopes determined from the CryoSat-2 data in the vicinity of the grounded ice boundary to assess their consistency. In areas with very steep surface slopes there is a very small change in position of the break in surface slope picked at different slope values; however, in regions with shallow surface slope there is a much larger separation. For this, we used hinge line locations mapped between 1992 and 2009 using QDInSAR (Rignot et al., 2011). Although there has been rapid grounding line retreat in parts of the Amundsen Sea sector, the majority of our study area has been in a state of approximate balance according to satellite observations of ice thickness change (Shepherd et al., 2012; McMillan et al., 2014), and so the 17 year mismatch between the two datasets should not adversely affect this assessment as it can be assumed that the surface terrain has not changed. The vast majority of all hinge line positions are located on ice exhibiting very low surface slopes, with over 70 % falling on slopes of less than 1.0 degree (Figure 5-5).

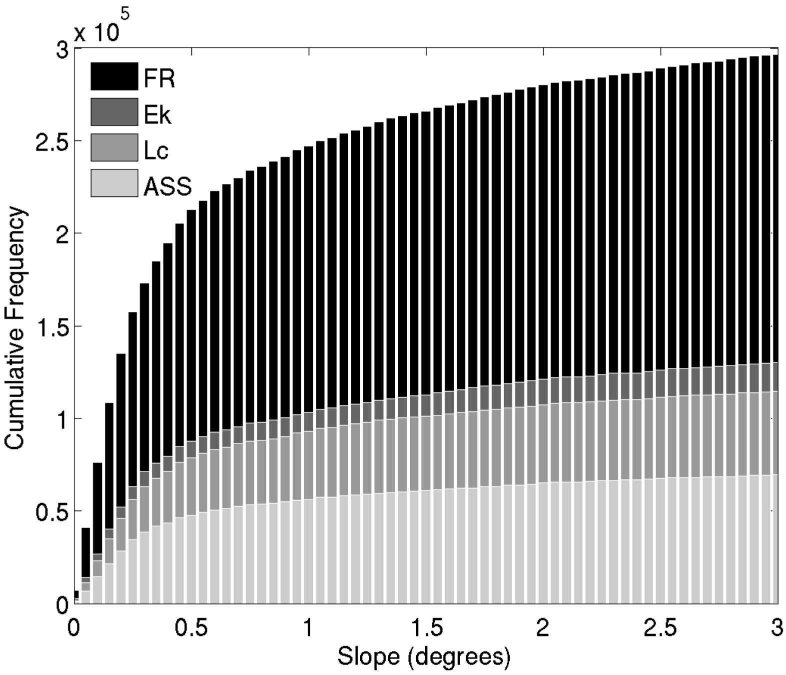

Figure 5-5. *Cumulative frequency of the ice surface slope retrieved at the QDInSAR hinge line in all four study areas. 70.2 % of the data points have slope values of less than 1 degree.*

Taking the range of hinge line slopes into account, we generated contours at 0.1 degree intervals using a bilinear interpolation scheme to mark a continuous line passing between common values of the surface slope. Some line breaks did occur, and so it was necessary to connect large, open contours separated by small gaps (< 25 km) at their closest point. Connecting contour breaks was mainly required on high slope terrain (> 0.5 degree), and illustrates that the continuity of the grounded ice boundary is dependent upon the steepness of the local terrain. It was not possible to produce a continuous contour for slopes greater than 0.9 degrees on the Ekström ice shelf, 0.8 degrees in the Amundsen Sea Sector, and 0.7 degrees on the Filchner-Ronne ice shelf, as the surface slopes were not persistently high enough around large proportions of the coast. We excluded contours surrounding areas smaller than 1000 km^2 as being not representative of the main ice sheet. Although this data editing step is designed to remove boundaries associated with erroneous data, it does also limit the utility of the approach for identifying relatively small regions of grounded ice such as ice rises.

To assess the similarity between the hinge line and break in surface slope, we calculated the mean absolute separation between each point on the QDInSAR hinge line and the nearest point on each slope contour in all four study areas (Figure 5-6). In the Amundsen Sea Sector the mean separation of the QDInSAR hinge line to the CryoSat-2 break in surface slope is over 50 km for the 0.1 degree slope value; however, for slope values between 0.3 and 0.8 degrees the mean separation is less than 10 km. The Ekström ice shelf exhibits a similar pattern to the Amundsen Sea Sector study area with a larger separation measured at lower slope values. However, there is less than 0.01 km difference in the mean separation of the break in surface slope determined from values between 0.5 and 0.7 degrees, indicating that in the Ekström ice shelf study area the break in surface slope is less sensitive to the optimum slope value. The Larsen-C ice shelf region is characterised by steep mountainous terrain typical of the Antarctic Peninsula. Evaluation of the break in surface slope in this region shows that there is over 5 km separation between the QDInSAR hinge line for slope values less than 0.4 degrees or greater than 0.6 degrees. However, the separation of the hinge line and the break in surface slope determined from 0.5 and 0.6 degree slope values exhibit root mean square variability of less than 5 km, suggesting that the performance of the technique is particularly good in this region. Contrary to the 3 other study areas, the mean separation of the QDInSAR hinge line and the CryoSat-2 break in surface slope increases with increasing slope values on the Filchner-Ronne ice shelf. Slope values equal too and less than 0.2 degrees result in a mean separation of less than 10 km indicating that much lower surface slopes are characteristic of this large study area resulting in a significantly lower optimum slope value. The number of unique points (Figure 5-6) provides, additionally, an indication of the completeness of each contour and of the confidence of the inter-comparison. In general, most coincidences occur between slope contours and hinge line positions for slopes in the range 0.2 to 0.8 degrees; for values outside this range, the inter-comparison can be considered less robust. The CryoSat-2 break in surface slope that matches most closely with the hinge line position is determined from slope values of 0.5, 0.6, 0.5 and 0.2 degrees in the Amundsen Sea Sector, Larsen-C, Ekström and Filchner-Ronne ice shelves respectively (Figure 5-6).

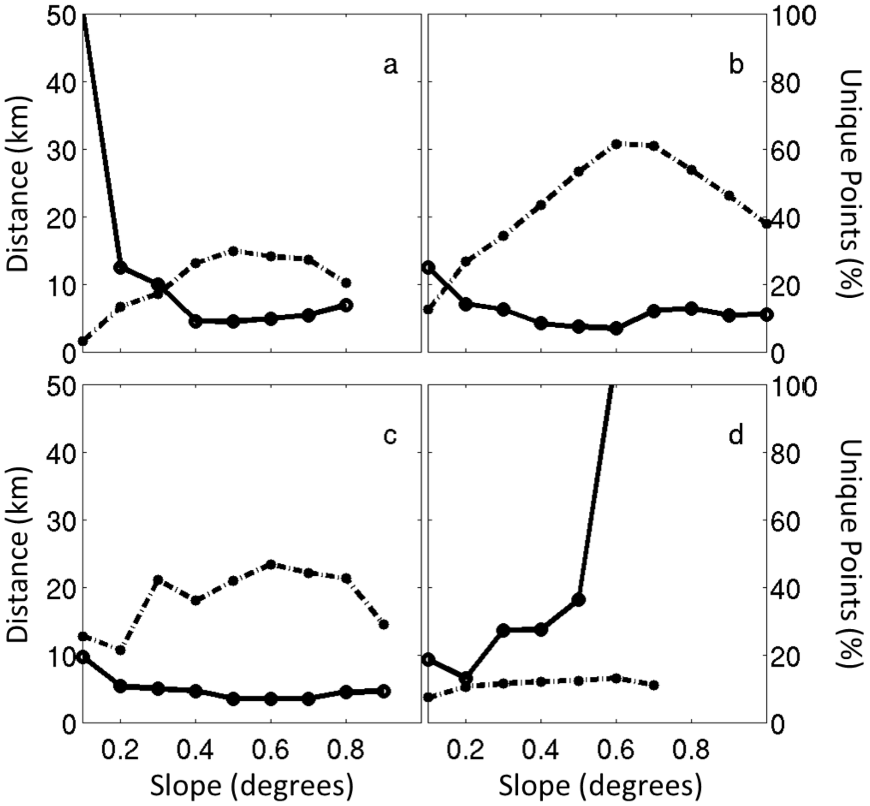

Figure 5-6. *Mean absolute separation between the ice sheet hinge line, as determined from QDInSAR (Rignot et al., 2011) and contours of the ice sheet surface slope, as determined from CryoSat-2 altimetry in (a) the Amundsen Sea Sector, (b) Larsen-C ice shelf, (c) Ekström ice shelf, and (d) Filchner-Ronne ice shelf (solid black line). Also shown is the number of unique points used in each comparison (dashed black line).*

Although there are regional differences in the slope value that marks the break in surface slope optimised against the QDInSAR hinge line, only the Filchner-Ronne ice shelf shows a significant departure from the mean. In the Filchner-Ronne ice shelf study area the smallest mean absolute separation from the QDInSAR hinge line occurs at the CryoSat-2 break in surface slope produced from low slope values, less than 0.3 degrees. However, a different slope regime is exhibited in the 3 other study areas where a larger mean absolute separation is measured for slopes less than 0.3 degrees. This is in part explained by the presence of steeply sloping mountainous terrain in the Larsen-C and Ekström ice shelf study areas, and high rates of basal sheer in the Amundsen Sea Sector which result in evolution and steepening of the ice surface geometry (Payne et al., 2004; Joughin et al,. 2010). The influence of topographic and basal sheer controls on surface geometry is less significant in large central and western sectors of the Filchner-Ronne ice shelf study area, as shown by spatially extensive lower slope measurements inland of the grounding line (Figure 5-3a), providing additional evidence that a different slope regime is found in this study area. Furthermore, the Amundsen Sea Sector, Larsen-C ice shelf and Ekström ice shelf study areas show a very small difference between the minimum separation measured at the location of the 0.4, 0.5 and 0.6 degree slope boundary, with a separation of less than 5 km measured for all 3 slope values and a total range of 1.5 km. Given that the area of these three regions is significantly smaller than the Filchner-Ronne ice shelf study area, and that individually the slope regimes are similar with low root mean square variability at the optimum slope value, we combined the three study areas in order to pick the break in surface slope at a more widely applicable optimum value. The optimum slope value determined by a linear fit to each dataset is 0.2 degrees for the Filchner-Ronne ice shelf, and 0.5 degrees for all 3 other study areas (Figure 5-7).

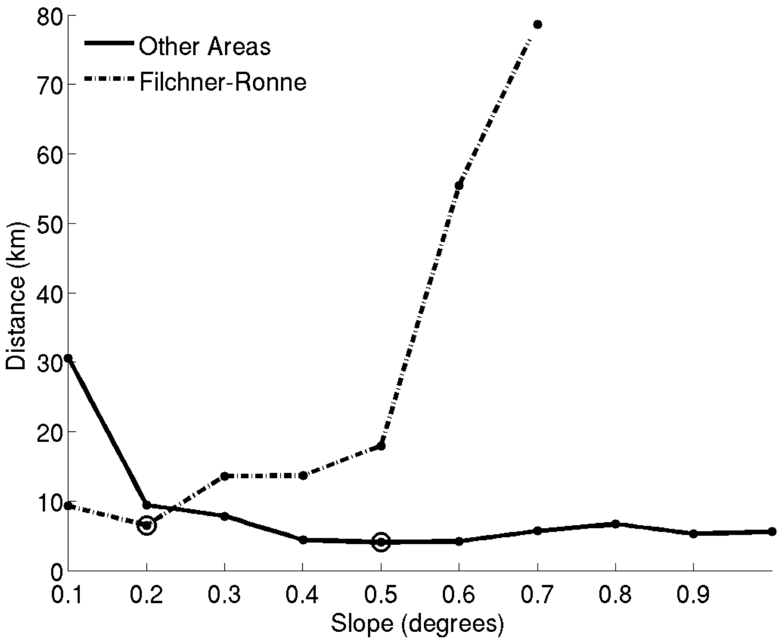

Figure 5-7. *Optimum slope values (large black circle) determined as the minimum mean absolute separation between the QDInSAR hinge line (Rignot et al., 2011) and the break in surface slope determined from CryoSat-2 altimetry. The Amundsen Sea Sector, Ekström ice shelf and Larsen-C ice shelf are grouped together (solid black line) whereas the Filchner-Ronne ice shelf which has a different slope regime is shown separately (dashed black line).*

5.6 Results and Discussion

We mapped the location of the break in surface slope, determined from slope values of 0.2 degrees at the Filchner Ronne ice shelf and as the 0.5 degrees elsewhere (Figure 5-8). Apart from a 55 km section of the Filchner-Ronne ice shelf, across the Foundation ice stream (-82.6 S, -60.3 W) where no CryoSat-2 SARIn data were acquired prior to 2013, the remaining 8,600 km of this boundary is continuous. We compared the CryoSat-2 break in surface slope to independent grounding line proxy datasets, including the QDInSAR hinge line (Rignot et al., 2011) and the shadow edge boundary (Bindschadler et al., 2011). The spatial separation between the CryoSat-2 break in surface slope and the QDInSAR hinge line (Figure 5-8) shows that on average for all four study areas, the mean absolute separation is 4.5 km, with differences of 6.5 km, 3.5 km, 4.5 km and 3.7 km in the Filchner-Ronne ice shelf, Ekström ice shelf, Amundsen Sea Sector and Larsen-C ice shelf respectively (Table 5-2). The regional mean separation between the CryoSat-2 break in surface slope and shadow edge boundary is even smaller, at 3.1 km, 2.6km 3.8 km and 3.0 km for the Ronne-Filchner ice shelf, Ekström ice shelf, Amundsen Sea Sector and Larsen-C ice shelf respectively. The overall mean difference between the CryoSat-2 break in surface slope and shadow edge boundary is 3.1 km, less than the difference between the two independent evaluation datasets (Table 5-2) which differ by 4.5 km on average for all 4 study areas.

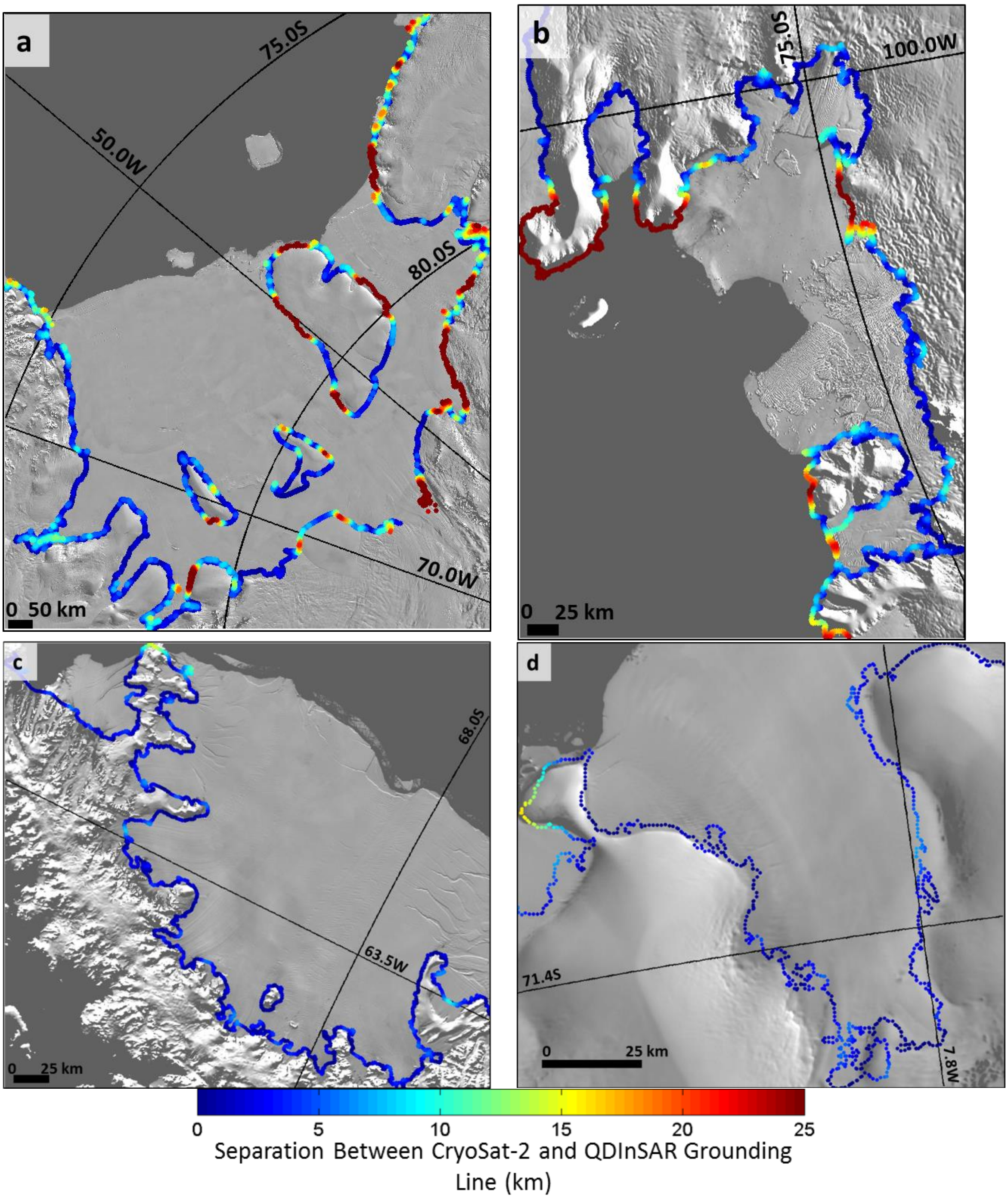

Figure 5-8. *CryoSat-2 break in surface slope in the Filchner-Ronne Ice Shelf (a), Amundsen Sea Sector (b), Larsen-C ice shelf (c) and Ekström Ice shelf (d) study areas, colour scaled to show mean absolute separation from the QDInSAR hinge line.*

A zoomed in view of the CryoSat-2 grounded ice boundary on the Filchner-Ronne ice shelf shows agreement between the break in surface slope and QDInSAR techniques across ice streams such as Carson Inlet, around isolated ice rises in the centre of the ice shelf, and across ice streams where no QDInSAR estimate exists (Figure 5-9).

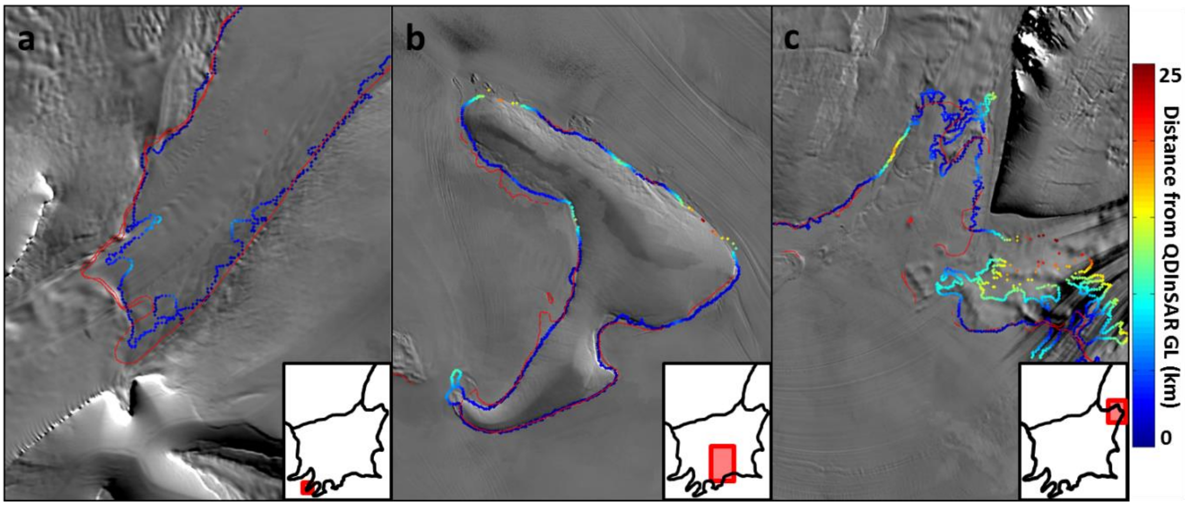

Figure 5-9. *Grounded ice boundary from the CryoSat-2 break in surface slope colour scaled to show mean absolute separation from the QDInSAR hinge line in three diverse areas of the Filchner-Ronne Ice Shelf including Carson Inlet (a), Henry Ice Rise (b), Baily and Slessor ice streams (c). The location of the QDInSAR grounding line is also shown (red) (Rignot et al., 2011).*

We evaluated the location of the CryoSat-2 break in surface slope against estimates of the grounding line position produced from independent satellite datasets and techniques. The QDInSAR hinge line is produced from ERS-1/2 and ALOS PALSAR SAR data acquired between 1992 and 2009 (Rignot et al., 2011), and the shadow edge boundary is produced from a combination of optical Landsat 7+ and laser altimetry ICESat data acquired between 1999 and 2009 (Fricker and Padman, 2006; Bindschadler et al., 2011). The CryoSat-2 data used in this study was acquired between 2010 and 2014, therefore neither of the available evaluation datasets are contemporaneous. This is an important consideration in areas of rapid grounding line retreat such as the Amundsen Sea Sector (Park et al., 2013) where grounding line retreat of up to 35 km, and maximum rates of 1.8 km per year, have been observed over the last 25 years (Rignot et al., 2014). It is important to note that while in the Amundsen Sea Sector some of the difference between the CryoSat-2 break in surface slope and the QDInSAR hinge line products can be attributed to change over time, this is unlikely to be true in other more stable regions such as the Ekström ice shelf where dynamic imbalance has not occurred. In these regions the separation between the CryoSat-2 break in surface slope and the evaluation datasets is more likely attributable to measurements inaccuracy. Overall, in all 4 study areas 82 % of the CryoSat-2 break in surface slope is separated by less than 10 km from the QDInSAR hinge line demonstrating the agreement between both techniques (Figure 5-10).

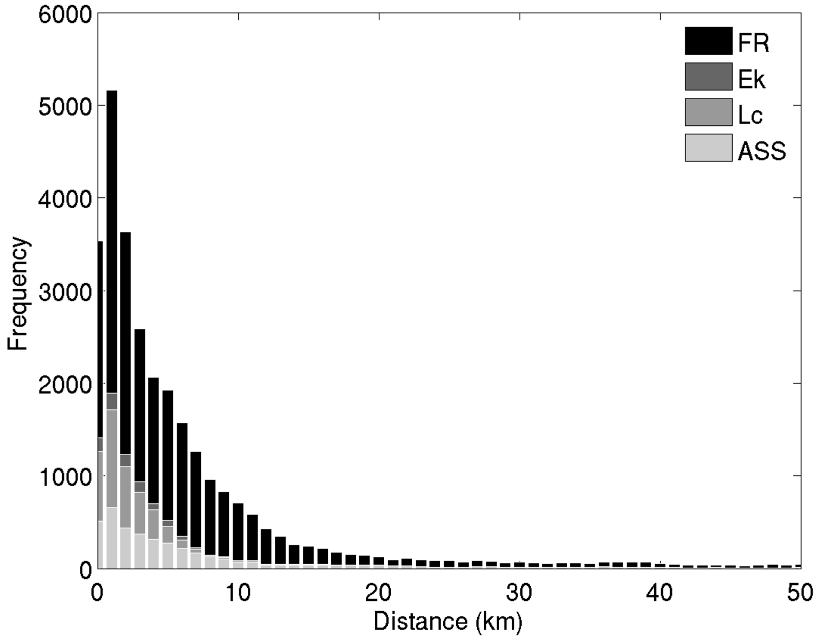

Figure 5-10. *Separation of the CryoSat-2 break in surface slope from the QDInSAR hinge line in all 4 study areas, where 82 % of the total dataset is separated by less than 10 km.*

Table 5-2. *Separation between estimates of grounding line position produced from the QDInSAR hinge line (Rignot et al., 2011), the shadow edge boundary (Bindschadler et al., 2011), and the CryoSat-2 break in surface slope, in all four study areas.*

	QDInSAR hinge line to CryoSat-2 break in surface slope		**QDInSAR hinge line to shadow edge boundary**	
Region	**Mean absolute separation (km)**	**Standard deviation of separation (km)**	**Mean absolute separation (km)**	**Standard deviation of separation (km)**
Filchner-Ronne	6.5	10.6	3.9	68.8
Ekström	3.5	7.2	5.8	10.2
Amundsen	4.5	7.1	6.2	12.5
Larsen-C	3.7	3.8	2.4	7.2

We evaluated the difference between the CryoSat-2 break in surface slope and the QDInSAR hinge line position in the Amundsen Sea sector in more detail as this is the only region where rapid grounding line retreat has been observed and a time series of QDInSAR hinge line measurements exist. The results show that across the main trunk of the Pine Island

Glacier in the Amundsen Sea Sector, West Antarctica, the break in surface slope is further inland than the QDInSAR hinge line produced in 2000, but corresponds well with the 2011 QDInSAR hinge line (Figure 5-11a) (Rignot et al., 2014). Thwaites Glacier is another region of known grounding line retreat and here the CryoSat-2 break in surface slope also more closely matches the spatial location and complex pattern of the 2011 QDInSAR hinge line (Rignot et al., 2014) compared to the 1996 QDInSAR hinge line position (Rignot et al., 2011) (Figure 5-11b). Smith Glacier is the most rapidly thinning ice stream in Antarctica, with surface lowering rates of up to 9 m per year measured since 2010 (McMillan et al., 2014). The CryoSat-2 break in surface slope shows ~19.1 km of inland retreat in comparison to the 1995 QDInSAR hinge line position, however this is ~12.3 km less than the 2011 QDInSAR hinge line position (Rignot et al., 2014) (Figure 5-11c). Despite the difference in inland retreat, the CryoSat-2 break in surface slope result shows that the zone of retreat extends an additional 25.6 km across Pope Glacier in the Amundsen Sea Sector, West Antarctica, a region that was unable to be mapped in 2011 due to lack of coherent SAR data. The CryoSat-2 break in surface slope shows that ~9.6 km of grounding line migration has occurred on Pope Glacier since the 1995, extending the zone of grounding line retreat to better match the observed region of surface lowering (McMillan et al., 2014).

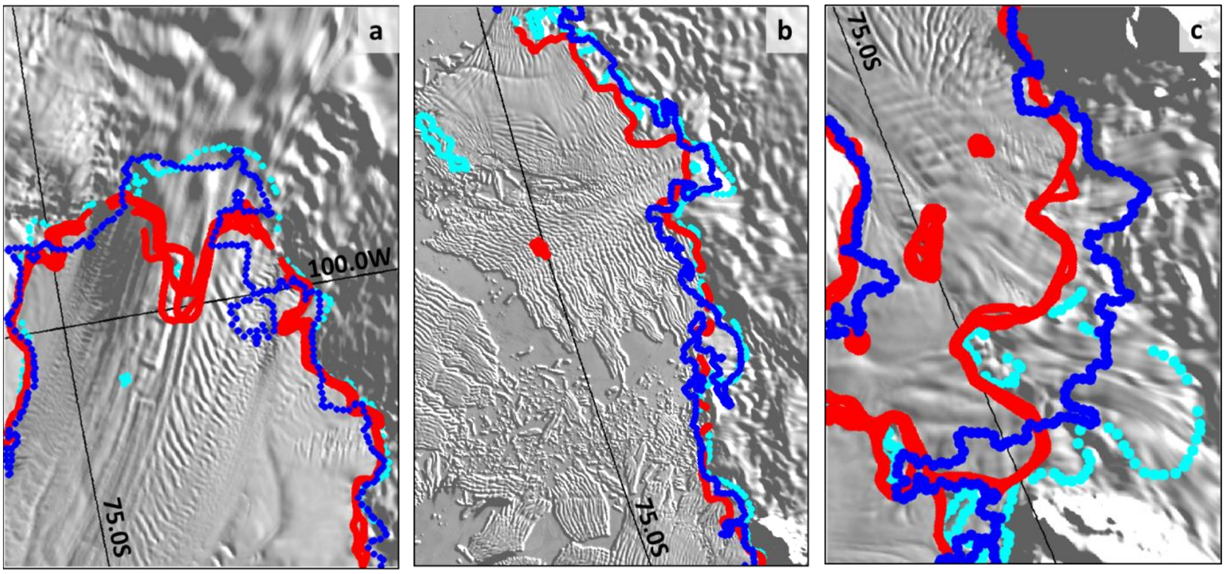

Figure 5-11. *CryoSat-2 break in surface slope (blue) on Pine Island Glacier (a), Thwaites Glacier (b) and Smith and Pope Glaciers (c) in the Amundsen Sea Sector, West Antarctica, shown alongside QDInSAR hinge line produced from SAR data acquired between 1992 and 2009 (red) and the 2011 (cyan) (Rignot et al., 2014).*

Our CryoSat-2 break in surface slope product provides a contemporary update to previous estimates of the grounding line position based on the QDInSAR hinge line and shadow edge boundary. These results provide a more recent assessment of the Antarctic ice sheet grounding line position compared with the most recent QDInSAR hinge line positions, measured in 2011 in the Amundsen Sea Sector (Park et al., 2013, Rignot et al., 2014), 2009 on the Filchner-Ronne ice shelf, 2000 on the Ekström ice shelf and 1996 on the Larsen-C ice shelf (Rignot et al., 2011). The CryoSat-2 break in surface slope confirms that in regions of sustained grounding line retreat, the present day break in surface slope is further inland than historical QDInSAR hinge line measurements, and furthermore it extends the region of contemporary retreat to encompass Pope Glacier which has thinned rapidly in the last 5 years (McMillan et al., 2014), an ice stream where the QDInSAR hinge line has not been mapped within the last 20 years. The spatial resolution and vertical accuracy of the QDInSAR technique is unprecedented, and when coherent SAR images are acquired they will serve as the primary hinge line measurement. However, over the last 25 years suitable data has not been acquired over the full Antarctic ice sheet, and outside of the Amundsen Sea Sector, observations of grounding line retreat are universally sparse.

We mapped the break in surface slope using a new independent technique which utilises CryoSat-2 radar altimetry data in four large, key study areas around the Antarctic ice sheet. The break in surface slope has previously been mapped using the shadow edge boundary as a proxy (Bindschadler et al., 2011); however, we provide the first assessment of using a direct measurement of the break in surface slope derived from geodetic surface elevation data as a proxy for the ice sheet grounding line. Historical radar altimeter missions such as ERS-1/2 and ENVISAT, and in the future Sentinel-3, combine to provide the most spatially wide, and temporally dense and continuous time series of ice sheet observations acquired by any instrument to date. In the future it will be possible to exploit the radar altimetry data archive to produce a 25 year long time series of the grounded ice boundary from the break in surface slope. This will provide an independent, complimentary means of detecting long term change in the grounded ice boundary location, both in regions of known instability such as West Antarctica, and in areas such as East Antarctica where SAR data required for the QDInSAR technique has not been acquired. CryoSat-2's novel SARIn imaging mode acquires spatially dense elevation measurements from which a relatively high resolution surface elevation map can be produced. The wider ~3 km track spacing of traditional pulse limited altimeters will limit the spatial resolution of a historical break in surface slope product; however, Digital Elevation Model's (DEM's) of geodetic surface heights could also be used to improve the spatial resolution. In the future it may be possible to directly compare cotemporaneous QDInSAR hinge lines with the break in surface slope, if the CryoSat-2 mission lifetime overlaps with Sentinel-1b when it will be possible to acquire short (6-day) repeat period SAR triplets suitable for interferometry.

5.7 Conclusions

We have measured the break in surface slope from CryoSat-2 radar altimetry data using an automated and computationally efficient plane fit solution. The dense spatial sampling of the CryoSat-2 Synthetic Aperture Radar Interferometric (SARIn) mode in the ice sheet margins (McMillan et al., 2014) has enabled a measurement of the break in surface slope to be produced every 1 km. Good agreement was found between the CryoSat-2 break in surface slope and the validation QDInSAR hinge line in all 4 study areas, with average separation of 6.5 km, 3.5 km, 4.5 km and 3.7 km on the Filchner-Ronne ice shelf, Ekström ice shelf, Amundsen Sea Sector and the Larsen-C ice shelf respectively. The separation between the CryoSat-2 break in surface slope and optical grounded ice boundary is even smaller at 3.1 km on average, and the mean absolute separation between the two independent evaluation datasets (4.5 km) indicates that the CryoSat-2 break in surface slope is of comparable accuracy to the existing datasets. In regions of rapid change such as the Amundsen Sea Sector, the CryoSat-2 break in surface slope more closely matches the published 2011 QDInSAR hinge line position in comparison to the historical position measured from data acquired 10 years earlier. This provides confidence that the CryoSat-2 break in surface slope correlates well with the present day QDInSAR hinge line location and can act as a complimentary new proxy measurement of the ice sheet grounding line. In the future this method could be extended to map the break in surface slope for the full Antarctic ice sheet from CryoSat-2. This new technique is automated, quick to run and objective therefore in the future when more data is acquired by CryoSat-2, it may also be possible to monitor change in the break in surface slope position using radar altimetry data.

Chapter 6

Discussion and Conclusions

6.1 Motivation

The aim of my thesis was to make new observations of ice sheet grounding lines using satellite Earth observation techniques. In the preceding chapters I have met this aim by measuring grounding lines using three techniques including quadruple difference interferometry (QDInSAR) (Chapter 3), differential range direction offset tracking (DRDOT) (Chapter 4) and the break in ice surface slope (Chapter 5). I developed methodology for two of the techniques (DRDOT and break in slope) within this thesis, and I have used the results to measure short term rates of grounding line migration for the first time, enabling an assessment to be made of the likely controlling processes (Chapter 3). In addition to this work on grounding lines I have also performed the first validation of an Arctic tide model (Chapter 3), and measured the seasonal ice velocity cycle on Petermann Glacier for the first time, linking this to observations of air temperature (Chapter 4). In this final chapter I will outline specifically how my thesis has met the original motivations for conducting the research, by providing a summary and synthesis of the work completed and the principal science results presented in each chapter. I also provide an overview of the key areas of future work that have been identified as a result of my thesis, and I will show how I have already begun to address some of these research questions.

6.1.1. Importance of Grounding Lines

The junction between the floating ice shelf and the grounded ice sheet is of critical importance because it delineates the lateral extent of the ice sheet margin and determines the optimum location of flux gates used for calculating ice discharge and hence ice mass balance. The position can fluctuate on short, sub-daily timescales due to the effects of ocean tides and localised ice thickness change (Chapter 3); however, regions of long term, annual to decadal, grounding line migration indicate the presence of sustained ice thickness change caused by dynamic instability (Rignot et al., 1998b; Park et al., 2013). Grounding line retreat leads to a reduction in the resistive force which restrains grounded ice and controls the rate of ice discharge. Ice sheet models and observations have shown that reduction or removal of this buttressing force can lead to rapid inland propagation of ice drawdown of marine based ice sheet sectors (Rignot et al., 2004; Joughin et al., 2010), illustrating how relatively modest changes at the termini of outlet glaciers can have a marked impact on the wider ice sheet mass imbalance. Measuring change in grounding line positions allows us to better understand the present day ice sheet contribution to sea level rise, and when ice sheet models accurately replicate the observed past change it provides improved confidence in their ability to predict the rate and magnitude of future dynamical imbalance (Favier et al., 2014).

6.1.2. Existing Techniques and Paucity of Data

A number of ground-based and Earth observation techniques have been used to map ice sheet grounding lines in Greenland and Antarctica. The ice sheet grounding line is located at the base of the ice sheet and, while it is theoretically possible to send an automatic submersible vehicle under the ice shelf to directly measure this location, in practice all existing in situ and remote observation techniques use ice surface features, such as the inland limit of tidal flexure (the hinge line) or the break in surface slope, as a proxy for grounding line position. A lack of suitable in situ and remote sensing data has meant that to date, the grounding line position has only been mapped at one epoch around the majority of the ice sheet coastline, precluding widespread observations of grounding line retreat (Figure 6-1). Three in situ methods have been used to measure ice sheet grounding line positions, including; measuring the vertical displacement caused by ocean tides using kinematic GPS (Vaughan, 1995) and tilt meters (Smith et al., 1991), and dating the historical ice sheet position using cosmogenic isotopes retrieved from seafloor sediments (Rebesco et al., 2014). Ground based observations of the grounding line position are extremely limited in both space and time due to the high cost and logistical difficulty of acquiring data over large areas. Consequently, techniques based upon satellite observations have emerged as an alternative solution, enabling relatively large quantities of data to be regularly acquired.

Three independent Earth observation techniques have been used to measure the grounding line position; namely shadow caused by the break in ice sheet surface slope in optical imagery (Bindschadler et al., 2011), and detection of tidal motion in quadruple difference interferometric synthetic aperture radar (QDInSAR) observations (Rignot et al., 1998a) and in repeat satellite altimeter measurements (Fricker and Padman, 2006) (Figure 6-1). However, only one technique - quadruple difference interferometry (QDInSAR) - has been demonstrated to be capable of measuring change in grounding line location. QDInSAR has been used to measure the only documented secular grounding line migration, in the Amundsen Sea Sector in West Antarctica (Figure 6-1) which, over the last 19 years, has exceeded 1 km per year on Pine Island and Smith Glaciers (Park et al., 2013; Rignot et al., 2014). It has not been possible to make widespread measurements of the grounding line retreat rates elsewhere on the Greenland and Antarctic ice sheets, because of the poor spatial and temporal coverage of Synthetic Aperture Radar (SAR) image triplets with a sufficiently short temporal baseline (days) to maintain phase coherence on fast flowing ice streams. Consequently, new techniques are required to fully exploit the satellite data archives, and to improve the temporal and spatial coverage of grounding line measurements. In this thesis I have processed previously unexamined historical datasets to provide the first quantitative assessment of how large short term changes in grounding line position can be, I have identified and assessed the processes driving these change, and I have developed, validated and applied two new methods for locating ice sheet grounding lines using incoherent SAR data and CryoSat-2 radar altimetry data.

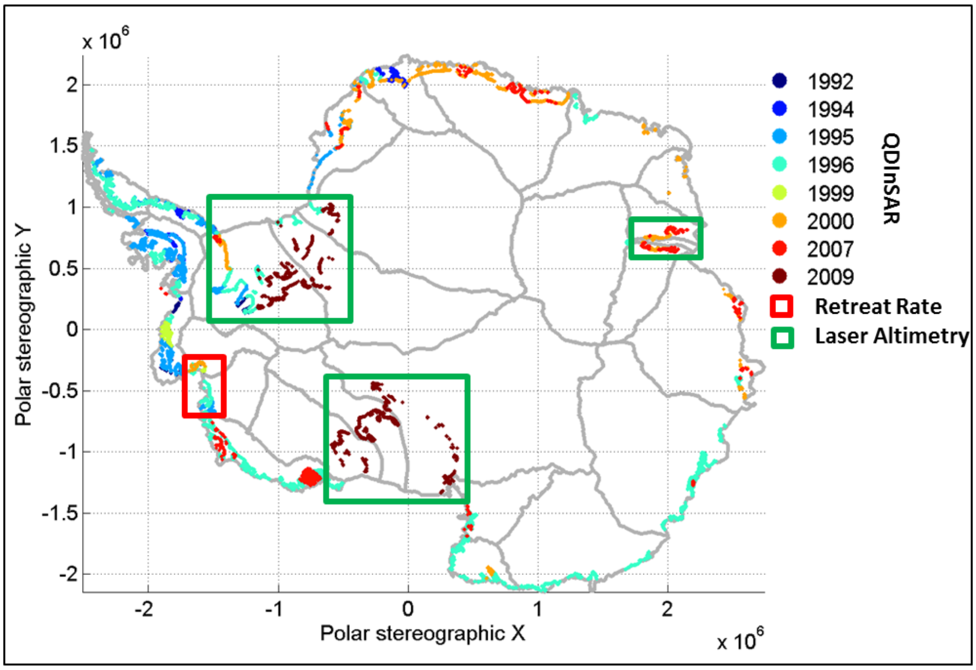

Figure 6-1. *Map of known grounding line positions around the Antarctic ice sheet, measured by different techniques including QDInSAR (multiple coloured lines by date) (Rignot et al., 2011), repeat track altimetry (green squares), and identification of the only area where retreat rates have been measured (red box). The ASAID optical shadow grounding line (Bindschadler et al., 2011) is present around the whole Antarctic coastline and is therefore not displayed for clarity.*

6.2 Summary of Principal Findings

Key Science Result 1: Lateral precision of a QDInSAR grounding line position estimated to be 25 m.

I quantified the error on QDInSAR measurements of the grounding line position by translating noise in the vertical displacement profiles into a lateral error in the grounding line position. Profiles of vertical displacement were retrieved from 17 quadruple difference interferograms along a transect oriented in a stream wise direction, perpendicular to the Petermann Glacier grounding zone (Chapter 3, Figure 3-1). A running mean of the vertical displacement was measured along each transect (Figure 6-2.a), with the residuals computed as the difference of each point along the profile from the local mean (Figure 6-2.b). All 17 profiles exhibited extremely low variability with a mean absolute difference of 0.4 ± 0.2 cm, and a larger total range of 6.5 cm. The range of the residuals measured along each profile is comparable on both grounded and floating ice, indicating that the error is independent of tide amplitude. This suggests that the error is systematic rather than geophysical in origin, and that it may reasonably be used as a formal error budget associated with QDInSAR grounding line measurements made in other areas. I retrieved the standard deviation of the residuals from the mean at the grounding line of each displacement profile, and then translated this into the lateral error in grounding line position by measuring the distance seaward of the grounding line over which the mean vertical displacement was within the range of error. The mean lateral precision of a QDInSAR grounding line position is 25 m with a total range of up to 0.1 km. This method of estimating the lateral precision of the QDInSAR technique results in a precision less than the 30 m pixel size of the input SAR data; however, it does not account for errors in the manual delineation of the grounding line which cannot have been completed at sub-pixel accuracy. Despite these limitations the method is used as it is a quantitative and repeatable estimate of the noise on the processed output data, which can be used to compare the quality of QDInSAR results against each other and different techniques. The error on the QDInSAR grounding line position is 22 % of the mean short term grounding line variability (0.45 km), providing confirmation that the observed change is not large enough to be accounted for by measurement error.

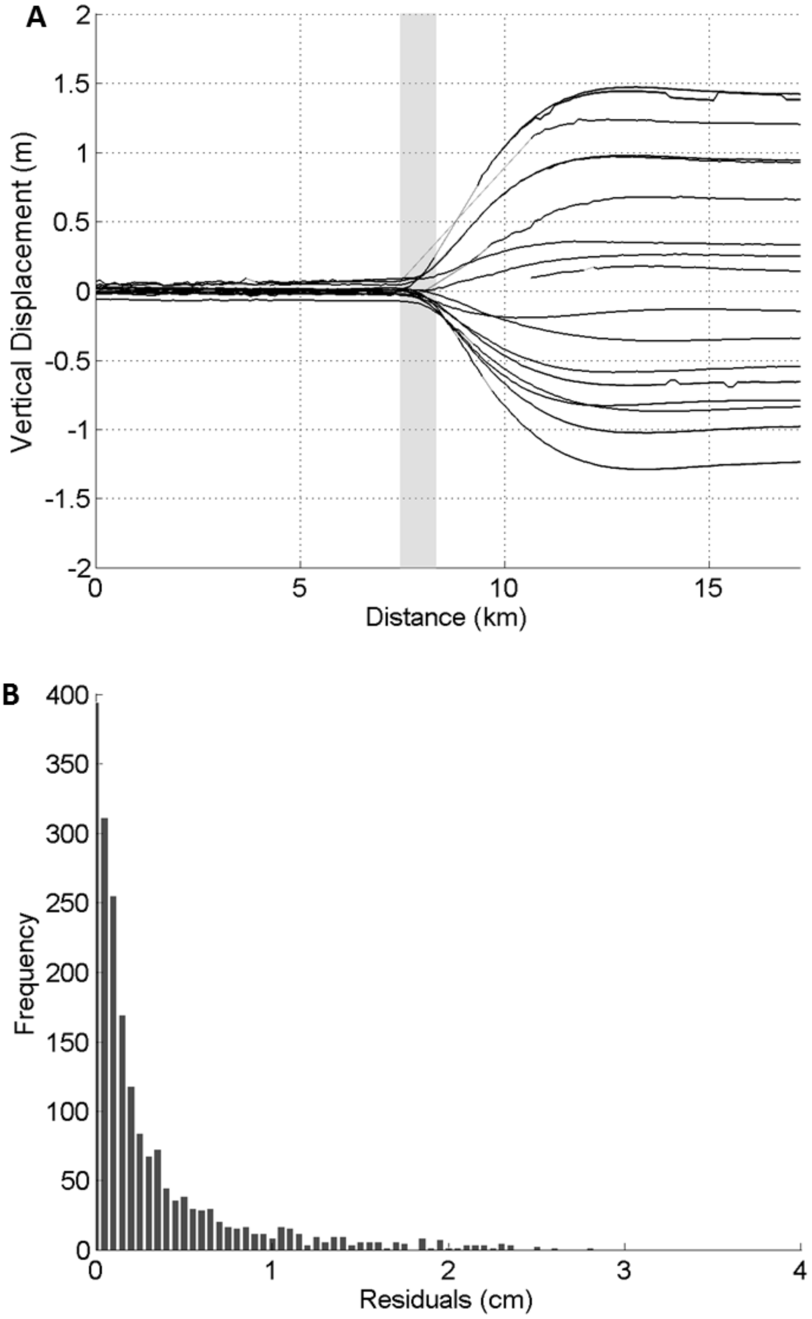

Figure 6-2. *(a) Profiles of vertical displacement retrieved from 17 unwrapped quadruple difference interferograms on Transect 1 (Chapter 3, Figure 3-1), which is oriented in a stream wise direction perpendicular to the Petermann Glacier grounding zone. The running mean (black line), standard deviation from the mean (dark grey shaded area) and minimum and maximum QDInSAR grounding line positions (light grey shaded area) are all annotated. (b) Histogram of the residuals measured as the difference from the mean of each point along the 17 QDInSAR vertical displacement profiles.*

Key Science Result 2: 19 Year Time Series of QDInSAR shows 0.5 km of short term variability in the grounding line position at Petermann Glacier.

In Chapter 3 I presented the most dense time series of grounding line positions measured on any single ice stream on the Greenland or Antarctic ice sheets to date. The 19 year time series of quadruple difference interferograms showed that while there was 0.5 km of variability in the grounding line position on Petermann Glacier, this is not attributed to long term retreat. The result provides evidence that, unlike many ice streams on the South-West Coast of Greenland, prior to 2011 Petermann Glacier, on the North-West coast, did not exhibit dynamic instability and increased rates of ice mass loss over time. No previous assessments of the short term change in grounding line position have been published due to a lack of observational evidence. I performed a critical evaluation of the 19 year QDInSAR time series to show that, on Petermann glacier, 34 % of the observed grounding line variability was caused by short term tidal motion, and that the residual de-tided grounding line variability was accounted for by less than 2.2 m of localised ice thickness change. The results showed that while QDInSAR can accurately measure vertical displacement to within 3.7 cm, the lateral variation in grounding line position at Petermann Glacier is significantly larger and cannot be unequivocally interpreted as dynamical retreat unless the change in position is greater than 1.3 km. Other ice streams with different bedrock geometry may experience even larger short term grounding line variability. Therefore in the future more spatially extensive and temporally dense measurements of grounding line position must be made to quantify the magnitude of short and long term change, which will enable a better understanding of the physical processes controlling grounding line migration.

Key Science Result 3: Lateral accuracy of a differential range direction offset tracking grounding line position is 0.8 km.

I quantified the accuracy of the DRDOT measurements of the grounding line position by translating noise in the profiles of vertical displacement into the equivalent lateral variability in grounding line position. Profiles of vertical displacement were retrieved from four differential range direction tracking images along a transect oriented in a stream wise direction, perpendicular to the Petermann Glacier grounding zone (Chapter 4, Figure 4-2). The running mean of the vertical displacement was calculated along each transect (Figure 6-3 a), and then the residuals were computed as the difference of each point along the profile from the mean (Figure 6-3 b). The mean absolute difference measured on all 4 profiles was 4.9 cm with a standard deviation of 2.0 cm, and a total range of 57 cm. The noise range on the DRDOT vertical displacement profiles is more than 8 times greater than the noise range on the QDInSAR vertical displacement confirming the much greater vertical precision of the phase sensitive interferometric techniques. The range of the residuals measured along each profile is comparable on both grounded and floating ice, indicating that the error is independent of tide amplitude. This suggests that the error is systematic rather than geophysical in origin, and that it can reasonably be used as a formal error budget associated with DRDOT grounding line measurements made in other areas. I retrieved the standard deviation of the residuals of the mean at the grounding line position on each of the four transects, and then translated this into lateral error in the grounding line position by measuring the distance seaward of the grounding line over which the mean vertical displacement was within the range of error. This shows that the mean lateral accuracy of a DRDOT grounding line position is 0.8 ± 1.0 km with a total range of up to 2.1 km, which is 163 % of the mean grounding line separation (0.5 km) from this new technique. While the DRDOT technique provides a valuable opportunity to make more frequent measurements of grounding line position due to the techniques lack of dependence on phase coherence, more care must be taken when interpreting the results, and when suitable data is acquired, QDInSAR measurements of the grounding line position should be used to complement this new technique.

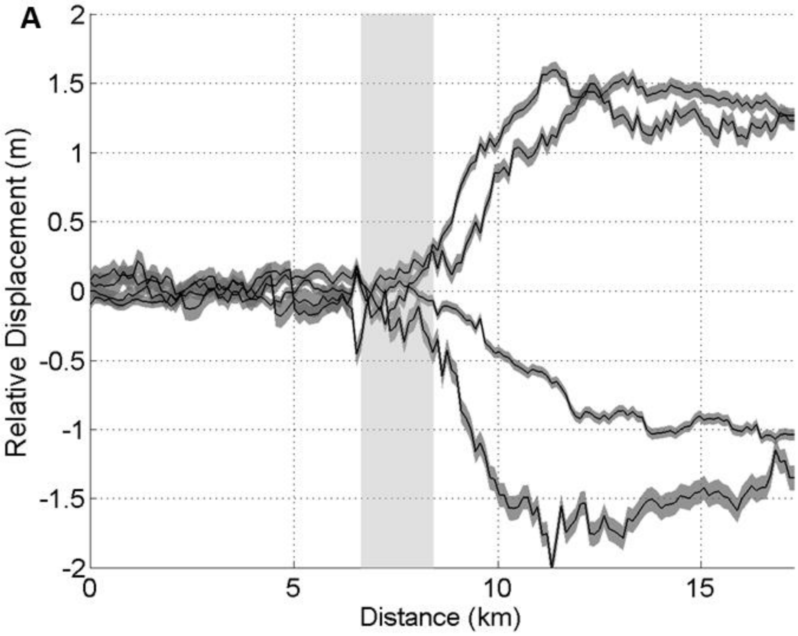

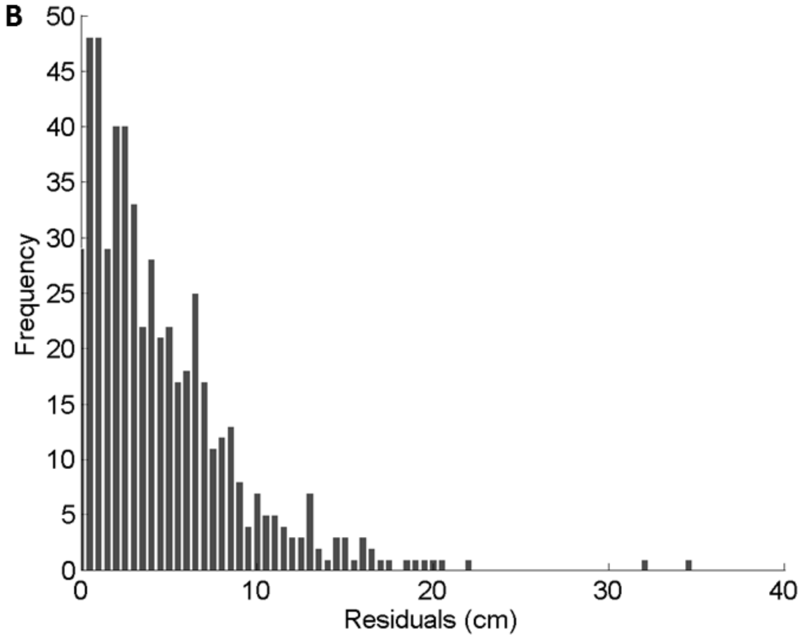

Figure 6-3. *(a) Profiles of vertical displacement retrieved from 4 Differential Range Direction Offset Tracking (DRDOT) images on Transect 1 (Chapter 4, Figure 4-2), which is oriented in a stream wise direction perpendicular to the Petermann Glacier grounding zone. The running mean (black line), standard deviation from the mean (dark grey shaded area) and minimum and maximum DRDOT grounding line positions (light grey shaded area) are all annotated. (b) Histogram of the residuals measured as the difference from the mean of each point along the DRDOT vertical displacement profiles.*

Key Science Result 4: Differential range direction offset tracking can be used to measure the grounding line position in incoherent TerraSAR-X data.

In Chapter 4 I developed and applied a novel method for determining the grounding line location using a time series of incoherent differential range direction offset tracking measurements. The offsets recorded low levels of vertical displacement on the grounded ice sheet inland of the grounding line, with larger vertical displacement on the floating ice shelf (~ ± 1.5 m) which is the same order of magnitude as the estimated differential tides simulated by the AODTM-5 Arctic ocean tide model. I used this technique to measure the location of the Petermann Glacier grounding line location on four separate occasions during a four month period, creating the third most populous time series of grounding line position to date (Chapter 3). An assessment of the modelled differential tide suggests that for the DRDOT technique to be successful, the floating ice shelf must be displaced by a differential tide greater or less than 0.5 m. I measured the separation of the DRDOT grounding line from the grounding line measured using QDInSAR (Chapter 3) and found good agreement between both datasets, with the location and relative shape of the line across the ice stream broadly repeated. This intercomparison showed that the mean separation of the differential range direction offset tracking grounding lines was 0.8 km from the 1995 QDInSAR position, an overall difference that is 56 % greater than the variability of grounding lines measured on the same ice stream using the QDInSAR technique. The 0.8 km lateral accuracy of the DRDOT technique suggests that a significant portion of the grounding line temporal variability observed may be attributable to measurement error, rather than real change in grounding line position. The DRDOT results provide independent confirmation that, prior to 2011, no significant grounding line retreat has occurred on Petermann Glacier since 1992.

Key Science Result 5: The break in ice surface slope can be mapped with CryoSat-2 SARIn mode at a spatial resolution of 1.0 km.

The results in Chapter 5 demonstrate that the grounded ice sheet boundary can be mapped by using the break in ice surface slope, detected with altimetry, as a proxy for the grounding line position. I developed a technique which used a robust plane fit solution to produce a reliable measurement of the geodetic ice surface slope from CryoSat-2 radar altimetry data, taking advantage of the dense spatial sampling achieved by the Synthetic Aperture Radar Interferometry (SARIn) acquisition mode which is operated over the ice sheet margins. While previous studies have used topographic shadow, caused by the break in ice sheet surface slope, as a proxy for grounding line position (Bindschadler et al., 2011), I demonstrated that the break in surface slope between the floating ice shelf and the grounded ice sheet can be detected with CS2 altimetry, and that it also corresponds to the known grounding line position measured using QDInSAR (Rignot et al., 2011). This provides observational evidence supporting the use of the break in slope, or proxies of the break in slope such as shadow, as an indicator of the grounding line position. This new technique is automated and computationally efficient which in the future will allow the break in ice surface slope to be rapidly and repeatedly mapped over the full ice sheet area every 1 km, as determined by the grid cell size.

Key Science Result 6: The CryoSat-2 break in slope technique matches the QDInSAR grounding line to within 4.5 km.

In Chapter 5 I presented the results of grounding line measurements made from CryoSat-2 in four regions of Antarctica; the Filchner-Ronne, Ekström and Larsen-C Ice Shelves, and throughout the Amundsen Sea Sector. I evaluated the quality of the CryoSat-2 grounding line position by computing the separation of the CryoSat-2 grounding line from the QDInSAR position, and found mean values of 6.5 km, 3.5 km, 4.5 km and 3.7 km respectively, for all four study areas. The mean separation of the CryoSat-2 break in slope product in all four study areas is 0.1 km lower than the total 4.5 km mean absolute separation of the optical shadow grounding line products, relative to the same QDInSAR dataset, indicating that the new CryoSat-2 product is of comparable accuracy to existing datasets. In some places, the CryoSat-2 product provides the first measurement of the grounded ice boundary for over 20 years.

The CryoSat-2 method can be used as a complimentary tool to the existing methods of measuring the grounding line. In the future, when a larger volume of CryoSat-2 data has been acquired, it will be possible to investigate if this technique can be used to detect change in grounding line positions over time. The dense spatial sampling achieved by the CryoSat-2 SARIn mode over the ice sheet margins enables a grounded ice boundary product to be produced at 1 km spatial resolution. While this offers a clear improvement over what would be possible using the 3 km footprint size of traditional pulse limited altimeters, in the future this technique could be adapted to produce a grounded ice boundary product from a long time series of multi mission altimetry data including ERS-1/2 and Sentinel-3. Unlike the QDInSAR and DRDOT methods, I did not produce a formal error estimate for the CryoSat-2 break in slope technique because the error on the slope measurement does not directly translate into lateral error in the grounding line position. In the future further research should be conducted to better characterise the relationship between the break in slope and the grounding line position to better understand the likely error.

Key Science Results 7: The CryoSat-2 break in slope technique provided the first grounding line measurement on Pope Glacier for 20 years, extending the zone of known retreat by 9.6 km .

The CryoSat-2 results presented in Chapter 5 showed that, in the Amundsen Sea Sector of West Antarctica, where the most rapid rates of grounding line retreat have been observed (Park et al., 2013; Rignot et al., 2014), the zone of grounding line retreat on Pope Glacier can be extended by ~ 9.6 km across the main ice stream. This is an area where rapid surface elevation change has been observed (McMillan et al., 2014); however, previous SAR acquisitions were not coherent and therefore it was not possible to measure the grounding line location using QDInSAR.

Key Science Result 8: AODTM-5 Arctic Tide Model predicts both the phase and amplitude of the ocean tides with a root mean square difference of 21 cm.

The results presented in Chapter 3 provide the first validation of an Arctic tide model using ice shelf vertical displacement measured by quadruple difference interferometry (QDInSAR) from data acquired by the European Remote Sensing (ERS)-1 and -2 satellites over a 19-year period. I found that within the Petermann Glacier fjord, although the AODTM-5 tide model predicted a large 1.7 m range of differential tide amplitudes, the spatial variability of the tide amplitude along the fjord at any one epoch was less than 1 cm. An intercomparison of differential tide amplitudes retrieved from the AODTM-5 tide model and unwrapped vertical displacement from quadruple difference interferograms (QDInSAR) showed that both datasets agree with a root mean square difference of 20.6 cm, indicating that in this area the tide model accurately estimates both the phase and amplitude of the observed ocean tides. In the future, as new SAR satellite systems such as the Sentinel-1a and b satellite constellation acquire data more regularly over Greenland and the larger Antarctic ice shelves, this study could be repeated to validate the spatial variability of ocean tide amplitude and phase predicted by both Northern and Southern hemisphere tide models.

Key Science Result 9: Seasonal ice speed up on Petermann Glacier is 21 % of the slower flowing, autumn mean.

In Chapter 4 I presented the results of a study investigating the ice velocity variations on Petermann Glacier using TerraSAR-X data acquired during the summer of 2009. I showed that throughout the 4 month study period, maximum ice velocities of up to 1.4 km per year were measured on the floating ice shelf 15 km seaward of the grounding line, and that this was 50 % more than the minimum ice velocity measured on the grounded ice stream, 20 km inland of the grounding line. I used this dataset to measure the seasonal ice velocity cycle on Petermann Glacier for the first time, which showed that over the whole study area a mean ice velocity speed up of 17 ± 4 % was measured at the summer peak, which in 2009 fell between the 15th and 26th of July. Furthermore, although air temperatures were not collected on Petermann glacier during the 2009 summer, air temperatures measured at an in situ automatic weather station on the Petermann Glacier ice shelf between 2002 and 2005 showed that the timing of the seasonal ice velocity speed up corresponds to the approximate middle of the positive day period of the typical summer season, suggesting that on Petermann Glacier the seasonal ice velocity cycle may be driven by surface melt, as postulated by previous modelling studies (Nick et al., 2012). The size of the seasonal cycle on Petermann Glacier is smaller than estimates of the seasonal speed up (> 50 %) on ice streams in the South West of Greenland (Joughin et al., 2008). This may be in part due to the shorter summer melt period in the North relative to the South of Greenland. Recent observations of seasonal ice velocity on Jakobshavn Isbrae showed that large inter-annual variations in the size of the summer speed up can occur, with peak summer speeds in 2012 recorded as being 30 to 50 % greater than in previous years (Joughin et al., 2014). This supports the need for continued and regular monitoring of ice velocity on all major ice streams in Antarctica and Greenland in order to develop a better understanding of the environmental forcing mechanisms controlling change.

6.3 A Combined Approach to Mapping Ice Sheet Grounding Lines

The results presented in this thesis have shown that it is possible to monitor ice sheet grounding lines more frequently than has been possible using the conventional approach of QDInSAR alone and that, additionally, new grounding lines can be detected by utilising previously unexploited satellite data. The three techniques considered in this thesis - QDInSAR, DRDOT, and break in surface slope - are complimentary, and in the future could be applied to data acquired over different study areas to provide new, updated measurements of the ice sheet grounding line position (Table 6-1).

Table 6-1. *Summary table of the techniques, satellite missions, study periods and areas, accuracy and spatial resolution of the derived grounding lines*

Technique	Satellite	Study Period	Study Area	Accuracy	Spatial Resolution
QDInSAR	ERS-1/2	1992 -2011	Petermann Glacier, NW Greenland	25.8 m	30 m
DRDOT	TerraSAR-X	June - October 2009	Petermann Glacier, NW Greenland	0.8 km	100 m
Break in Slope	CryoSat-2	2010 - 2014	Amundsen Sea Sector, Larsen-C, Filchner-Ronne, Ekström ice shelf	-	1 km

It is important to make present day measurements of the grounding line position around the full Greenland and Antarctic coastline because widespread and sustained ice speedup (Moon et al, 2012, Mouginot et al., 2014) and ice thinning on both the grounded ice sheet (Pritchard et al., 2009; Helm et al., 2014; McMillan et al, 2014) and floating ice shelves (Shepherd et al., 2010; Paolo et al., 2015) has been observed over the last 25 years, and may be associated with previously undetected regions of long term grounding line retreat. In some areas such as the Amundsen Sea Sector in West Antarctica, a large amount of satellite data has been regularly acquired allowing the dynamic instability and grounding line retreat to be detected using QDInSAR (Figure 6-1) (Park et al., 2013; Rignot et al., 2014). Nevertheless, even in this most frequently observed regions, a continuous present day grounding line is not available over the whole study area, for example, a loss of phase coherence has prevented the QDInSAR technique being successfully applied on Pope Glacier and therefore an updated grounding line position had not been measured since 1995 (Rignot et al., 2014). However, by utilising previously unexploited CryoSat-2 data to measure the break in surface slope, it was possible to reproduce the more recent 2011 grounding line position in areas where coherent SAR data did exist. This has extended the known region of grounding line retreat by 9.6 km over earlier QDInSAR estimates thus providing an updated assessment of the grounding line position. The same was true for other regions such as the Larsen-C ice shelf where an absence of coherent SAR data prevented a reassessment of the present day grounding line position using the QDInSAR technique within the last 20 years. However, utilising the CryoSat-2 break in slope technique enabled a present day measurement to be made (Chapter 5).

Present day grounding line measurements are also required to detect newly evolved regions of dynamic instability with greater confidence. Around the Antarctic coastline there are a number of regions where sustained ice thinning at rates of over 2 m per year has been observed during the last 5 years, for example Fleming Glacier on the Antarctic Peninsula, Totten Glacier in East Antarctica, and a number of tributary Glaciers feeding into the Eastern Getz ice shelf (McMillan et al., 2014). Some of this ice mass loss signal may be metrological in origin and therefore not driven by dynamic instability; however, the 20 % error on even the most sophisticated surface mass balance models (Van Wessem et al., 2014) can make it particularly challenging to attribute the signal to a dynamic or meteorological origin. The English Coast on the Antarctic Peninsula has been recently identified as new region of dynamic instability (Wouters et al., 2015); however, temporally coincident measurements of ice velocity speed up and grounding line retreat are lacking. In the future, a combined multi-technique approach should be used to increase the spatial and temporal density of grounding line measurements which would enable regions of dynamic instability to be identified with greater confidence.

The large number of QDInSAR grounding line measurements on Petermann Glacier (Chapter 3) revealed that the magnitude of short term grounding line variability, on an otherwise stable grounding line which has shown no long term retreat, is 1.3 km. There have been no previous observations of short term change in grounding line position so it is not known if variability of this magnitude is representative of other major ice streams. However, in the absence of other observations, there are no major extenuating factors that suggest the observations on Petermann Glacier are extreme. This indicates that it could serve as a useful guide for the likely short term grounding line variability experienced on other marine terminating ice streams. The magnitude of tidally-induced grounding line displacement depends primarily on the bedrock slope and on the tidal range, which in the case of the Petermann Glacier, the AODTM-5 tide model predicts is ~2.1 m (Chapter 4) (Padman and Erofeeva, 2004). This is within the average 1 to 2 m range of tide amplitudes estimated around the Antarctic coastline using the CATS2008 tide model (Padman et al., 2002). In other areas such as the Filchner-Ronne and Larsen ice shelves in the Weddell Sea, a large > 3 m tide range is predicted; this is over ~ 33 % more than that observed on Petermann Glacier. This indicates that on some ice streams, tidally induced grounding line migration may be even larger than that observed on Petermann Glacier, suggesting that the magnitude of the observed short term migration may be a lower bound rather than an upper limit (Chapter 3). Another significant controlling factor that influences the rate and magnitude of both short and long term grounding line migration is bedrock geometry. Two airborne measurements acquired by a deep ice penetrating radar across the Petermann Glacier grounding line showed that the bedrock topography has a relatively low inclination (-0.11 % and 0.42 %) in comparison to other ice streams such as Pine Island Glacier (1.1 %; Rignot et al., 1998b). While steeply sloping bedrock that also increases in elevation inland of the grounding line is not likely to facilitate large rates of migration, a steeply-sloping retrograde bedrock topography is inherently unstable and is conducive to much larger grounding line position variability. The relatively flat bedrock topography on Petermann Glacier indicates that the topographic setting is unlikely to cause either extremely large or small grounding line migration, providing further support that the short term variability observed on Petermann Glacier may be indicative of the likely range on other ice streams in Antarctica and Greenland. Without more widespread observations of short term grounding line retreat, it is not possible to ascertain with greater certainty whether or not this hypothesis is correct. However, if we make this assumption, the observed short term grounding line migration (810 m) is 42 % of the annual retreat rate (1.8 km) on the world's most rapidly retreating grounding line on the Smith/Kohler ice streams (Rignot et al., 2014). This would suggest that in order to measure long term dynamically induced grounding line retreat with confidence, measurements would have to be made over a time period greater than a year for the retreat signal to be significant enough to be detected outside of the range of short term variability, unless a smaller range of short term variability has been rigorously characterised for the specific ice stream. In the future, by utilising the strengths and weaknesses of multiple measurements techniques, such as those demonstrated in this thesis, it will be possible to monitor ice sheet grounding line positions with greater frequency which will continue to improve our understanding of the range of short and long term rates of grounding line migration.

6.4 Ideas for Future Work

6.4.1. Application of QDInSAR to ERS-1/2 Archive to Map Antarctic and Greenland Grounding Lines Between 1992 and 2011

The ERS-1 and -2, 1-3-day repeat periods which took place in 1992, 1995/6 and 2011, have provided the majority of the interferometrically viable datasets used to measure the grounding line using QDInSAR. On Petermann Glacier I demonstrated that it was possible to measure the grounding line 17 times using QDInSAR from this historical dataset which was a significant improvement on the previously published single grounding line measurement (Rignot et al., 1998a). It is possible that there are many other ice streams in Greenland and Antarctica where a large volume of currently unexploited coherent SAR data exists. In the future, processing and analysis of this data would increase the number of grounding line measurements available. This would provide new information on the magnitude of short term grounding line migration on a larger number of ice streams, and may help identify previously unknown regions of long term retreat and ice instability. Given the high resolution of the QDINSAR technique, which has a small lateral error of only 25.3 m, even very small changes in grounding line position should be measurable. One of the challenges that may limit the extent to which this new work can be carried out, is that in order for an accurate QDInSAR measurement to be made, the topographic phase signal must be removed using an auxiliary digital elevation model. The number of accurate digital elevation models is limited in time, and therefore in regions which have experienced large rates of surface elevation change, it may not always be possible to accurately remove all of the topographic phase signal. Inaccuracies in the topographic phase signal removal will result in either too many or too few phase cycles, or ‘fringes’, being removed from the interferogram which in the worst case could result in a misinterpretation of the differential interferogram and therefore the delineation of the grounding line. Despite these potential issues, as long as a rigorous evaluation of the results is conducted, it is likely that there is still a large amount of scientifically pertinent information on grounding lines that can be gained from the ERS data archives.

6.4.2. Application of QDInSAR and DRDOT to TerraSAR-X Archive to Map Antarctic and Greenland Grounding Lines Between 2007 and 2015

Since 2007, TerraSAR-X has acquired valuable data over a large number of Greenland and Antarctic ice streams, including areas such as East Antarctica which are relatively unexplored in comparison to the more frequently observed West Antarctica and the Antarctic Peninsula. In the future, the DRDOT technique developed in this thesis could be applied to all ice streams where sufficient data has been acquired which would provide new measurements of the grounding line position that are not already available. However, the major limiting factor in this next step is data access, as the archive of TerraSAR-X satellite data is not freely and openly available. It has also been demonstrated that the lateral precision of the DRDOT technique (0.8 km) is poorer than the highly precise phase sensitive QDInSAR technique (25.3 m), which limits the extent to which low amplitude tidal displacements, and therefore the grounding lines, can be measured. A future study should be conducted to investigate if the lateral precision of the DRDOT technique could be improved using TerraSAR-X spotlight mode data. Although limited in spatial extent by the smaller frame size, spotlight mode data is acquired with a 300 MHz bandwidth which translates into a much finer range resolution which should be capable of measuring displacements in the line of sight of over 0.5 m. This is a 50% improvement on the range resolution of strip map mode TerraSAR-X data which has the potential to significantly improve the accuracy of the DRDOT technique.

6.4.3. Application of Slope Break Method to CryoSat-2 Archive to Map Antarctic and Greenland Grounding Lines Between 2010 and 2015

Over the last 5 years CryoSat-2 data has been acquired over the full Antarctic and Greenland ice sheet and provide sufficient data density in the ice sheet margins to produce a robust plane fit solution of the surface topography from which the surface slope can be derived. As the CryoSat-2 break in slope technique developed in this thesis is largely automated and computationally efficient to run, extending and applying this technique to map grounding line positions across the full ice sheet area is possible. The major challenge that is likely to be encountered when expanding this study is reconciling the regionally specific slope thresholds from which the current grounding line results have been obtained, with the need for a continuous grounding line around that whole ice sheet coastline. A significant amount of work would also be involved in validating an extended CryoSat-2 break in slope grounding line around the whole ice sheet margin, and this would be particularly challenging in parts of Eastern Antarctica and the Trans Antarctic mountains where QDInSAR grounding line measurements are not always present.

6.4.4. First Application of QDInSAR to Sentinel-1 Archive and Future Data to Map Antarctic and Greenland Grounding Lines from 2014 Onwards

Temporal decorrelation of SAR data over ice covered terrain has been a major prohibitive factor preventing widespread application of interferometric processing techniques to data acquired by historical SAR sensors over ice covered terrain. New SAR sensors operated with shorter (< 35 day) repeat periods offer an exciting new prospect for producing contemporary QDInSAR measurements of the grounding line position. Sentinel-1a, launched in April 2014 into a polar sun synchronous orbit, is revolutionising the spatial coverage and temporal frequency with which multiple glaciological parameters can be measured, including ice speed, calving front location, sea ice coverage and motion, and grounding lines. Sentinel-1a is a C-band SAR satellite which is operated in a short 12-day repeat orbit, with a large swath width that enables data to be regularly acquired over the full ice sheet area at latitudes less than 82° North or South. The 12-day repeat period will be further reduced to 6-days after the launch of Sentinel-1b, which is currently scheduled for 2016. Over the Greenland and Antarctic ice sheets Sentinel-1a data is primarily acquired in Interferometric Wide (IW) swath mode, which has a large 250 km swath width because it is operated in a Terrain Observation with Progressive Scans in azimuth (TOPS) mode. This acquisition mode is a significant departure from the traditional ScanSAR acquisition mode utilised by SAR missions such as ERS-1/2 which had a significantly smaller 100 km swath width.

The advantage of Sentinel-1a is large scale frequent coverage; however, this is tempered by significant new TOPS mode data processing challenges which have the potential to significantly limit the usefulness of even coherent InSAR data. A TOPS mode Sentinel-1 frame is comprised of 3 ~80 km wide sub-swathes which are merged together in the range direction forming the final width of the swath, and 9 smaller ~80 km by 20 km bursts within each sub-swath which are acquired sequentially in the azimuth direction. The active microwave radar beam is steered in both the range and azimuth direction across a burst as it is acquired, which given that the satellite is constantly orbiting, results in adjacent geographical regions being viewed with a slightly different imaging geometry. The small difference in imaging geometry results in a phase discontinuity at the burst boundaries within each Sentinel-1 SAR frame. As there is a small region of overlap in the geographical area observed within each burst, on regions of stable, non-deforming terrain the phase discontinuity can be corrected by measuring the interferometric fringe rate in the burst-overlap region, and then subtracting this value from the adjoining burst. In regions of unstable, constantly deforming terrain, such as ice streams, the phase discontinuity represents a real difference in the phase signal measured on adjacent bursts. Although it is possible to try and correct the phase discontinuity using the method previously described, as the difference is ultimately a real difference rather than just a constant offset, the phase jump at the burst boundary is often not fully removed. It has been widely suggested that the problem of correcting the phase jump at the burst boundary will cause too large an error in the phase signal measured on ice thereby severely limiting the usefulness of coherent Sentinel-1 acquisitions for mapping ice sheet grounding lines. I have conducted an initial investigation into this problem, and here I present the first successful example of a Sentinel-1a QDInSAR measurement of the grounding line position. This demonstrates that Sentinel-1 already offers the potential for making widespread, present day grounding line measurements provided that sufficient SAR triplets are acquired over the ice sheet margin.

I used a time series of four Sentinel-1a TOPS mode SLC data acquired in interferometric wide swath mode, with a HH polarisation, over the Dotson Ice shelf in West Antarctica. The data was acquired every 12-days with a ~35° inclination angle between 23rd November 2014 and the 17th December 2014. The SAR data backscatter intensities were radiometrically calibrated and noise corrected using metadata files provided with the Sentinel-1 SAR data, specific to each individual acquisition. Each Sentinel-1a frame was de-bursted in the azimuth direction and then sub-swaths were merged in the range direction to remove the data gaps in the SLC frame. The SLC frame was multi-looked by 5 and 1 pixels in the range and azimuth direction respectively to form square, 20 m by 20 m pixels. Two temporally sequential SLC master and slave image pairs were formed and both image pairs were co-registered using common intensity features retrieved across the image frame after making an initial estimate of the co-registration offsets using the orbital state vectors provided in the Sentinel-1 metadata. We produced an interferogram from each co-registered image pair and then removed the simulated Earth curvature and topographic phase signal from each interferogram. At this stage it should be possible to estimate and correct the phase discontinuity at the burst boundaries; however, although tested, this step was not successfully completed and remains as work to be completed in the future. The two interferograms of the Dotson ice shelf now contain phase signal from surface displacement caused by ice flow which we assume is constant over the short 24 day total study period, and vertical displacement of the ice shelf by ocean tides which is not constant in both interferograms. We differenced the two interferograms to remove the constant phase signal caused by ice flow which revealed a dense band of InSAR fringes, which produced a QDInSAR image that shows the ice sheet grounding line, and small residual phase discontinuities at the burst boundaries that it was not possible to correct for during the InSAR processing (Figure 6-4).

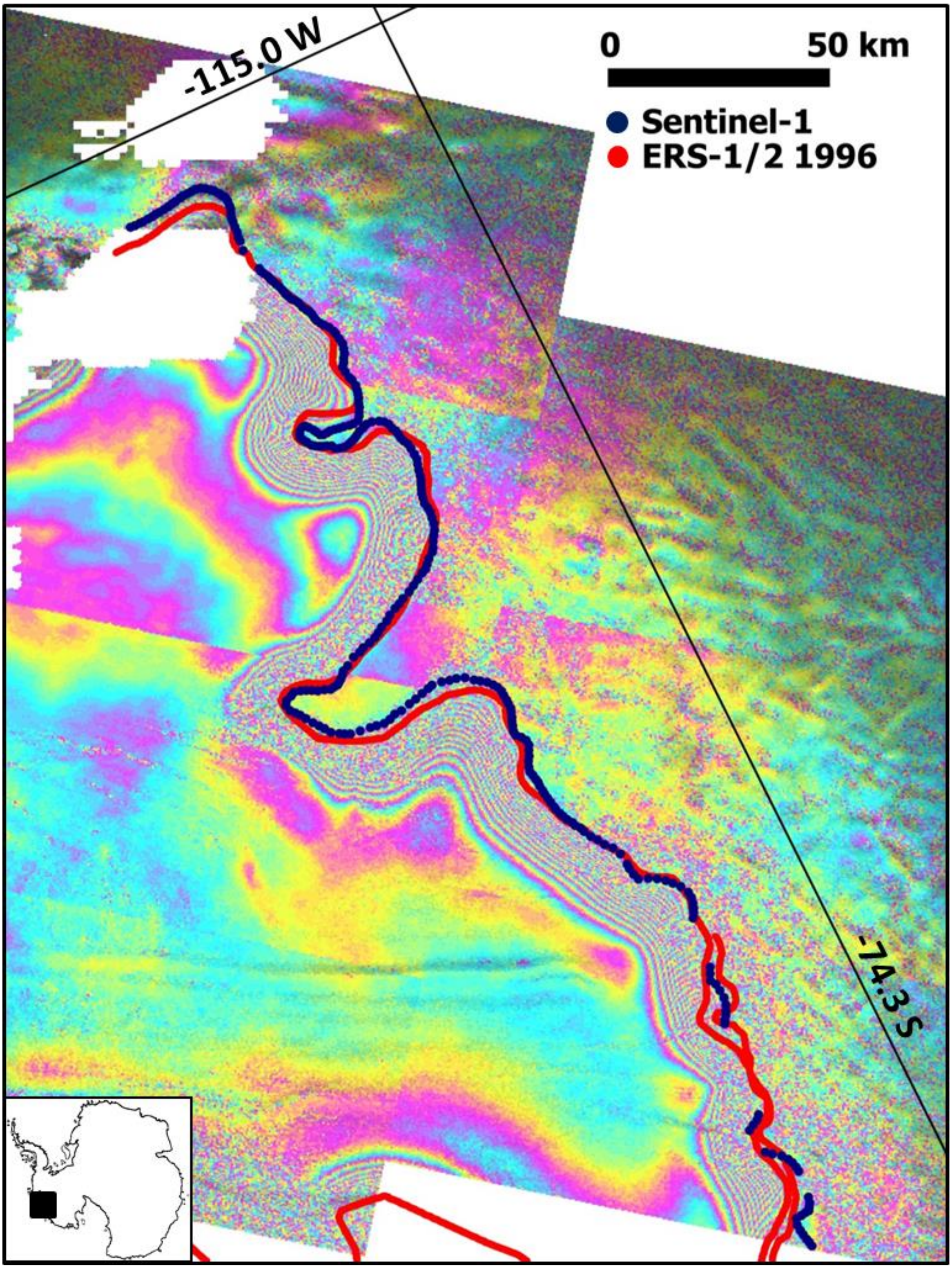

Figure 6-4. *Sentinel-1a 12-day repeat TOPS mode quadruple difference interferogram of the Dotson Ice Shelf, West Antarctica. Shown with the grounding line picked from the Sentinel-1a QDInSAR (blue dots), and 1996 ERS-1/2 QDInSAR (red dots).*

The grounding zone measured here on the Dotson ice shelf (Figure 6-4) is the first demonstration that it is possible to measure ice sheet grounding lines using Sentinel-1. We show that when the grounding line is picked as the inland limit of tidal flexure from the Sentinel-1a QDInSAR image, it closely matches the QDInSAR measurement of the grounding line position measured 20 years earlier by ERS-1/2 (Rignot et al., 2011). This shows that in the last 20-years on the Dotson ice shelf, there has been no significant grounding line retreat which is consistent with observations of surface elevation change over the last 20 years, which have also not shown any large rates of surface lowering on the grounded ice flowing into this ice shelf (McMillan et al., 2014). This first result also demonstrates that a residual phase discontinuity at the burst boundary does not significantly affect the location of the inland limit of tidal flexure, and therefore the measured grounding line position; however, the magnitude of the unwrapped surface displacement will be affected by this processing artefact. It is essential that this new satellite mission is fully utilised and that SAR data is acquired over the most rapidly changing regions of the ice sheet with sufficient repeats (3 minimum) to allow QDInSAR measurements to be made. This will enable us to better constrain the rate, magnitude and spatial variability of present day grounding line migration on both the Antarctic and Greenland ice sheets.

6.5 Concluding Remarks

Over the last 25 years satellite Earth observation has transformed our view of the Antarctic and Greenland ice sheets. Complex patterns of surface elevation change have shown that ice loss is now occurring at rates greater than 9 m per year in regions of dynamic instability (McMillan et al., 2014), and ice speed up of more than 40 % can occur both seasonally (Joughin et al., 2014) and over longer inter-annual periods (Mouginot et al., 2014). Grounding line retreat has been observed in the ice sheet regions which have exhibited the most rapid dynamic change showing that it is a sensitive indicator of instability. In conclusion, the research described in this thesis and the work by others (Thomas 1979, Rignot 1998a, Shepherd et al 2001, Fricker and Padman 2006, Joughin et al 2010, Park et al 2013, Dutrieux et al 2014, Rignot et al 2014, Favier et al 2014) has demonstrated the importance of ice sheet grounding line locations as a sensitive indicator of dynamic imbalance. However, the challenges associated with measuring this glacial parameter means that today we are only just starting to understand and the variability and size of short and long term migration (Park et al., 2013; Rignot et al., 2014, Chapter 3). As demonstrated in this thesis, by developing new techniques to fully exploit the Earth observation data archives, we can increase the number of grounding line measurements, which enables us to better understand the processes controlling short and long term migration. I have shown that when the magnitude of short term grounding line variability is quantified, it is much larger than previously thought and represents a significant proportion of even the fastest recorded rates of grounding line migration. In the future it is essential that we systematically acquire and assess long term continuous SAR datasets over all major marine based ice sheet grounding zones in order to measure grounding line retreat rates, and to disentangle natural variability from permanent change which directly contributes to present day rates of sea level rise.

References

Allen, C. (2013) IceBridge MCoRDS L3 Gridded Ice Thickness, Surface, and Bottom*,* Version 2, Petermann_2010_2012_Composite. Boulder, Colorado USA: NASA DAAC at the National Snow and Ice Data Center.

ASTER GDEM Validation Team: METI/ERSDAC, NASA/LPDAAC, USGS/EROS, in cooperation with NGA and other collaborators, ASTER GDEM Validation Summary Report, available at: http://www.jspacesystems.or.jp/ersdac/GDEM/E/ image/ASTERGDEM ValidationSummaryReport Ver1.pdf, 2009.

Aulard-Macler, M., R. Barstow, D. Ramsbottom, P. Lim (2011) Sentinel-1 Product Definition, *MacDonald Dettwiler and Associates Ltd*, **2.3**, SEN-RS-52-7440.

Bindschadler, R., H. Choi, A. Wichlacz, R. Bingham, J. Bohlander, K. Brunt, H. Corr, R. Drews, H. Fricker, M. Hall, R. Hindmarsh, J. Kohler, L. Padman, W. Rack, G. Rotschky, S. Urbini, P. Vornberger, N. Young (2011) Getting around Antarctica: new high-resolution mappings of the grounded and freely-floating boundaries of the Antarctic ice sheet created for the International Polar Year, *The Cryosphere*, **5**, 569 – 588.

Brunt, K. M., H. A. Fricker, L. Padman, T. A. Scambos, S. O'Neel, (2010) Mapping the grounding zone of the Ross Ice Shelf, Antarctica using ICESat laser altimetry, *Annals of Glaciology*, **51**, (55), 71 – 79.

Brunt, K., M., H. A. Fricker, L. Padman (2011) Analysis of ice plains of the Filchner-Ronne Ice Shelf, Antarctica, using ICESat laser altimetry, *Journal of Glaciology*, **57**, 205, 965 – 975.

Church, J. A., P.U. Clark, A. Cazenave, J.M. Gregory, S. Jevrejeva, A. Levermann, M.A. Merrifield, G.A. Milne, R.S. Nerem, P.D. Nunn, A.J. Payne, W.T. Pfeffer, D. Stammer and A.S. Unnikrishnan (2013) Sea Level Change, In: Climate Change 2013: The Physical Science Basis. Contribution of Working Group I to the Fifth Assessment Report of the Intergovernmental Panel on Climate Change [Stocker, T.F., D. Qin, G.-K. Plattner, M. Tignor, S.K. Allen, J. Boschung, A. Nauels, Y. Xia, V. Bex and P.M. Midgley (eds.)]. Cambridge University Press, Cambridge, United Kingdom and New York, NY, USA.

Clark, C. D., A. L. C. Hughes, S. L. Greenwood, C. Jordan, H. P. Sejrup (2012) Pattern and timing of retreat of the last British-Irish ice sheet, *Quaternary Science Reviews*, **44**, 112 – 146, DOI: 10.1016/j.quascirev.2010.07.019.

Conwey, H., B. L. Hall, G. H. Denton, A. M. Gades, E. D. Waddington (1999) Past and future grounding line retreat of the West Antarctic Ice Sheet, *Science*, **286**, 280 - 283, DOI: 10.1126/science.286.5438.280.

CryoSat-2 Product Handbook (2012) ESRIN-ESA and Mullard Space Science Laboratory – University College London, http://emits.sso.esa.int/emits-doc/ESRIN/7158/CryoSat-PHB-17apr2012.pdf

Cuffey, K. M. and W. S. B. Patterson, (2010) Reaction of glaciers to environmental changes, In: The Physics of Glaciers, 4th edition, Elsevier, China.

Dutrieux, P., J. De Rydt, A. Jenkins, P. R. Holland, H. K. Ha, S. H. Lee, E. J. Steig, Q. Ding, E. P. Abrahamsen, M. Shröder (2014) Strong sensitivity of Pine Island Ice-Shelf melting to climatic variability, *Science*, **343**, 174-178, doi:10.1126/science.1244341.

Eineder., T. F., J. Mittermayer, B. Schättler, W. Balzer, S. Buckreuβ, R. Werninghaus (2008) TerraSAR-X Ground Segment Product Specification Document, *DLR*, **1.5**, TX-GS-DD-3302.

Falkner, K. K., H. Melling, A. M. Münchow, J. E. Box, T. Wohlleben, H. L. Johnson, P. Gudmandsen, R. Samelson, L. Copland, K. Steffen, E. Rignot, A. K. Higgins (2011) Context for the recent massive Petermann Glacier calving event, *EOS Transactions American Geophysical Union*, **92**, 14, 117 – 118.

Favier, L., G. Durand, S. L. Cornford, G. H. Gudmundsson, O. Gagliardini, F. Gillet-Chaulet, T. Zwinger, A. J. Payne, A. M. Le Brocq (2014) Retreat of Pine Island Glacier controlled by marine ice-sheet instability, *Nature Climate Change*, **4**, 117-121, doi:10.1038/NCLIMATE2094.

Fricker, H. A. and L. Padman (2002) Tides on Filchner-Ronne Ice Shelf from ERS radar altimetry, *Geophysical Research letters*, **29**, 12, doi: 10.10292001GL014175.

Fricker, H. A. and L. Padman (2006) Ice shelf grounding zone structure from ICESat laser altimetry, *Geophysical Research Letters*, **33**, L15502.

Fricker, H. A., R. Coleman, L. Padman, T. A. Scambos, J. Bohlander, K. M. Brunt (2009) Mapping the grounding zone of the Amery Ice Shelf, East Antarctica using InSAR, MODIS and ICESat, *Antarctic Science*, **21**, 5, 515-532.

Goldstein, R. M., H. A. Zebker, C. L. Werner (1988) Satellite radar interferometry: Two-dimensional phase unwrapping, *Radio Science*, **23**, 4, 713-720.

Goldstein, R. M., H. Engelhardt, B. Kamb, R. M. Frolich (1993) Satellite radar interferometry for monitoring ice sheet motion: Application to an Antarctic ice stream, *Science*, **262**, 1525 – 1530.

Hansen, R. F. (2001) Radar Interferometry: Data interpretation and error analysis, Kluwer Academic Publishers, Dordrecht.

Helm, V., A. Humbart, H. Miller (2014) Elevation and elevation change of Greenland and Antarctica derived from CryoSat-2, *The Cryosphere*, **8**, 1539 - 1559, doi:10.5194/tc-8-1539-2014.

Hogg, A. E. and A. Shepherd (2013) Mapping ice sheet grounding lines using differential range direction offset tracking of TerraSAR-X Data, *TerraSAR-X Science Team Meeting*, DLR, Oberpfaffenhofen, 10th -13th June 2013.

Hogg, A. E., A. Shepherd, N. Gourmelen, M. Engdahl (Chapter 3), Grounding line migration from 1992 to 2011 on Petermann Glacier, North West Greenland.

Holdsworth, G. (1969) Flexure of a floating ice tongue, *Journal of Glaciol*ogy, **8**, 385–397.

Holland, D. M., R. H. Thomas, B. D. Young, M. H. Ribergaard, B. Lyberth (2008) Acceleration of Jakobshavn Isbrae triggered by warm subsurface ocean waters, *Nature Geoscience*, **1**, 659 – 664, doi:10.1038/ngeo316.

Horgan, H. J., S. Anandakrishnan (2006) Static grounding lines and dynamic ice streams: Evidence from Siple Coast, West Antarctica, *Geophysical Research Letters*, **33**, L18502, doi: 10.1029/2006GL027091.

Howat, I. M., J. E. Box, Y. Ahn, A. Herrington, E. M. McFadden (2010) Seasonal variability in the dynamics of marine-terminating outlet glaciers in Greenland, *Journal of Glaciology*, **56**, 198, 601 – 613.

Huybrechts, P. (2002) Sea level changes at the LGM from ice-dynamic reconstructions of the Greenland and Antarctic ice sheets during the glacial cycles, *Quaternary Science Reviews*, **21**, 203 – 231.

Jackson, C. R., and J. R. Apel (2004) Synthetic Aperture Radar Marine User's Manual, *National Oceanic and Atmosphere Administration*, Washington DC.

Johnson, H. L., A. Münchow, K. K. Falkner, H. Melling (2011) Ocean circulation and properties in Petermann Fjord, Greenland, *Journal of Geophysical Research*, **116**, C01003, doi:10.1029/2010JC006519.

Joughin, I., M. Fahnestock, R. Kwock, P. Gogineni, C. Allen (1999) Ice flow of Humboldt, Petermann and Ryder Gletscher, northern Greenland, *Journal of Glaciology*, **45**, 150, 231 – 241.

Joughin, I. and L. Padman (2003) Melting and freezing beneath Filchner-Ronne ice shelf, Antarctica, *Geophysical Research Letters*, **30**, (9), 1477, doi:10.1029/2003GL016941.

Joughin, I., S. B. Das, M. A. King, B. E. Smith, I. M. Howat, T. Moon (2008) Seasonal speedup along the Western flank of the Greenland ice sheet, *Science*, **320**, 781 - 783, doi:10.1126/science.1153288.

Joughin, I., B. E. Smith, D. M. Holland (2010) Sensitivity of 21st century sea level to ocean-induced thinning of Pine Island Glacier, Antarctica, *Geophysical Research Letters*, **37**, L20502, doi:10.1029/2010GL044819.

Joughin, I., R. B. Alley, D. M. Holland (2012) Ice-Sheet Response to Oceanic Forcing, *Science*, **338**, 1172 – 1176, doi:10.1126/science.1226481.

Joughin, I., B. E. Smith, D. E. Shean, D. Floricioiu (2014a) Brief Communication: Further speedup of Jakobshavn Isbrae, *The Cryosphere*, **8,** 209-214, doi:10.5194/tc-8-209-2014.

Joughin, I., B. E. Smith, B. Medley (2014b) Marine ice sheet collapse potentially underway for the Thwaites Glacier basin, West Antarctica, *Science*, **344**, 735-738, doi:10.1126/science.1249055.

Kobarg, W. (1988) The tide-dependent dynamics of the Ekström Ice Shelf, Antarctica , Berichte zur Polarforschung (Reports on Polar Research), Bremerhaven, Alfred Wegener Institute for Polar and Marine Research, 50 ,1-164, doi: 10013/epic.10050.d001.

Marsh, O. J., W. Rack, D. Floricioiu, N. R. Golledge, W. Lawson (2013) Tidally induced velocity variations of the Beardmore Glacier, Antarctica, and their representation in satellite measurements of ice velocity, *The Cryosphere*, **7**, 1375 – 1384, doi:10.5194/tc-7-1375-2013.

McMillan, M., A. Shepherd, P. Nienow, A. Leeson (2011) Tide model accuracy in the Amundsen Sea, Antarctica, from radar interferometry observations of ice shelf motion, *Journal of Geophysical Research*, **116**, doi:10.1029/2011JC007294.

McMillan, M., A. Shepherd, A. Sundal, K. Briggs, A. Muir, A. Ridout, A. Hogg, D. Wingham (2014) Increased ice losses from Antarctica detected by CryoSat-2, *Geophysical Research Letters*, **41**, 3899-3905, 10.1002/2014GL060111.

Moon, T., I. Joughin, B. Smith, I. Howat (2012) 21st – Century Evolution of Greenland Outlet Glacier velocities, *Science*, **336**, 576, doi:10.1126/science.1219985.

Moon, T., I. Joughin, B. Smith, M. R. van den Broeke, W. J. van de Berg, B. Nöel, M. Usher (2014) Distinct patterns of seasonal Greenland velocity, *Geophysical Research Letters*, **41**, 7209 – 7216, doi:10.002/2014GL061836.

Mouginot, J., E. Rignot, B. Scheuchl (2014) sustained increase in ice discharge from the Amundsen Sea Embayment, West Antarctica, from 1973 to 2013, *Geophysical Research Letters*, **41**, doi: 10.1002/2013GL059069.

Muchow, A., L. Padman, H. A. Fricker (2014) Interannual changes of the floating ice shelf of Petermann Gletscher, North Greenland, from 2000 to 2012, *Journal of Glaciology*, **60**, 221, doi:10.3189/2014JoG13J135.

Nick, F. M., A. Luckman, A. Vieli, C. J. Van Der Veen, D. Van As, R. S. W. Van De Wal, F. Pattyn, A. L. Hubbard, D. Floricioiu (2012) The response of Petermann Glacier, Greenland, to large calving events, and its future stability in the context of atmospheric and oceanic warming, *Journal of Glaciology*, **58**, 208, doi:10.3189/2012JoG11J242.

Nick, F. M., A. Vielli, M. L. Andersen, I. Joughin, A. Payne, T. L. Edwards, R. S. W. van de Wal (2013) Future sea-level rise from Greenland's main outlet glaciers in a warming climate, *Nature*, **497**, 235 – 238, doi:10.1038/nature12068.

Padman, L., H. A. Fricker, R. Coleman, S. Howard, S. Erofeeva (2002) A new tidal model for the Antarctic ice shelves and seas, *Annals of Glaciology*, **34**, 247-254.

Padman, L. and S. Erofeeva (2004) A barotropic inverse tidal model for the Arctic Ocean, *Geophysical Research Letters*, **31**, L02303, doi:10.1029/2003GL019003.

Padman, L., H. A. Fricker, R. Coleman, S. Howard, L. Erofeeva (2002) A new tide model for the Antarctic ice shelves and seas, *Annals of Glaciology*, **34**, 247 – 254.

Park, J. W., N. Gourmelen, A. Shepherd, S. W. Kim, D. G. Vaughan, and D. J. Wingham (2013) Sustained retreat of the Pine Island Glacier, *Geophysical Research Lett*ers, **40**, 2137-2142.

Payne, A. J., Vieli, A. A. P. Shepherd, D. J. Wingham, E. Rignot (2004) Recent dramatic thinning of largest West Antarctic ice stream triggered by oceans, *Geophysical Research Letters*, **31**, L23401, doi:10.1029/2004GL021284.

Paolo, F., H. A. Fricker, L. Padman (2015) Volume loss from Antarctic ice shelves is increasing, *Science*, **348**, 6232, 327 – 331, doi: 10.1126/science.aaa0940.

Pollard, D. and R. M. DeConto (2009) Modelling West Antarctic ice sheet growth and collapse through the past five million years, *Nature*, **458**, 329 – 322, doi: 10.1038/nature07809.

Pritchard, H. D., R. J. Arthern, D. G. Vaughan, L. A. Edwards (2009) Extensive dynamic thinning on the margins of the Greenland and Antarctic Ice sheets, *Nature*, **461**, 971 – 975, doi:10.1038/nature08471.

Rabus, B. T., and O. Lang (2002) On the representation of ice-shelf grounding zones in SAR interferograms, *Journal of Glaciology*, **48**, 162, 345 – 356.

Rack, W. and H. Rott (2004) Pattern of retreat and disintegration of the Larsen B ice shelf, Antarctic Peninsula, *Annals of Glaciology*, **39**, 505 - 510.

Rebesco, M., E. Domack, F. Zgur, C. Lavoie, A. Leventer, S. Brachfeld, V. Willmott, G. Halverson, M. Truffer, T. Scambos, J. Smith, E. Pettit (2014) Boundary condition of grounding lines prior to collapse, Larsen-B Ice Shelf, Antarctica, *Science,* **345**, 1354 - 1358, doi: 10.1126/science.1256697.

Rignot, E. (1996) Tidal motion, ice velocity and melt rate of Petermann Gletscher, Greenland, measured from radar interferometry, *Journal of Glaciology*, **42** (142), 476 – 485.

Rignot, E. (1998a) Hinge-line migration of Petermann Gletscher, North Greenland, detected using satellite-radar interferometry*, Journal of Glaciology*, **44** (148), 469 – 476.

Rignot, E. (1998b) Fast Recession of a West Antarctic Glacier, *Science*, **281**, 549-551.

Rignot, E., R. H. Thomas (2002) Mass Balance of Polar Ice Sheets, *Science*, **297**, 1502 – 1506.

Rignot, E., G. Casassa, P. Gogineni, W. Krabill, A. Rivera, R. Thomas (2004) Accelerated ice discharge from the Antarctic Peninsula following the collapse of Larsen B ice shelf, *Geophysical Research Letters*, **31**, L18401, doi:10.1029/2004GL020697.

Rignot, E., J. L. Bamber, M. R. Van den Broeke, C. Davis, Y. Li, W. Jan Van de Berg, E. Van Meijgaard (2008) Recent Antarctic mass loss from radar interferometry and regional climate modelling, *Nature Geoscience*, **1**,106 – 110, doi:10.1038/ngeo102.

Rignot, E. and K. Steffen (2008) Channelized bottom melting and stability of floating ice shelves, *Geophysical Research Letters*, **35**, L02503, doi:10.1029/2077GL031765.

Rignot, E., J. Mouginot, B. Scheuchl (2011) Antarctic grounding line mapping from differential satellite radar interferometry, *Geophysical Research Letters*, **38**, L10504.

Rignot, E., J. Mouginot, M. Morlighem, H. Seroussl, B. Scheuchl (2014) Widespread, rapid grounding line retereat of Pine Island, Thwaites, Smith and Kohler glaciers, West Antarctica, *Geophysical Research Letters,* **41**, 3502 – 3509, doi:10.1002/2014GL060140.

Rosich, B., P. J. Meadows, B. Schättler, M. Grion, and G. Emiliani (2001) The ERS-2 mono-gyro and extra backup piloting modes: Impact on SAR performance, presented at the CEOS Workshop, Tokyo, Japan, Apr. 2–5, 2001.

Rott, H., P. Skvarca, T. Nagler (1996) Rapid collapse of Northern Larsen Ice Shelf, Antarctica, *Science*, **271**, 5250, 788 – 792.

Rott, H. and Siegel, A. (1996) Glaciological Studies in the Alps and in Antarctica using ERS Interferometric SAR, FRINGE, Zurich, Switzerland, 30th September-2nd October 1996.

Scambos, T. A., C. Hulbe, M. Fahenstock, J. Bohlander (2000) The link between climate warming and break-up of ice shelves in the Antarctic Peninsula, *Journal of Glaciology*, **46**, 154, 516 – 530.

Scharroo, R. and P. Visser (1998) Precise orbit determination and gravity field improvement for the ERS satellites, *Journal of Geophysical Research*, **103**, C4, 8113-8127.

Schmeltz, M., Rignot, E., and MacAyeal, D. (2002) Tidal flexure along ice-sheet margins: comparison of InSAR with an elastic-plate model, *Annals of Glaciology*, **34**, 202–208.

Schoof, C. (2007) Ice sheet grounding line dynamics: steady states, stability and hysteresis, *Journal of Geophysical Research*, **112**, F03S28.

Shepherd, A. , D. J. Wingham, J. A. D. Mansley, H. F. J. Corr (2001) Inland Thinning of Pine Island Glacier, West Antarctica, *Science*, **291**, 5505, 862 – 864.

Shepherd, A., D. Wingham T. Payne, P. Skvarca (2003) Larsen ice shelf has progressively thinned, *Science*, **302**, 5646, 856 – 859.

Shepherd, A., D. Wingham (2007) Recent sea-level contributions of the Antarctic and Greenland Ice Sheets, *Science*, **315**, 1529 – 1532.

Shepherd, A., D. Wingham, D. Wallis, K. Giles, S. Laxon, A. V. Sundal (2010) Recent loss of floating ice and the consequent sea level contribution, *Geophysical Research Letters*, **37**, L13503, doi: 10.1029/2010GL042496.

Shepherd, A., E. R. Ivins, G. A, V. R. Barletta,4 M. J. Bentley, S. Bettadpur, K. H. Briggs, D. H. Bromwich, R. Forsberg, N. Galin, M. Horwath, S. Jacobs, I. Joughin, M. A. King, J. T. M. Lenaerts, J. Li, S. R. M. Ligtenberg, A. Luckman, S. B. Luthcke, M. McMillan, R. Meister, G. Milne, J. Mouginot, A. Muir, J. P. Nicolas, J. Paden, A. J. Payne, H. Pritchard, E. Rignot, H. Rott, L. S. Sørensen, T. A. Scambos, B. Scheuchl, E. J. O. Schrama, B. Smith, A. V. Sundal, J. H. van Angelen, W. J. van de Berg, M. R. van den Broeke, D. G. Vaughan, I. Velicogna, J. Wahr, P. L. Whitehouse, D. J. Wingham, D. Yi, D. Young, H. J. Zwally (2012) A reconciled estimate of ice-sheet mass balance, *Science*, **338**, 1183-1189,doi:10.1126/science.1228102.

Smith, A. M. (1991) The use of tilt meters to study the dynamics of Antarctic ice-shelf grounding lines, *Journal of Glaciology*, **37** (125), 51-58.

Strozzi, T., A. Luckman, T. Murray, U. Wegmuller, C. L. Werner (2002) Glacier motion estimation using SAR offset-tracking procedures, *IEEE Transactions on Geoscience and Remote Sensing*, **40**, 2384–2391.

Sundal, A. V., A. Shepherd, P. Nienow, E. Hanna, S. Palmer, P. Huybrechts (2011) Melt-induced speed-up of Greenland ice sheet offset by efficient subglacial drainage, *Nature*, **469**, 521 - 524, doi:10.038/nature09740.

Sundal, A. V., A. Shepherd, M. van den Broeke, J. van Angelen, N. Gourmelen, J. Park (2013) Controls on short-term variations in Greenland glacier dynamics, *Journal of Glaciology*, **59**, 217, 883 - 892, doi: 10.3189/2013JoG13J019.

Tachikawa, T., M. Hato, M. Kaku, A. Iwasaki (2011) Characteristics of ASTER GDEM Version 2, *IEEE*, IGARSS 2011 Proceedings, 3657 – 3660.

Thomas, R. H., T. J. O. Sanderson, K. E. Rose (1979) Effect of climatic warming on the West Antarctic ice sheet, *Nature*, **277**, 355 – 358.

Thomas, R. H. (1984) Ices margins and ice shelves, *AGU Geophysical Monograph Series: Climate Processes and Climate Sensitivity*, **29**, 265 - 274.

Tsai, V. C., and G. H. Gudmundsson (2015) An improved model for tidally modulated grounding-line migration, *Journal of Glaciology*, **61**, 226, 216 - 222, DOI: 10.3189/2015JoG14J152.

Vaughan, D. G. (1995) Tidal flexure at ice shelf margins, *Journal of Geophysical Research,* **100,** (B4), 6213 – 6224.

Velicogna, I. and J. Wahr (2013) Time-variable gravity observations of ice sheet mass balance: Precision and limitations of the GRACE satellite data, *Geophysical Research letters*, **40**, 3055 – 3063, doi:10.1002/grl.50527.

Werner, C., U. Wegmüller, T. Strozzi, A. Weismann (2000) GAMMA SAR and Interferometric Processing Software, ERS – ENVISAT Symposium, Gothenburg, Sweden, 16-20 Oct 2000.

Willis, J. K., J. A. Church (2012) Regional sea-level projection, *Science*, **336**, 550 – 551.

Wingham, D. J., C. R. Francis, S. Baker, C. Bouzinac, D. Brockley, R. Cullen, P. de Chataeu-Thierry, S. W. Laxon, U. Mallow, C. Mavrocordatos, L. Phalippou, G. Ratier, L. Rey, F. Rostan, P. Viau, D. W. Wallis (2006) CryoSat: A mission to determine the fluctuations in Earth's land and marine ice fields, *Advances in Space Research*, **37**, 841 - 871.

Wouters, B., A. Martin-Español, V. Helm, T. Flament, J. M. van Wessem, S. R. M. Ligtenberg, M. R. van den Broeke, J. L. Bamber (2015) Dynamic thinning of glaciers on the Southern Antarctic Peninsula, *Science*, **348**, 6237, 899-903.

Van Wessem, J. M., C. H. Reijmer, M. Morlegheim, J. Mouginot, E. Rignot, B. Medley, I. Joughin, B. wouters, M. A. Depoorter, J. L. Bamber, J. T. M. Lenearts, W. J. Vende Berg, M. R. Van den Broeke, E. Van Meijgaard (2014) Improved representation of East Antarctic surface mass balance in a regional atmospheric climate model, *Journal of Glaciology*, **60**, 222, 761 - 770, doi: 10.3189/2014JoG14J051.

Vaughan, D. G. (1995) Tidal flexure at ice shelf margins, *Journal of Geophysical Research,* **100,** (B4), 6213 – 6224.

Zwally, H. J., B. Schutz, W. Abdalati, J. Abshire, C. Bentley, A. Brenner, J. Bufton, J. Dezio, D. Hancock, D. Harding, T. Herring, B. Minster, K. Quinn, S. Palm, J. Spinhirne, R. Thomas, (2002) ACESat's laser measurements of polar ice, atmosphere, ocean and land, *Journal of Geodynamics*, **34**, 405 – 445.

Zwally, H. J., M. B. Giovinetto, M. A. Beckley, J. L. Saba (2012) Antarctic and Greenland Drainage Systems, GSFC Cryospheric Sciences Laboratory, http://icesat4.gsfc.nasa.gov/cryo_data/ant_grn_drainage_systems.php